THE UNIVERSITY OF QUEENSLAND

AUSTRALIA

Optimised Multifunctionality of Mesoporous Carbon Hollow Spheres (MCHS) Nanocarriers Using Carbonisation Temperature

Trisha Ghosh

B.Pharm, MEng

A thesis submitted for the degree of Doctor of Philosophy at

The University of Queensland in 2019

Australian Institute for Bioengineering and Nanotechnology

Abstract

Currently, chemotherapeutic research is using smart and specially engineered multifunctional nanocarriers for targeted nanomedicine for improved and promising cancer treatment. Mesoporous carbon nanomaterials (MCNs) have been widely regarded for this purpose owing to its multifunctional nature. MCNs possess unique combinations of chemical and physical properties along with high surface area, high porosity, biocompatibility and high cellular uptake making them up-and-coming candidates in many areas of biomedical research such as drug delivery, tissue scaffolding, cellular sensors, etc. With a steady increment in the biomedical research centred on MCN as potential nanocarrier systems for chemotherapeutics, the need to determine the optimised conditions to synthesise MCN with the most desirable traits are that much more necessary. One of the critical factors that control the physical, chemical, electrical and mechanical behaviour of MCN is the carbonisation temperature. Carbonisation temperature determines the carbon content, carbon bonding, crystallinity, hydrophobicity, solubility, porosity which in turn influences their effectiveness. Although there have been studies on the characteristic differences in MCNs influenced by carbonisation temperature, however, the impact the carbonisation temperature makes in bio-application of MCN has not been reported so far. So, this PhD aims to study the influence of carbonisation temperature in MCNs and to investigate its behaviour in the biological environment for varied biological applications.

In the first part, we prepared mesoporous carbon hollow spheres (MCHS) using resorcinol-formaldehyde polymer and silica hard-template in the one-pot synthesis process. We carbonised the polymer-silica matrix at different carbonisation temperatures (MCHS-T) and studied its changes in physical and chemical properties such as morphology, aqueous distribution, crystallinity, hydrophobicity, carbon content, surface area and porosity. We further investigated the loading capacity and release pattern of the various carbonised samples and their intracellular behaviour. We observed that the delivery of therapeutic biomolecule in cancer cells varied depending on which temperature the nanocarriers were carbonised which led to different cytotoxicity. With this study, we were able to find out the optimised temperature at which mesoporous carbon hollow spheres should be carbonised to achieve the best nanocarrier performance for the delivery of therapeutic protein in cancer therapy.

In the second part, we investigated the antioxidant property (free radical scavenging) mediated by the temperature of carbonisation of MCHS-T. We found that MCHS-T is a great antioxidant agent which lowers the ROS levels in cells that are suffering from oxidative stress. We carbonised MCHS-T from temperatures 700-1300° C to find the optimised

temperature that elicits the maximum antioxidant property. We also demonstrated MCHS's antioxidant property compared with other popular carbon nanoparticles in their pristine form. The extracellular ROS scavenging activity was analysed via (Electron paramagnetic resonance) EPR, and the intracellular antioxidant property was evaluated using flow cytometry (FACS), microplate reading and confocal imaging techniques.

In the third part, we tested the photothermal property (conversion of light into heat) and photothermal ablation capacity of MCHS-T when carbonised at various temperatures for a promising combination (chemotherapy and photothermal) treatment. First, we tested the loading and delivery of 17AAG (a heat shock protein inhibitor) whose purpose is to make the cancer cells more susceptible to thermal damage. Then the cancer cells that internalised MCHS-T carrying 17AAG were irradiated with UV-light for a 3 min period, and the number of viable cells was checked to determine the effect of the combination therapy.

Declaration by author

This thesis is composed of my original work, and contains no material previously published or written by another person except where due reference has been made in the text. I have clearly stated the contribution by others to jointly-authored works that I have included in my thesis.

I have clearly stated the contribution of others to my thesis as a whole, including statistical assistance, survey design, data analysis, significant technical procedures, professional editorial advice, financial support and any other original research work used or reported in my thesis. The content of my thesis is the result of work I have carried out since the commencement of my higher degree by research candidature and does not include a substantial part of work that has been submitted to qualify for the award of any other degree or diploma in any university or other tertiary institution. I have clearly stated which parts of my thesis, if any, have been submitted to qualify for another award.

I acknowledge that an electronic copy of my thesis must be lodged with the University Library and, subject to the policy and procedures of The University of Queensland, the thesis be made available for research and study in accordance with the Copyright Act 1968 unless a period of embargo has been approved by the Dean of the Graduate School.

I acknowledge that copyright of all material contained in my thesis resides with the copyright holder(s) of that material. Where appropriate I have obtained copyright permission from the copyright holder to reproduce material in this thesis and have sought permission from co-authors for any jointly authored works included in the thesis.

Publications included in this thesis

Peer-reviewed paper

Trisha Ghosh, Manasi Mantri, Zhengying Gu, Mohammad Kalantari, Meihua Yu and Chengzhong Yu, Mesoporous carbon hollow spheres: carbonisation-temperature-dependent delivery of therapeutic proteins, Journal of Material Chemistry B, 2018, 6, 763-768.

Conference proceedings

Oral Presentations:

Trisha Ghosh, Carbonization temperature influence of mesoporous carbon hollow nanoparticles on therapeutic protein delivery, The 8th International Symposium on Nano & Supramolecular Chemistry, 13-16 July 2016, Brisbane, Australia.

Submitted manuscripts included in this thesis

Trisha Ghosh, Manasi Mantri, Zhengying Gu, Mohammad Kalantari, Meihua Yu and Chengzhong Yu, Mesoporous carbon hollow spheres: carbonisation-temperature-dependent delivery of therapeutic proteins, Journal of Material Chemistry B, 2018, 6, 763-768- included in Chapter 4.

Other Publications during Candidature

No other publications

Contributions by others to the thesis

Contributors	Statement of contribution
Author Trisha Ghosh (Candidate)	Experimental design and performance (85%) Analysis and interpretation of data (85%) Drafting and writing (80%)
Author Meihua Yu	Experimental design and performance (5%) Analysis and interpretation of data (10%) Drafting and writing (10%)
Author Manasi Mantri	Experimental design and performance (5%)
Author Zhengying Gu	Experimental design and performance (3%) Analysis and interpretation of data (1%)

Author Hao Song	Experimental design and performance (3%)
Author Chengzhong Yu	Experimental design and performance (5%)
	Analysis and interpretation of data (10%)
	Drafting and writing (10%)

All the confocal images were taken in Australian National Fabrication Facility (ANFF-Q) (Chapter 4 and 5), and the SEM and TEM images were taken in Australian Microscopy and Microanalysis Research Facility at the Centre for Microscopy and Microanalysis, The University of Queensland (Chapter 4). The Electron paramagnetic resonance (EPR) analysis was conducted in the Centre for Advanced Imaging (Chapter 5), The University of Queensland.

Statement of parts of the thesis submitted to qualify for the award of another degree
None
Research Involving Human or Animal Subjects
No animal or human subjects were involved in this research

Acknowledgements

At first, I would like to express my sincere gratitude to my supervisor Prof. Chengzhong (Michael) Yu for allowing me to pursue my PhD in his research group. I always counted on his wisdom, support, patience, valuable insight and motivation. His infectious passion for research has always directed me to the right path. My PhD projects were hugely polished and improved, thanks to his useful suggestions. I also would like to appreciate my co-supervisor Dr Meihua Yu for her active support, suggestions and guidance. Her guidance has helped me with my project designs and experiments. Both of them has helped me to grow my research, knowledge, skills and techniques that I will carry with me in my future. I would also like to thank my assessors, Dr Barbara Rolfe and Dr Bin Luo, for reviewing my work and helping me improve my research over time.

   I am grateful to all the members of the Yu research group for making this journey fulfilling and for making our research lab a pleasant place to work. I would like to thank my colleagues especially Manasi Mantri, Mohammad Kalantari, Prasanna Lakshmi, Anand Kumar Meka, Manasi Mantri, Owen Noonan, Jun Zhang, Chang Lei, Chun Xu, Yang Liu, Yanan Yang, Min Zhang, Yue Wang, Xiaoran Sun, Hao Song, Jianye Fu, Zhengying Gu,Hongwei Zhang, Swasmi Purwajanti and Yusilawati Ahmad Nor, for either their cooperation in the office, during experiments and lab work as well as for their beautiful friendship. Additionally, I would like to thank Cheryl Berquist (lab manager), Colette Godfrey (floor manager) of Centre for Personalised nanomedicine for their aid for making sure that the laboratory work went as smooth as possible.

 I would like to thank Dr Jane Kenna, Facility manager at Australian Institute for Bioengineering and Nanotechnology (ANFF-Q) on her belief in me and all ANFF-Q professional officers, Center for Microscopy and Microanalysis (CMM), and Centre for Advanced Imaging (CAI) for providing training and technical assistance.

    Last but not the least, I want to express my most profound gratitude to my best friend Mr Bivas Kanti Saha for his unconditional support and love that helped me build the courage to face and conquer all the challenges I faced. Words are not enough to describe my tremendous love and respect for my parents, Mr Bhaskar Kumar Ghosh and Mrs Mukta Ghosh for their genuine care and love and for supporting me throughout my life. Many thanks to my brother Arnab Ghosh for taking care of my parents while I was away from home and his belief in me. I am blessed to have them in my life, and without them supporting me, this dissertation would not have come to a completion.

Keywords

Mesoporous carbon hollow spheres, carbon nanocarriers, carbonisation temperature, protein delivery, cancer therapeutics, free radical scavenging, oxidative stress, photothermal agent, combination therapy

Australian and New Zealand Standard Research Classifications (ANZSRC)

ANZSRC code: 090302, Biomedical Engineering, 40%

ANZSRC code: 100708, Nanomaterials, 40%

ANZSRC code: 091205, Nanomaterial Characterisation, 20%

Fields of Research (FoR) Classification

FoR code: 0903, Biomedical Engineering, 40%

FoR code: 1007, Nanotechnology, 40%

FoR code: 1115, Pharmaceutical Sciences, 20%

Table of Contents

List of Figures and Tables

Fig 2.8. Schematic representation of PTT therapy using carbon nanomaterials as photothermal agents

Fig 2.9. Schematic diagram representation of carbon nanotubes used in cancer cell ablation in PTT.

Scheme 3.1. A schematic representation of the one-pot synthesis of MCHS-*T*.

Scheme 4.1. Schematic representation of mesoporous carbon hollow spheres optimised by carbonization temperature for intracellular therapeutic protein delivery and the cancer cell cytotoxicity.

Fig 4.1 SEM (A, B, C) and TEM (D, E, F) images of MCHS-500, MCHS-700 and MCHS-900, respectively.

Fig 4.2. Raman spectra (A) and DLS profiles of MCHS-T (B) in PBS and (C) in DMEM culture media.

Fig. 4.3. (A) N_2 adsorption-desorption isotherms, (B) pore size distribution curves, (C) loading capacity of RNase A and (D) RNase A release profiles of MCHS-*T*.

Fig. 4.4 Dosage-dependent cell viability of SCC25 cells treated with bare and RNase A after (A) 24 and (B) 48 h incubation. ns p> 0.05, *p<0.05, **p<0.01, ***p<0.001.

Fig. 4.5 Confocal microscopy images of SCC25 treated with RNase A delivered with MCHS-700 and MCHS-900. Blue fluorescent signal indicates the nuclei stained with DAPI; green represents FITC tagged with RNase A and red represents the endo/lysosome stained by lysotracker. Scale bar is 10 μm.

Fig 4.S1. FTIR spectral analysis of MCHS-T carbonised at different temperatures indicated as MCHS-500, MCHS-700, and MCHS-900.

Fig 4.S2. Relative hydrophobicity as measured by adsorption of Rose Bengal on MCHS-*T*. (A) PQ and (B) LE values as a function of the weight of MCHS-*T* and (C) LC of 10 µg of MCHS-*T* towards RB.

Fig 4.S3. (A) TEM image and (B) nitrogen absorption-desorption isotherm and pore size distribution curve (inset) of MCHS-1100.

Fig 4.S4. Images are showing the dispersion of MCHS-900 and MCHS-1100 after ultra-sonication. We observed that MCHS-900 had excellent dispersity in PBS buffer solution whereas MCHS-1100 started to separate from the buffer solution and settle as aggregates in PBS after 5 minutes of ultra-sonication.

Fig 4.S5. (a) Loading capacity of RNase A, (b) RNase A release profile of MCHS-900 and MCHS-1100, (c) RBITC positive cell percentages and (d) mean fluorescence intensity of SCC25 cells treated with RBITC labelled MCHS-900 and MCHS-1100.

Fig 4.S6. Cell viability of SCC25 cells treated with bare MCHS-*T* at a high concentration of 200μg/mL to investigate the biocompatibility of the nanocarriers.

Fig 4.S7. Confocal Microscopic images of SCC25 showing the fluorescent signals of blue representing DAPI and green representing RNase A tagged with FITC carried inside the cells by MCHS-500, the scale bar is 10μm.

Fig 5.1 Schematic representation of antioxidant MCHS-900 having ROS scavenging property.

Fig 5.2 (A) Effect of MCHS carbonised at different temperatures on hydroxyl radicals generated by Fenton reaction. The number of radicals produced is proportional to the intensity of EPR signals(B) Intracellular ROS scavenged by MCHS carbonised at different temperatures in HCT-116 cells, ns, *$p<0.05$, **$p<0.01$, ***$p<0.001$.

Fig 5.3 (A) Effect of different carbon nanoparticles on hydroxyl radicals generated by Fenton reaction measured by intensity of EPR signal (B) Intracellular ROS scavenged by different carbon nanoparticles in HCT-116 cells, ns, *$p<0.05$, **$p<0.01$, ***$p<0.001$.

Fig.5.4 Bright field images of HCT-116 cells stained with DCFH2-DA (green fluorescence) after being incubated with tert-Butyl hydro peroxide and then treated with 25μg of carbon nanoparticles to detect their scavenging property (A) Positive control (B) CNT (C) RGO (D) MCHS-900

Fig 5.5 Confocal images of HCT-116 cells showing cellular uptake of carbon samples loaded with RhB with the same feeding amount of RhB determined from the loading capacity of the sampeles where (A)DAPI@Control PBS (B) PBS (C) DAPI combined with CNT@RhB (D)CNT@RhB (E)DAPI combined with MCHS-900@RhB (F)MCHS-900@rhB (G)DAPI combined with RGO@RhB (H) RGO@RhB. The scale bar is 2μm.

Fig 5.6 Flow cytometry analysis of cellular uptake of different carbon uptake of different carbon samples loaded with RhB in HCT-116 after 4 hours of incubation, inset cellular uptake histogram; where, ns, *$p<0.05$, **$p<0.01$, ***$p<0.001$.

Fig 6.1 Schematic representation of the multi-hit modality of photothermal therapy and chemotherapy for a tumour and cancer cell ablation.

Fig 6.2 Photothermal heating graph of MCHS-T at different concentrations of 75 µg/ml and 200 µg/mL after UV-A irradiation for 3 min.

Fig 6.3 UV-Vis spectral analysis of MCHS-*T* in PBS buffer solution at pH 7.4.

Fig 6.4. (A) The loading efficiency of 17 AAG in MCHS-*T* (B) the release profile of MCHS-*T*, ns p> 0.05, *p<0.05, **p<0.01, ***p<0.001.

Fig 6.5 (A) Dosage-dependent cell viability of MCF 7 cells treated with bare testing the biocompatibility of MCHS-*T* aftder 24 hours incubation (B) Cell viability of MCF 7 after combination therapy by exposing them to pure 17 AAG, only MCHS-*T* and 17 AAG loaded in MCHS-*T* and after irradiation with UV light irradiation for 3 minutes; ns p> 0.05, *p<0.05, **p<0.01, ***p<0.001.

Table 1.1 Rational design of nanocarriers for cancer therapy

Table 2.2. Various antioxidants with their mechanism of action

Table 4.1. Summary of the physicochemical properties of MCHS-T

Table 4.S1. Calculated RNase A adsorption capacity of MCHS samples.

List of Abbreviations used in the thesis

MCN - Mesoporous Carbon Nanoparticles/ Nanocarriers

MCHS - Mesoporous Carbon Hollow Spheres

TPOS - Tetrapropyl orthosilicate

RF- Resorcinol Formaldehyde

TEM - Transmission Electron Microscopy

XPS - X- ray Photon Spectroscopy

SEM - Scanning Electron Microscopy

BJH - Barrett–Joyner–Halanda

EPR - Electron Paramagnetic Resonance

CNT - Carbon Nanotubes

MWCNT - Multiwall Carbon Nanotubes

SWCNT- Single Carbon Nanotubes

RGO - Reduced Graphene oxide

BET - Brunauer–Emmett–Teller

UV - Ultraviolet

EA - Elemental Analysis

ATR-FTIR - Attenuated Total Reflectance -Fourier Transform Infrared Spectroscopy

DLS - Dynamic Light Scattering

MTT - 3-[4,5-dimethylthiazol-2-yl]-2,5-diphenyl tetrazolium bromide

ROS - Reactive Oxygen Species

FACS - Flow Cytometry Analysis

PTT - Photothermal Therapy

HSP 90 - Heat Shock Protein 90

17 AAG - 17-*N*-allylamino-17-demethoxygeldanamycin

SCC 25 - Squamous Cell Carcinoma

MCF 7- Michigan Cancer Foundation 7 (breat cancer cells)

HCT-116 - Homo sapiens Colon Colorectal Cancer

RNase A - Ribonuclease A

Chapter 1

Introduction

1.1. The significance of the work

The development of specially designed and engineered nanoparticles possessing unique structures and properties has witnessed a massive surge in nano-biomedical research in recent years.   In particular, cancer research has substantially benefited from this development as it has opened gates to a newer chemotherapeutic approach than conventional methods that are usually associated with high-risk factors and side effects. Various nanoparticles systems have been synthesised such as polymer-based nanoparticles, lipid-based nanoparticles, micelles, quantum dots, nanofibers, magnetic nanoparticles, carbon-based nanoparticles, etc., to enhance the performance of drug molecules while reducing the risk of toxicity. Among them, carbon-based nanocarrier such as fullerenes, carbon nanotubes, carbon nano-horns, nanodiamonds, porous carbon and graphene has shown to be extremely beneficial in bio-medical applications for nanomedicine, drug delivery and bio-labelling, due to their distinct structures made up of uniquely hybridised carbons [2]. Carbon nanoparticles at present are standing at crossroads between proof of principle concept and established clinical candidates for therapeutic applications[3]. Carbon nanoparticles have distinct optical, thermal, mechanical and electrical properties along with inherent hydrophobicity, biocompatibility and their capacity to penetrate the cells and tissues which makes them suitable for different biological applications[4, 5]. Owing to the numerous benefits of carbon nanoparticles, researchers utilize these multifunctional nanoparticles in three broad approaches for chemotherapeutic applications, [6, 7]:

1. **Nanocarrier systems:**   Carbon nanocarrier systems (such as CNTs, graphene, fullerene, C dots, mesoporous carbon nanoparticles) possess some distinctive physicochemical and biological characteristics that make them suitable for diagnosis

and chemotherapeutic practices as they help overcome cellular barriers and enhance the intracellular concentration of drug candidates. Therapeutic bio-macromolecules such as nucleic acids, proteins, DNA, genes, are mainly benefited as they increase their bioavailability using both active and passive targeting strategies [8-11].

2. ROS Scavenging Nanomedicines (Carbon-based antioxidants): Carbon nanoparticles have demonstrated excellent antioxidant prowess owing to their high interaction with reactive oxygen species (ROS), the prime reason for various grave illnesses such as myocardial infarction, kidney failure, Rheumatoid Arthritis, Parkinson's, etc. Carbon nanoparticles have drawn attention towards their superior free radical scavenging abilities when compared to other agents such as Vitamin C, Vitamin E, PEG-SOD in clinical research[12-14].
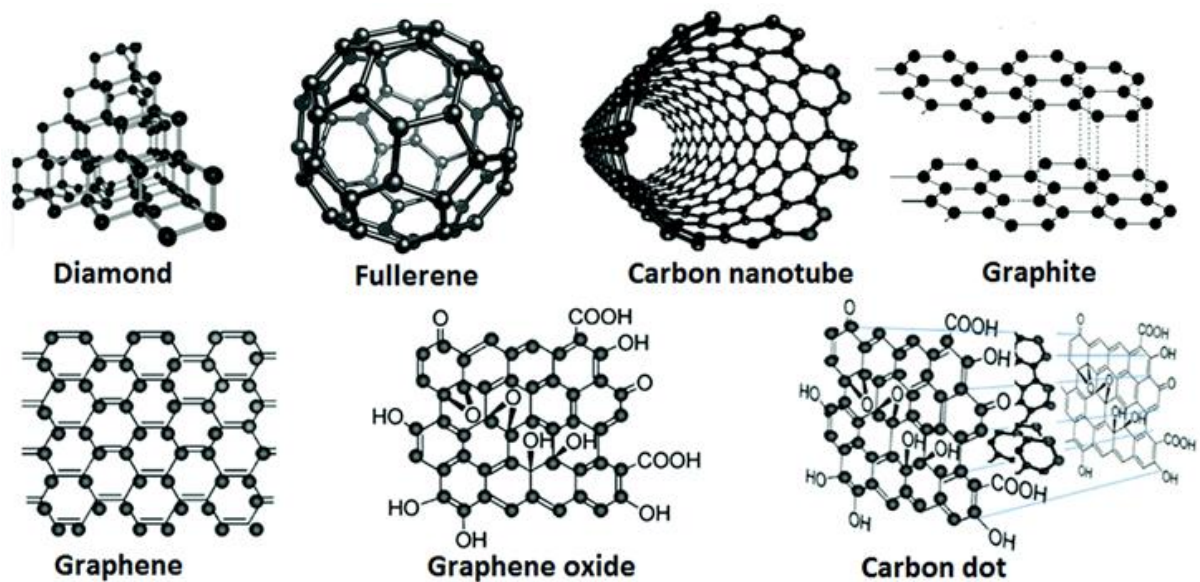
Fig 1.1. The schematics of the representative carbon-based nanomaterials (Pic courtesy Creative Diagnostics)

3. Photothermal agents: Currently, there is much interest in light absorbing materials such as metallic nanoparticles[15, 16], semiconductor polymer nanoparticles[17, 18] and carbon-based nanostructures[19, 20]. The unique structure carbon composition, electrical and thermal characteristics offer a promising approach to cancer therapy. The idea is to place the multifunctional carbon nanomaterials at tumour sites and heating that site to impart photothermal effect via local hyperthermia[21, 22].

1.1.1. Mesoporous carbon nanoparticles as delivery systems

Among the various carbon-based nanocarrier systems, mesoporous carbon nanospheres have carved its niche as novel owing to its large surface area, open frameworks, mesoporosity, large internal volumes, chemical inertness and hydrophobicity. These numerous properties make them more noticeable and beneficial for high adsorption of hydrophobic drugs with the controlled release pattern and efficient cellular delivery [23, 24]. They have been used for delivery of drugs, contrast agents and target molecules (genes, DNA, proteins) [25, 26]. Owing to its hydrophobic properties, it has shown a better affinity towards hydrophobic anticancer drug molecules (ex, doxorubicin, cisplatin, paclitaxel, etc.) and has demonstrated enhanced antitumour efficiency [26]. Thus, owing to the numerous advantages of mesoporous carbon-based nanocarrier systems, they have increasingly become desirable candidates for biomedical applications from the carbon family [23, 27-29]. Mesoporous carbon nanoparticles are especially beneficial for delivery of therapeutic proteins[9, 30]. In chemotherapeutics, protein-based drugs are gaining popularity mostly because of its adequate potency lacking the random/ genetic side effects. Harnessing them for therapeutics holds more considerable promise for cancer treatment than conventional chemotherapy [31, 32]. However, their fragile structures and extreme sensitivity to physicochemical changes in their immediate environment, such as hydrolysis, oxidation, proteolysis and denaturation necessitate having an escorting that can transport them successfully within the cytosol of the cell to elicit an effective response[32]. It is anticipated that mesoporous carbon nanoparticles are porous and multifunctional; they could serve as a platform for next-generation nanocarrier system for diagnosis and therapy simultaneously [26, 31]. Mesoporous carbon nanospheres are derived from the polymer sources under heating process in a nitrogen environment [28] in which the treated carbonisation temperature determines the physicochemical, electrical and mechanical properties of final products [33, 23, 34, 35].

1.1.2. Mesoporous Carbon nanoparticles as Antioxidant agents

Recent preclinical studies have demonstrated that carbon nanomaterials exhibited superior antioxidant properties than those of dietary antioxidants, and it is an affinity towards cellular uptake [14] [12]. Their antioxidant properties have shown impressive results in not only ROS generated diseases such as cancer etc.; but also showed promising performance in recovery and restoration in patients who suffered a traumatic brain injury. However, among the various carbon particles utilised for biomedical

applications, mesoporous carbon nanomaterials hold a more significant promise as it has a carbonaceous composition with high porosity, biocompatibility, chemical inertness, cellular affinity, which are highly desirable traits for therapeutics strategies[36-38]. Moreover, owing to its physicochemical properties, it readily interacts with ROS species (hydroxyl radicals) in its natural form optimised by carbonisation temperature and displays ROS scavenging activity, which has never been reported in any other carbon nanoparticles.

1.1.3. Mesoporous carbon nanoparticles as photothermal agents

Colloidal mesoporous carbon nanospheres form stable suspensions in aqueous solutions and have exhibited high light absorption capabilities in UV-Vis-NIR region[39, 40]. Comparative studies with other photothermal agents such as gold nanorods, SWCNTs, graphene have shown mesoporous carbon nanospheres have 1.5-2 times higher than those of CNTs and graphene and are comparable to those of gold nanoparticles[39]. Additionally, due to high drug loading capabilities, they are also ideal candidates for the combination of tumour-suppression effect by using low drug dosage and laser power density. Thus, the high drug loading capacity together with excellent photothermal effect makes them promising platforms for cancer theranostics.

Most of the carbon nanoparticles such as graphene, CNTs, carbon dots, nanohorns, etc., are functionalised to achieve colloidal stability, biocompatibility and enhance their biological performance. However, the performance of mesoporous carbon nanospheres can be optimized by optimising various aspects such as size, porosity, temperature[28, 41]. Although several studies show the impact of carbonisation temperature on the structural and morphological features[34, 35] of the nanoparticles yet its impact on the biological behaviour has not been reported until now. Through this PhD work, we have tried to address this exact query by studying the mesoporous carbon nanospheres and its behavioural and performance changes according to the change in the temperature of carbonisation.

In the first part of the thesis, mesoporous carbon hollow spheres (MCHS) was synthesised using silica template method, carbonised at different temperatures 500°C-1100°C, followed by removal of the template. The porous MCHS were characterised and found MCHS-900 had the highest hydrophobicity and biocompatible among all samples, exhibiting superior RNase A (a model of therapeutic proteins) adsorption and

sustained release, beneficial for therapeutic protein delivery. RNase A delivered by MCHS-900 demonstrated significantly improved anti-cancer efficacy than free RNase A or delivered by MHCS-500 and MHCS 700. Furthermore, MCHS-900 also enhanced the cellular uptake of RNase A and successful endosomal escape, critical steps for therapeutic protein delivery.

In the second part, we investigated the optimised MCHS for highest antioxidant properties in the pristine state. For this, MCHS was carbonised from 700 °C to 1300 °C, their ROS scavenging activity was tested, and the optimised MCHS was selected depending on the highest ROS scavenging activity. Furthermore, MCHS ROS scavenging activity was also compared to other carbon-based ROS scavenging agents in their pristine form. Extracellular ROS scavenging activity and intracellular ROS scavenging activity were analysed. EPR analysis of pristine MCHS carbonised at different temperatures revealed MCHS-900 carbonised at 900°C has remarkable ROS scavenging profile in the aqueous environment. Further comparative EPR analysis revealed that MCHS-900 is 3.2 times and 2.7 times more effective than CNT and RGO, respectively. Moreover, intracellularly, the same trend was observed where MCHS-900 emerged as the best antioxidant agent for ROS- mediated therapeutic approach.

Finally, we explored the theranostic capabilities of MCHS. In this part, we again used MCHS carbonised at different temperatures, and we tested the up-conversion capabilities (conversion of absorbed light into heat) of mesoporous carbon hollow spheres in aqueous solutions. We also utilised MCHS as a nanocarrier system to deliver HSP 90 inhibitor intracellularly which works by inhibiting the heat shock chaperone protein in cancer cells making them ultra sensitive to thermal damage. Simultaneously, MCHS was irradiated with UV incident light, where the nanospheres absorbed the light and converted them into heat creating an environment of intracellular hyperthermia, thus inhibiting cancer cell proliferation.

1.1. Research objective and scope

The general aim of this project is to systematically investigate the optimisation of Mesoporous Carbon Hollow Spheres with carbonisation temperature and tuning its properties that determine its therapeutic behaviour in the biological environment. The specific aims include:

1) To investigate the impact of carbonisation temperature on MCHS and their correlation with its intracellular protein delivery.

2) To investigate the optimised carbonisation temperature to elucidate the highest ROS scavenging activity to be utilised as a best antioxidant agent

3) To investigate the theranostic abilities of temperature optimised MCHS delivering HSP90 inhibitor intracellularly to inhibit cancer cell by applying combination therapy (chemotherapeutics and photothermal effect)

Our study will pave the way towards the development of next-generation, highly effective mesoporous carbon nanoparticles that can be applied as active biomaterial systems in cancer therapy via simple optimisation technique.

1.2. Thesis Outline

This thesis is written according to the guidelines of the University of Queensland. The chapters in this thesis are presented in the following sequence:

Chapter Introduction 1

This chapter includes a brief overview of the background of this research work including aims and significance of the work.

Chapter 2 Literature Review

This chapter presents a detailed review of the contributions made by mesoporous silica nanoparticles in drug delivery systems. Also, a detailed review of the contribution of particle shape and pore size of MSN in a biological application.

Chapter 3 Methodology

This chapter summarizes the strategies utilized in the whole PhD project, including synthesis strategy of mesoporous carbon hollow spheres and its carbonisation technique along with the techniques for material characterizations and biological evaluations.

Chapter 4 Mesoporous Carbon Hollow Spheres: Carbonisation-Temperature-Dependent Delivery of Therapeutic Proteins

This chapter reports the influence of carbonization temperature of mesoporous carbon hollow spheres (MCHS) on their delivery performance of therapeutic protein in cancer cells.

Chapter 5 Antioxidant property of pristine mesoporous carbon hollow spheres (MCHS) for ROS mediated cancer therapeutic strategy

This chapter reports the ability of MCHS to relieve intracellular oxidative stress, mainly prevalent in cancer cells, by its efficient free radical scavenging property. Here we measured the antioxidant property of MCHS carbonised at various temperatures to select the optimized MCHS for maximum scavenging activity. We also tested the free radical scavenging activity of MCHS compared to other famous carbon scavengers to compare its effectiveness.

Chapter 6 Photothermal ablation of cancer cells using temperature optimized mesoporous carbon hollow spheres

This chapter reports the theranostics capabilities of MCHS by applying a combined therapy of chemotherapeutics and photothermal effect to inhibit cancer cells. We also tested the capabilities of MCHS to convert absorbed light into heat according to its the temperature of carbonisation.

Chapter 7 Conclusion and Recommendations

Conclusion and significant contributions of this work are highlighted, and recommendations for future work are presented.

Chapter 2

Literature Review

The inception of the concept, "Nanotechnology", was proposed by Richard Feynman in 1959 and since then, it has led to numerous developments in scientific and engineering disciplines. It has blessed researchers with the ability to investigate substances at a molecular level. Nanotechnology has raised the intrigue in generating innovative materials with outstanding properties revolutionising the field of chemistry, biology, material science, physics, engineering and biomedical sciences.[42] Nanotechnology is defined as a realm of science that takes advantage of the transformation induced in materials at nanometers scale (nanomaterials) ranging from 10^{-7} to 10^{-9} m in size, which would otherwise be absent in bulk form. Nanomaterials at this small level start exhibiting novel physical, chemical and biological properties that can be utilised to create unique materials, devices and systems.[43] Although, nanotechnology is a considerably new scientific field of interest; however, its impact has been utilised since ancient times. The most famous case of the use of nanotechnology in primaeval times was the "Lycurgus cup", made by ancient Roman glassblowers using small gold colloidal particles. The influence of using those nanosized gold particles was observed when the cup changed colour from opaque green to translucent red after the light was shone through it[44]. The astounding change in the optical property of the gold nanoparticles in its bulk form was discovered, but it took the scientific community several years before they realised the real potential of nanotechnology. Nanotechnology has given rise to various ways of manipulation of matter at the nanometer scale that allows researchers to design and engineer novel and precise synthesis of nanomaterials for desired functions and applications. As a result, nanotechnology has become a hot commodity in today's scientific world, which has attracted interests from prominent industries, organisations and governments. "The Global Nanotechnology Market Analysis" conducted a compressive market assessment across the major geographies such as North America, Europe, Asia

Pacific Middle East, Latin America and Rest of the world and estimated that nanotechnology might reach a global revenue of USD 173.95 billion by 2025. This goes to show how much of substantial investments are being made to build and expand this technology so that the possibility for developing future nanomaterials that are better, more efficient and effective in its respective applications becomes a reality.

2.1. Nanocarrier technology in the biomedical application:

Nanotechnology has given rise to a new age of hybrid science that exploits nanomaterials integrated into biological systems engineered to exhibit specific chemical and physical properties. The field of biomedical sciences has embraced nanotechnology with open arms after extensive investigations were carried out to find the potential of nanomaterials in medicine and biomedical applications such as imaging[30], sensing and detection[45], targeted drug[46, 47] and gene delivery[48, 49], medical implants[50], nanodevices[51] and disinfection[52].

In recent years, plenty of development has been made in designing and engineering nanomaterials that are specially designed to possess unique structures and properties useful in escorting therapeutic biomolecules and drug molecules that are otherwise restricted by our bio-systems. Therapeutic bio-macromolecules such as nucleic acids, proteins, peptides, DNA analogues (e.g., hormones, monoclonal antibodies, vaccines), are mainly benefited as nanocarrier systems using both active and passive targeting strategies[8-11].

2.2. Protein therapeutics:

Protein therapeutics pose tremendous opportunity as new age therapeutic method to alleviate some of the gravest of illnesses. Proteins are the building blocks that perform most complex and diverse roles in the human body to support and maintain balanced functions such as cellular signalling and gene expression that is hard for synthetically modified chemical moieties to replicate. Most of the human diseases such as cancer, autoimmune diseases and infectious diseases are a result of mutations or abnormalities in the levels of essential proteins in our bodies [53]. This has given researchers tremendous opportunities to explore its potential in biotherapeutics[54], vaccines[55, 56], tissue culture engineering[57], embryonic stem cell regulation[46,58-61]. Moreover, proteins and peptides are being harnessed cell targeted oncotherapy and theragnosis as they are highly potent and precise therapeutic agents minus the random/ genetic side effects [31] and holds a greater promise alternative medicine for

cancer treatment than conventional chemotherapy[62]. Recently, FDA (Food and Drug Administration) approved the first protein therapy, manufactured by "Novartis", which will be marketed as "Kymriah" also known as "CAR-T therapy" has shown remarkable results in bone marrow cancer that affects children and young adults. CAR-T therapy showed incredible potential when it was subjected to clinical trial. The clinical trial involved 63 children and young adults with a type of acute lymphoblastic leukaemia, 83% of patients that received the CAR-T therapy had their cancers go into remission within 3 months. At 6 months, 89 % of patients who received the therapy were still living, and at 12 months, 79 % had survived.

Although the potential of protein therapeutics is high, the presence of certain limitations confines the use of protein for therapeutic potentials such as poor cellular uptake, limited transportation into tissues and the blood-brain barrier, enzymatic hydrolysis, fragile tertiary structures that are easy to get deactivated or degraded in native forms [32]. That is why, nanocarrier systems are needed in the diagnosis and therapeutic practices, especially in cancer therapeutics to assist the target protein/drug molecule in overcoming cellular barriers and improving their intracellular concentration. The factors required for effective nanocarriers are summarized in Table1.

Table 2.1 Rational design of nanocarriers for cancer therapy[8, 53]

Advantages of nanocarriers over free drugs/biomolecules	Requirements nanocarriers should meet
Offers protection to the drug/biomolecule from premature degradation/ denaturation.	Synthesized with a very biocompatible material, well characterized and easily optimized
Enhances tissue absorption (like solid tumours) and overcomes multiple drug resistance	Exhibit high cellular uptake efficiency in cancer cells

Improves intracellular penetration	Be either soluble or colloidal under aqueous conditions for increased effectiveness
Enhances bioavailability	Have high drug/biomolecule loading capacity with controlled release pattern
Controls the pharmacokinetic and pharmacodynamics interactions	Have an extended circulating half-life, a low aggregation and a long shelf life

Various nanocarrier systems have been synthesised such as polymer-based nanocarrier, lipid-based nanocarriers, micelles, quantum dots, nanofibers, magnetic nanoparticles, carbon-based nanoparticles, etc., to enhance the performance of therapeutic molecules while reducing the chances of potential side-effects. Among the various nanocarriers, carbon nanocarriers have grabbed significant attention for its potential therapeutic drug delivery applications, especially in cancer therapeutics.

2.3. Carbon nanoparticles as escorts for protein therapeutics:

Numerous studies have suggested carbon-based nanocarrier such as fullerenes, carbon nanotubes (SWCNTs, MWCNTs), carbon nano-horns, C-dots, nanodiamonds, porous carbon and graphene are incredibly beneficial in bio-medical applications for nanomedicine, drug delivery and bio-labelling, due to their distinct structures made up of uniquely hybridised carbons [1]. Moreover, carbon nanocarriers are innately hydrophobic in nature. This allows them to have a higher affinity towards highly hydrophobic anticancer drug molecules such as doxorubicin, cisplatin, paclitaxel, and in turn, enhancing their bioavailability and effectiveness, which leads to enhanced antitumour efficiency. Presently most of the carbon nanomaterial allotropes used in biomedical applications possess desirable properties such as high cellular internalisation via various endocytotic mechanisms and fast endosomal release of protein conjugated carbon scaffolds into the cytoplasm that are essential steps to elicit is a fast and efficient response[63]. Using carbon nanomaterials as scaffolds enhance the utilisation potential of protein/ drug molecules which may solve the challenges in healthcare systems.

Carbon nanoparticles such as C-dots have reportedly suppressed cancer cells in vitro and are capable of inhibiting Hep G2 growth in liver cancer. Similar inhibition was seen in MCF-7 and MDA-MB-231 breast cancer cells where the cause was suggested to be due to the generation of large amounts of reactive oxygen species (ROS)[64, 65].

CNTs is another popular choice for researchers as robust nanocarriers systems. A leading effort in this field has been made by Dai group, which demonstrated multiple CNT based protein delivery platform for delivery in human cancer cell lines such as CHO and 3T3[66].
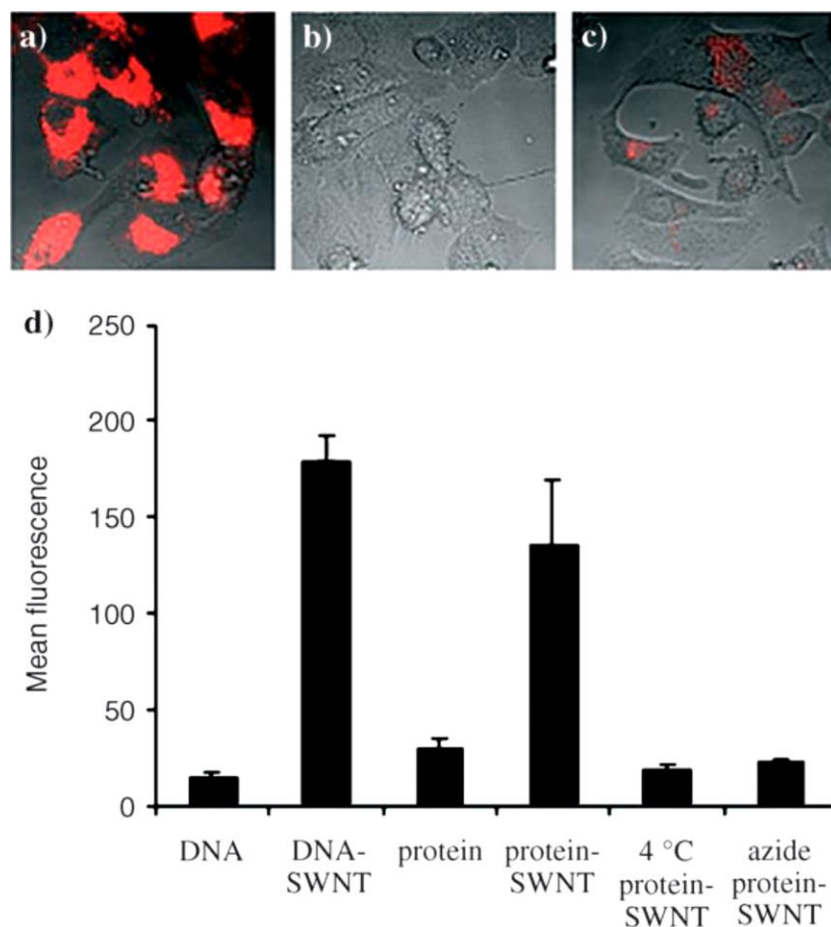
Fig 2.1. Confocal microscopy images of HeLa cells after incubation in fluorescently labelled DNA-SWNT at (a) 37°C (b) 4°C, and (c) after pretreatment with NaN_2. (d) flow cell cytometry data for HL60 cells that were incubated in fluorescently labelled pure DNA or protein solutions without nanotubes (labeled "DNA" and "protein", respectively), DNA_SWNT and SA-SWNT at 37°C, and protein-SWNT at 37°C in cells incubated at 4°C or presented with sodium azide[(image courtesy ref67)].

Nadine Wong Shi Kam et at. in 2006 investigated the delivery potential of proteins and DNA inside two different mammalian cells lines, adherent HeLa cells and non-adherent HL60 cells.
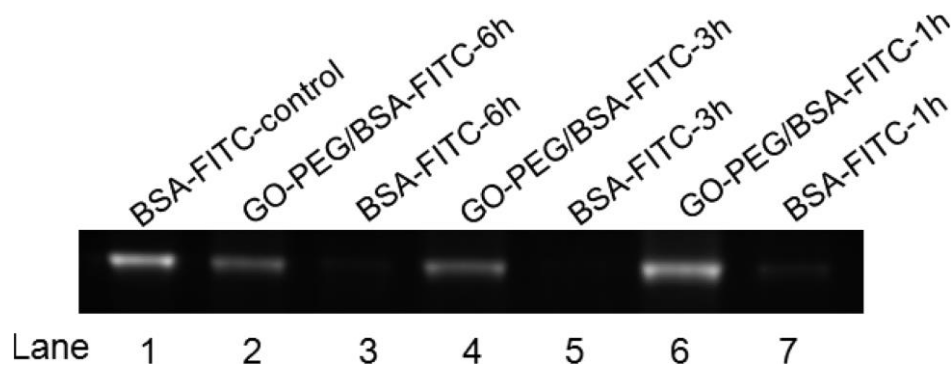
Fig 2.2. The SDS-PAGE analysis of BSA-FITC without trypsin digestion (lane 1) and GO-PEG/BSA-FITC and free BSA-FITC with trypsin cleavage for 1 h (lane 6 and 7), 3 h (lane 4 and 5), and 6 h (lane 2 and 3), respectively (image courtesy ref61).

In their study, they have shown that short SWNTs with right functionalization are capable of transportation of proteins and oligonucleotides into living cells via energy-dependent endocytosis mechanism of cellular uptake. Their cellular uptake and FACS data (Fig 1) showcased significantly elevated levels of fluorescing coming from cells introduced to carbon nanocarrier systems (SWNT) loaded with fluorescence-tagged proteins and oligoDNA proving the delivery efficiency of carbon nanocarrier systems.

Another carbon allotrope, graphene oxide (GO), has also shown promising results in intracellular trafficking of the therapeutic protein. In 2012, He Shen and co-workers reported PEG functionalized graphene oxide (GO-PEG) mediated protein delivery into cells. In their work, they delivered ribonuclease A (RNase A) which led to cell death and also transported protein kinase A (PKA) inducing cell growth and retaining their biological functions. Firstly, using SDS-PAGE analysis of protein-FITC, they observed the changes in the protein before and after trypsin digestion at various time points and found that GO-PEG/protein showed no discernable differences even after an hour of exposure where bare protein dissolved completely. The results (Fig 2); therefore, suggested protein loaded in GO were reasonably protected from enzymatic degradation than naked protein.

Furthermore, cellular uptake studies done on HeLa cells treated with GO-PEG/protein showed 42 % of cellular viability indicating high cytotoxicity caused by the intracellular delivery of therapeutic protein RNase A. They also delivered functional protein PKA (Protein Kinase A) to elucidate the influence of functional proteins delivered by GO-PEG. They saw PKA-regulated pathways in MCF7 cells were retained causing enhanced cell growth in contrast to free PKA.

15

Carbon nanocarriers such as graphene oxide, CNTs, nanohorns, carbon dots, fullerenes relies heavily on surface modifications and functionalisation to achieve higher biocompatibility, loading capacity, cellular interactions and sustained release[68, 69]. However, mesoporous carbon nanocarriers are unique carbon nanocarriers that don't rely on a surface modification to achieve those benefits.

2.3.1. Mesoporous carbon nanospheres as nanocarrier systems:

Among all the carbon family nanomaterials, mesoporous carbon nanospheres (MCNs) have drawn particular attention as the next generation of platforms for drug delivery and biomedical applications. When it comes to mesoporous nanomaterials, mesoporous silica nanomaterials (MSN) have gained the most attention owing to its large surface area, tunable pore size, high pore volume, large drug loading and storage capacity, biocompatibility, etc.   However, MCNs embody the benefits of both sp2 carbon-based materials as well as MSN's. They integrate a list of various features such as:

(i)   large surface area and pore volume for favourable for high drug loading capacity

(ii)   adjustable pore structure enabling controlled the supramolecular release

(iii)   excellent biocompatibility and physicochemical stability

(iv)   easy surface modification and optimisation that enhances the therapeutic drug efficiency

(v)   supramolecular π-π stacking allowing the high drug loading and sustained release of aromatic and hydrophobic drugs

(vi)   excellent heat conversion capacity   that provides possibilities of photothermal therapy (PTT)

(vii)   unique optical properties and natural combination with photoluminescent giving us options of exploring theranostic diagnosis functions.

Hence, it is anticipated that porous, multifunctional, multicomponent carbon nanoparticles could serve as a platform for next-generation nanocarrier system for diagnosis and therapy simultaneously[26, 31]. Thus, all of the benefits mentioned above

are making mesoporous carbon-based nanocarrier systems highly attractive candidates for biomedical applications[23, 27-29]. They have been used for delivery of drugs, contrast agents and target molecules (genes, DNA, proteins)[25, 26]. Owing to its hydrophobic properties, it has shown a better affinity towards hydrophobic anticancer drug molecules and has demonstrated enhanced antitumour efficiency [26]. However, mesoporous carbon nanocarriers are especially beneficial for active biomolecules like peptides, proteins, nucleic acids and therapeutic agents[9, 30].
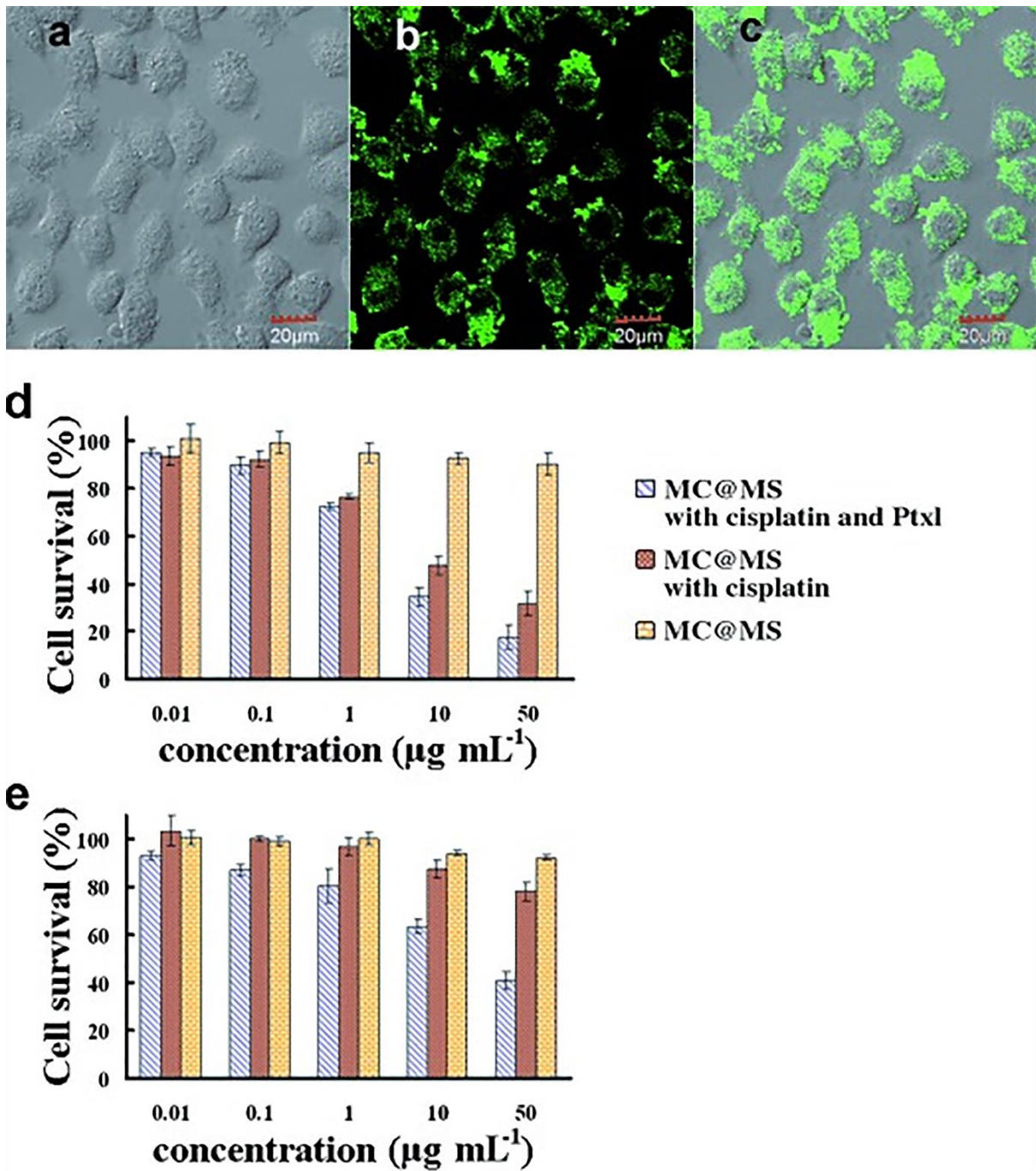
Fig 2.3. Bright (a), fluorescence (b), and overlay CLSM images (c) of SKOV3 after incubation for 3 h with the rattle like dual-pore mesoporous carbon/silica nanospheres MC@MS grafted with FITC group. d, e) Cytotoxicity of cisplatin and Ptxl drugs loaded into the MC@MS nanospheres, cisplatin

alone loaded into MC@MS nanospheres, and dual-pore mesoporous MC@MS nanospheres at the same dose in different human ovarian cancer cells (d) normal ovarian cancer cells SKOV3, and (e) drug-resistant A2780 (CP70) cells^(image courtesy ref70).

In recent years, Yin Fang and their co-workers synthesized dual–pore mesoporous carbon@silica composite nanospheres (MC@MS) for multidrug delivery, Fig 3. The hierarchical mesostructure and amphiphilicity of the hydrophobic carbon cores and hydrophilic silica shells led to distinct benefits in multi-drug combination therapy with anticancer drugs (Cisplatin and Paclitaxel) for the treatment of ovarian cancer including drug-resistant strains.

When they conducted a visual test using the confocal microscope of the cellular uptake of MC@MS in SKOV3 cells, they observed remarkable intracellular luminescence coming from the cytoplasm of the cells indicative of high cellular trafficking capability. Moreover, the cytotoxicity tests indicated MC@MS loaded with both cisplatin and paclitaxel (denoted as MC@MS-Pt-Ptxl), killed more than 50% of the cancer cells, indicating efficient therapeutic effect of the nanocarrier loading with chemical drugs for the normal human ovarian cancer cells when compared to MC@MS loaded with only cisplatin (denoted as MC@MS-Pt). In cisplatin-resistant A2780 (CP70) cells were cultured with a specific amount of MC@MS-Pt for 24 h, over 80 % of the cells were found to be alive. However, when the same cells were cultured with the same amount of MC@MS-Pt-Ptxl for 24 h, over 50 % of cisplatin-resistant cells are killed by the multidrug system. Their work showcased the performance of anticancer drug were enhanced significantly by the use of mesoporous carbon nanocarrier system and its tremendous potential for therapeutic cancer utilisation.
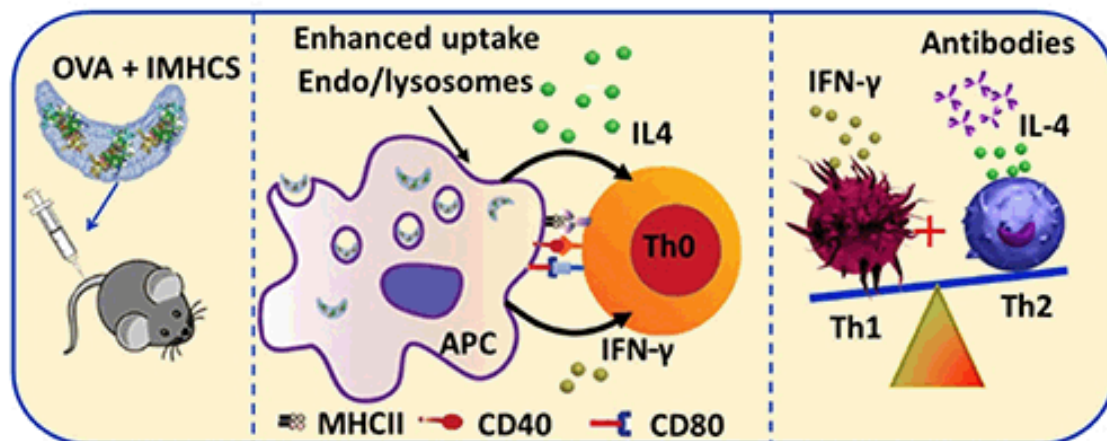
Fig 2.4 Schematic representation of protein loaded mesoporous carbon nanospheres for an enhanced immune response for vaccine delivery ^(image courtesy ref71).

Not only mesoporous carbon enhance anticancer drug activity, but they are also excellent carrier systems for biomolecules for medical application. Recently, Hongwei Zhang and co-workers from our research group demonstrated the high loading capacity of biomolecules such as "lysozymes" and "oligoDNA" mesoporous hollow carbon spheres (MHCS) for biomedical applications. Through his work, he demonstrated high loading of the biomolecules with rapid adsorption kinetics. The oligoDNA were tagged with cyanine dye (Cy3), were loaded in MHCS and human colon cancer cells (HCT-116) were treated with them. Confocal images of the cells showed strong signals from cells indicating high delivery of cargo biomolecule indicating the efficiency of mesoporous carbon nanospheres. Similarly, when Manasi Jambhrunkar, also from our research group tested the efficacy of mesoporous carbon nanospheres as an adjuvant system, she observed promising biological effects, Fig 4.

In her work, she highlighted the high loading capacity off vaccine proteins in the nanostructures, and when it was delivered as a vaccine on naïve 8-week-old C57BL/6J female mice, it showed amplified immune response to the delivered antigen. Although pristine mesoporous carbon nanospheres were highly biocompatible, exhibited little to no immunological response on its own, however, when antigen protein (OVA) were loaded in the nanoparticles. Moreover, *in-vivo* immunisation studies in mice demonstrated that OVA-loaded mesoporous carbon nanospheres induced a 3-fold higher IgG response compared to a traditional adjuvant QuilA used in veterinary vaccine research.

Thus, mesoporous carbon nanospheres not only showcased their potential as efficient intracellular nanocarrier systems but also has the potential to be utilized in cancer therapeutics for efficient and effective anti-cancer effects than conventional chemotherapy.

The primary reason mesoporous carbon nanocarrier's effectiveness lies in their fabrication process. Unlike other nanocarriers, mesoporous carbon nanocarriers are very easy to synthesize using templating methods and are engineered to possess desirable qualities and morphologies suited for their desirable role.

2.3.2. Synthesis of mesoporous carbon nanospheres

Nanostructured porous carbon nanomaterials have been applied to various applications such as gas storage, capacitors, adsorbents, electrode materials, gas storage and catalytic supports owing to its porous structures, high surface area and high adsorption capacity. With the increasing amount of investigation being carried

out in mesoporous carbon structures, scientists have discovered their incredible potential to be excellent nanocarrier systems with high cellular internalization capacity.

Porous carbon materials can be classified into three different categories namely, microporous (pore size<2 nm), mesoporous (2 nm<pore size<50 nm) and macroporous (pore size>50 nm)[72]. The primary way ordered mesoporous carbon materials are synthesized by carbonizing carbon precursors such as polymers, resins, etc. fused with a sacrificial template that makes the well-controlled porous frames. Current syntheses strategies can be categorized as either hard-template or soft template methods. The hard templating method involves the use of organic and inorganic templates that mainly serve as moulds for the replication of mesoporous carbon materials, and no significant interaction happens between the template and the precursors. On the other hand, the soft templating method involves the self-assembly of organic molecules. The corresponding pore structures are determined by the mixing, synthetic conditions, solvent and temperatures. Unlike hard template synthesis soft template involves the chemical interactions of the templates and carbon precursors.

The first reported synthesis of carbon nanomaterials was by Knox and co-workers who fabricated nanomaterials using a spherical sol-gel as a template[73]. Their approach included the following steps (a) preparation of silica template with controlled pore structure (b) impregnation or infiltration of the template with monomer or polymer precursors (c) crosslinking of the organic precursors followed by carbonization and finally (d) removal of the silica template. Knox et al. used the phenol-hexamine mixture as the carbon precursor. After the polymerization, the phenolic resin was carbonized inside the pores of the spherical silica gel to transform into carbon structures. The dissolution of silica template resulted in rigid, spherical mesoporous carbon. They even commercialized the carbon material as "Hypercarb" that were used in making unique retention characteristics in liquid chromatography. The synthesis approach established by the Knox group is being followed to this day as the most reliable and standard way of synthesizing mesoporous carbon nanostructures using the hard templating method.

Recently, Hongwei Zhang and co-workers from our research group successfully synthesized mesoporous carbon nanospheres using a hard silica templating method. His work demonstrated a simple one-pot synthesis process based on an *in situ* generated primary silica particles as templates, Fig 5. The highlight of the work was the ability to control the pore size which was adjustable from micropores to 13.9 nm.

Tetrapropyl orthosilicate (TPOS) and tetraethyl orthosilicate (TEOS) was used as a silica source, and resorcinol-formaldehyde (RF) was used as a carbon precursor source. First, they let the silica source to hydrolyse in order to form primary silica particles, after which RF oligomers polymerized and co-condensed onto the SiO_2 core particles forming a $SiO_2@SiO_2$/RF core-shell structure. Then the polymer-silica matrix was carbonized followed by the removal of SiO_2. The ratio of TPOS and TEOS were adjusted and depended on the ratios the pore sized were determined. He also reported using the hard templating method multilayered structures (bi- and triple-layered), and controllable morphologies (invaginated, endo-invaginated, and intact spheres) could also be synthesized with high mesoporous volume[28, 74, 75].
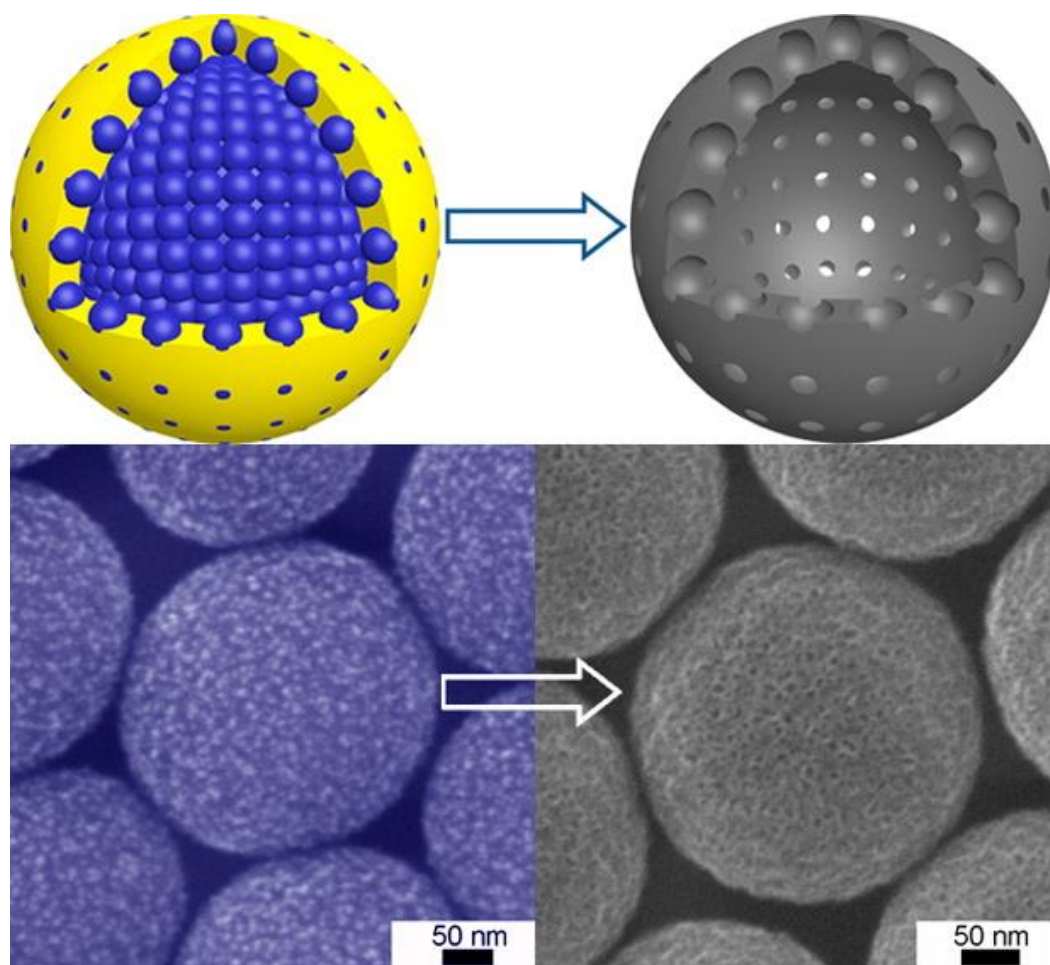
Fig 2.5. Graphical representation of mesoporous carbon hollow spheres with polymer carbon precursors embedded into silica template on the left while the right shows the finished mesoporous carbon hollow spheres after carbonization and removal of silica template.

Taking into account the ease of synthesis and the control over nanofabrication of the nanomaterials we prepared our carbon nanocarrier systems using the hard silica templating, one-pot synthesis method. As mentioned earlier mesoporous carbon nanocarriers give the engineering freedom to manipulate its features in order to

accommodate its role. Features such as porosity[36, 39], shape[36] and size[76] have been altered by controlling the synthesis process to acquire desired benefits. However, no reports have been published so far (to best of our knowledge) regarding the influence of carbonisation temperature on mesoporous carbon nanocarriers in biomedical application.

2.4. Parameters for optimisation of the physicochemical properties of carbon particles

As the use of nanocarrier systems increased in the biomedical applications, so did the assessments regarding the factors that influence their interactions with the biological environment. Research intended to associate the properties of nanomaterials such as size, shape, chemical functionality, surface charge, and composition with bio-molecular signalling, biological kinetics, transportation, and toxicity in both cell culture and animal experiments is vital [77]. These studies help set the foundations for engineering the next generation of nanoscale vectors and devices[77-80]. As the synthesis process of nanomaterials is essential to discover new therapeutic escorts, the tuning of the properties of the nanocarrier is just as vital. Continuous efforts are being made to improve the therapeutic delivery systems to maximise the therapeutic effect of the drug while diminishing its undesirable side effects. As far as carbon-based nanocarrier systems are concerned, they are no exception to the factors mentioned above and they do influence them to a certain extent. The application performance of mesoporous carbon nanospheres is strongly influenced by numerous factors such as surface modification, particle, pore size, reaction time and reaction temperature[36, 75, 81, 82]. Optimization of such factors helps it to attain desirable properties such as higher stability, loading capacity, better bioavailability, better encapsulation, controlled drug release, the possibility of incorporation of both hydrophilic and hydrophobic substances, the feasibility of variable routes of administration, which are vital features for carbon nanocarrier systems to consider as efficient drug delivery systems.

2.4.1. Carbonization temperature influence on mesoporous carbon nanospheres.

"Carbonisation temperature" is the key factor that dictates the physical, chemical, the electrical and mechanical behaviour of carbon-based nanomaterials [33]. Carbonization in itself is the most vital step in the synthesis of mesoporous carbon nanospheres

where the carbon precursors (such as polymers, resins, etc.) are converted into pure carbon structures at controlled elevated temperature conditions. Carbonisation increases the percentage of carbon content as well as introduces pores. As a result, the physicochemical properties the carbon nanomaterials possess such as adsorption capacity, solubility, hydrophobicity, crystallinity, etc., are also essentially brought about by influenced[23, 34, 35]. Studies were done on the effects of temperature during pyrolysis on carbon-based nanomaterials which showed, temperature change directly influences its performances in various applications such as fuel cells [83], catalysis[84], and gas separation[85], but this investigation has not been extended to the biomedical applications. While other carbon nanomaterials require functionalization and modifications to improve its colloidal stability in aqueous solutions; mesoporous carbon nanospheres show excellent colloidal stability modified with thermal changes during the carbonization process. Mesoporous carbon hollow spheres (MCHS) have shown excellent delivery performance in previous reports but at a fixed carbonisation temperature[28].

In 2001, Tse-Hao Ko et al. investigated the changes in the structure and crystallinity of the phenol-formaldehyde resin system that were carbonized and graphitized at from 300°C to 2400°C[35]. In their work, they traced the transformation of polymer resin into carbon framework using Raman spectra and X-Ray diffraction, Fig 6. They found that transformation of the phenolic resin into carbon starts at 500°C, no carbon structures are formed at a temperature below 400°C, and the original resin structure disappeared entirely above 600°C . As the carbonization temperature rose from 600°C to 1000°C, the carbon crystal size of the polymer resin increased. Moreover, above 1000°C the carbon started to graphitize as the stack size of carbon increase and the frequency of the G band and D band starts getting closer to 1582 cm^{-1} and 1357 cm^{-1} respectively.
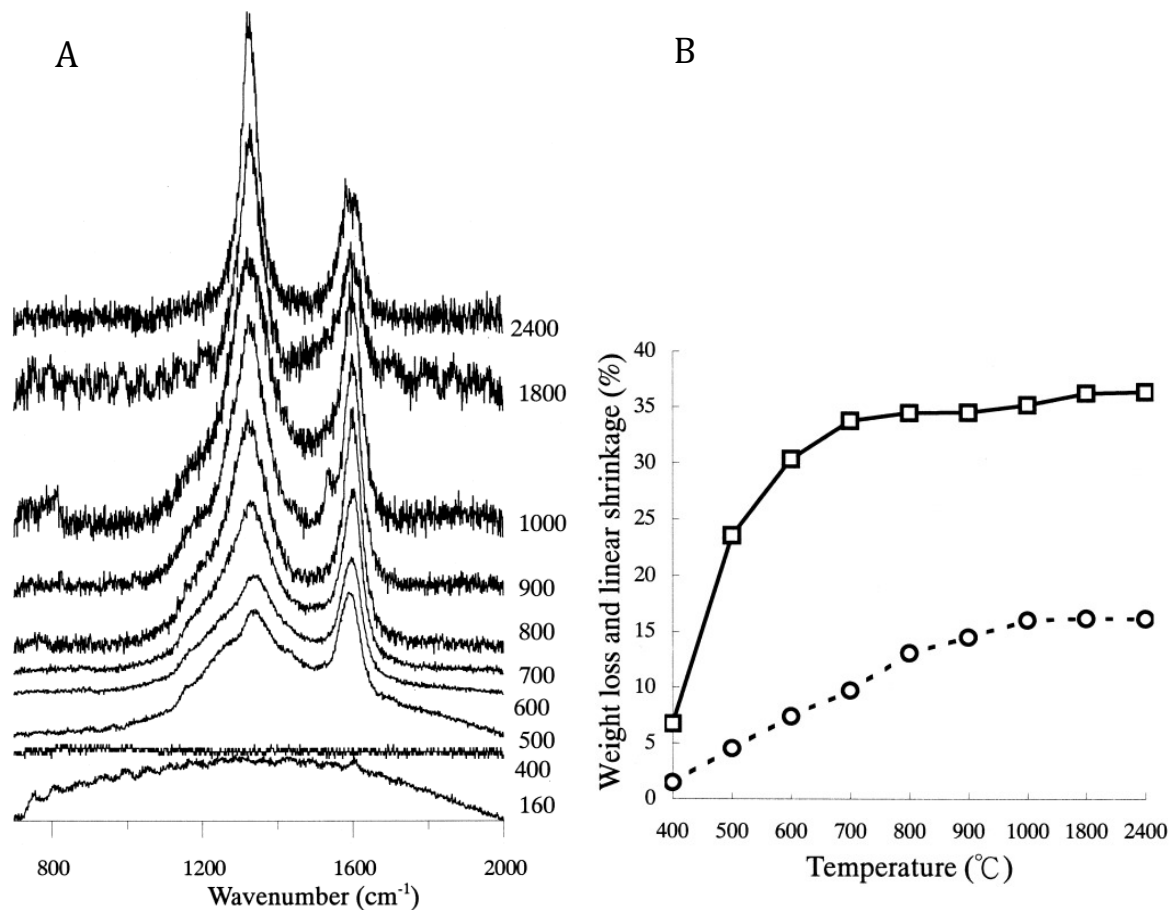
Fig 2.6. (A) The wide- angle X-ray diffraction pattern of cured resins during pyrolysis (B) The graph shows the variation of the weight loss and shrinkage of resulting carbonised resins as a function of the pyrolysis temperature (image courtesy reference[86])

The same group also observed the changes in the microstructure and physicochemical properties in the phenol-formaldehyde resin after carbonization at different temperatures. Their results showed carbonization temperature brings significant changes such as weight loss, shrinkage, pore formation, volume expansion, etc[86].

The studies demonstrated the importance of carbonization temperature, and it impacts on the structure and behaviour of carbon nanomaterials. Moreover, due to the changes brought about by the carbonization temperature their features can be tuned and optimized by tuning the carbonization temperature.

2.5. Carbon nanomaterials as ROS scavengers

Not only does carbon nanocarrier systems are excellent escorts for therapeutic drugs, but they are very efficient free radical ROS scavengers as well often attributed to their long conjugated C=C carbon chains[87]. Over the years, a plethora of research has suggested a direct correlation of the elevated level of ROS, i.e. an extended state

24

of oxidative stress, to major chronic diseases including cancer, rheumatoid arthritis (RA), neurogenerative diseases, acute ischemic injury, etc[14]. The current clinical recommendations for oxidative damage is to use classical antioxidants that have shown little to no benefit in the treatments.   Some of the popular antioxidants have been listed in Table 2. The factors that might be a reason for hindrance for the efficiency of the antioxidants are as following (i) they require additional enzymes to assist them in detoxifying the radical molecule (ii) limited number of radicals removed per antioxidant moiety (iii) production of other radicals due to antioxidant's mechanism intended to neutralise the free radicals[12, 88].

Table 2.2. Various antioxidants with their mechanism of action[88]

Antioxidants	Target ROS	Number of ROS removed per molecule	ROS generated	Detoxifying enzyme
SOD	$O_2^{\bullet-}$	2	H_2O_2	None
Catalase	H_2O_2	2	None	None
Glutathione peroxidase	H_2O_2	1	None	None
Glutathione	H_2O_2	1	None	Glutathione reductase
Vitamin E	$O_2^{\bullet-}$, $R^\bullet$	1	E	Vitamin C
Vitamin C	$E^\bullet$, $R^\bullet$	1	C	Dehydroascorbate reductase
Albumin	$HO^\bullet$	Unknown	None (presumably by disulphide formation)	None

PBN	$O_2^{\bullet-}$, $HO^{\bullet}$	1	Nitroxide free radical	None
Tempol	$O_2^{\bullet-}$, $ONOO^-$	1	H_2O_2, $NO^{\bullet}$	None
Fullerene derivative (C60)	$O_2^{\bullet-}$, $HO^{\bullet}$	Unknown	None	None
PEG- HCC	$O_2^{\bullet-}$, $HO^{\bullet}$	Estimated 10^6	H_2O_2	None

That is why particle-based systems are being considered as an emerging class of active antioxidants due to the possibility of complete quenching of radicles without the need for assistance from detoxifying molecules. Carbon materials such as SWCNT, MWCNT, graphene, fullerene or their other derivatives are being aggressively investigated as antioxidants owing to their potential to scavenge free radicals effectively.

In 2012, Brittany R. Bitner and co-workers tested PEG- functionalised hydrophilic carbon clusters (PEG-HCCs) as antioxidants to reduce the cerebral blood flow (CBF) in rat model inflicted with mild traumatic brain injury (TBI)/ hypotension/resuscitation. As elevated levels of ROS such as superoxide (SO) have been detected in the vasculature and spikes of ROS, have been found following a trauma; the damaging spikes in the level of ROS continue upon blood reinfusion during resuscitation and blood reinfusion which further ensues oxidative damage. The authors theorised, a potent, non-toxic clinical agent should be administered following the release of ROS that has ROS annihilation capabilities at a clinically realistic time point. So, in their work, they administered functionalized carbon clusters as therapeutic ROS scavenger. The results indicated that non-toxic PEG-HCCs normalised the oxidative radical profile and restored cerebral perfusion. Since cerebral perfusion following even a mild TBI is a vital cause of poor outcome, the ability of PEG-HCCs to restore ROS levels were supportive of a treatment that can potentially improve the neurological prognosis for traumatised patients.

Due to the high ROS scavenging capabilities of carbon nanomaterials, it has also been investigated for its ROS mediated immunomodulatory behaviour. Recently, in 2016, Redwan Huq and co-workers discovered that carbon nanomaterials as superior antioxidant agents could be utilised for cell- targeted immunotherapy. They reported functionalised carbon clusters which are known ROS scavengers have a preferential internalisation by T- lymphocytes over other splenic immune cells. They exploited this selectivity to inhibit T cell activation without affecting significant functions of macrophages, APC cells that are crucial for T-cell mediated inflammation in delayed hypersensitivity in experimental autoimmune encephalomyelitis (EAE, a model of multiple sclerosis). They assessed the consequences of PEG-HCC internalisation and found a significant reduction in intracellular ROS levels after administration of carbon nanoparticles. Consequently, ~30 % reduction in the intracellular pro-inflammatory cytokines such as T_H^1 cytokines, interleukin (IL)-2 and interferon (IFN)-γ were observed which are critical cytokines in autoimmune diseases such as multiple sclerosis. Moreover, after the histological analysis was conducted of the spinal cord grey matter collected from clinical models of rats with acute EAE, they found a decrease in inflammatory foci after 12-days post- immunisation. This suggested PEG-HCC reduced immune cell infiltration into the central nervous making it a potential and highly active antioxidant agent for immunomodulation for autoimmune diseases.

Fullerenes and its functionalized derivatives are one of the most popular nanomaterials that have exhibited high anti-oxidative capability in reducing ROS-induced injuries in biological systems. Empty fullerenes with big conjugated π-system can efficiently capture electrons and can be utilised as ROS scavengers. Although their low solubility restricts pure fullerenes in the hydrophilic environment; functionalized and modified fullerene have shown remarkable success as antioxidant carbon nanomaterials to alleviate detrimental effects of elevated ROS content. They have been studied for various ROS-induced injuries including ROS mediated cancer prevention strategies. In 2016, Jie Li and co-workers designed water-soluble metallofullerene $Gd@C_{82}$ (Ethylenediamine)$_8$ nanoparticles that exhibited remarkable cytoprotective effect against peroxide-induced injuries to human epidermal keratinocytes-adult (HEK-a) cells at a minuscule concentration of 2.5 µM. Using EPR analysis,Fig 7, they found that $Gd@C_{82}$ (EDA)$_8$ NPS had ~81% reduction in hydroxyl radical (OH•, the most common radical found in the human body). The cellular study

also indicated high intracellular scavenging activity by increasing the cell viability by approximately 20%, protecting the cells from ROS included injuries.
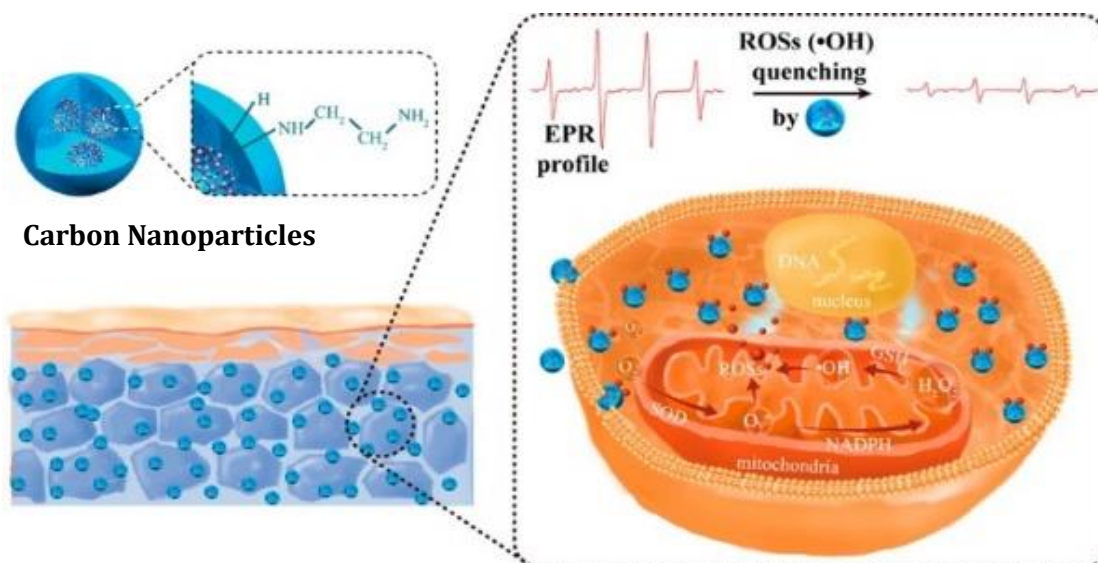
Fig 2.7. Diagrammatic representation of intracellular ROS scavenging ability of carbon nanoparticles[89].

Not only has that, but carbon nanoparticles also showed noteworthy resulted in the management of rheumatoid arthritis (RA). In 2009, Kazuo Yudoh and co-workers demonstrated that water-soluble fullerene carbon nanoparticles are great protective agents against synovitis in arthritis both *in-vivo* and *in-vitro.* They used adjuvant-induced arthritic rats were used as a model of arthritis. It was found that water-soluble C60 significantly suppressed the TNF-α induced production of proinflammatory cytokines in synovial fibroblasts, synovial infiltrating lymphocytes and macrophages in-vitro. Moreover, histological analysis of the ankle joint revealed C60 significantly reduced synovitis and alleviated bone resorption and destruction of in the joints compared to animals who were categorized as control groups.

All the above stated fascinating research points towards the fact that carbon nanomaterials have an excellent ROS scavenging ability that can be utilized as a potential therapeutic agent for various ROS mediated diseases.

2.6. Photothermal therapy (PTT) using carbon nanomaterials as photothermal agents

Photothermal therapy (PTT) or photothermal cancer therapy has garnered significant attention as an innovative cancer treatment strategy over traditional cancer therapies such as chemotherapy, radiation therapy and surgery. PTT strategy involves using specific light sources to induce heat, creating an environment of hyperthermia to kill cancer cells[90]. Interest in PTT started in the nineteenth century; however, it started to gain momentum in the 1980s owing to rapid development in optical and nanomaterial technology[91]. PTT is an effective cancer therapy that creates a state of hyperthermia after administration and light treatment, elevating the temperature to 40° C- 43°C[92]. Temperatures at this range have clinical significance as several cellular reactions such as protein denaturation, aggregation and cell inactivation occurs that disrupts or damages the cellular homeostasis in cancer cells causing lower survival rate, cell necrosis or cell apoptosis[91, 92]. Currently, PTT is being developed and encouraged for innovative cancer therapeutic strategy. This strategy is useful and attractive as it blends the unique advantages of being highly selective/ specific with minimum invasiveness. If the proper photoabsorbers / photothermal agents are employed in PTT, it can directly eradicate the cancer cells in a primary tumour or local metastasis to combat the initial stage of cancer metastasis and can also be employed in combination with current therapeutic modalities. The strategy has been graphically represented in Fig 2.8. This helps achieve the precise heating of the cancerous region.

Rapid developments in nanotechnology have allowed the investigation of a variety of specialised nanomaterials such as conducting metallic and semiconductor materials[93], organic polymers[94], quantum dots[95], carbon nanomaterials[91] for *in vitro* as well as *in vivo* PTT. Carbon nanomaterials have proven to be excellent choices for photothermal agents as they have desirable properties such as i)relatively higher absorbance of light wavelength (nm) ii)good biocompatibility iii)good dispersion in biofluids such as blood[91]. Taking advantage of the ability of carbon nanomaterials to harvest light, convert it into heat and biocompatibility, they are being investigated for potential candidates for "photothermal therapy" (PTT) as "photothermal agents" or "theranostic agents". Carbon-based nanomaterials such as CNT, carbon nanohorns and graphene have been extensively studied as potential PTT agents[96-98].
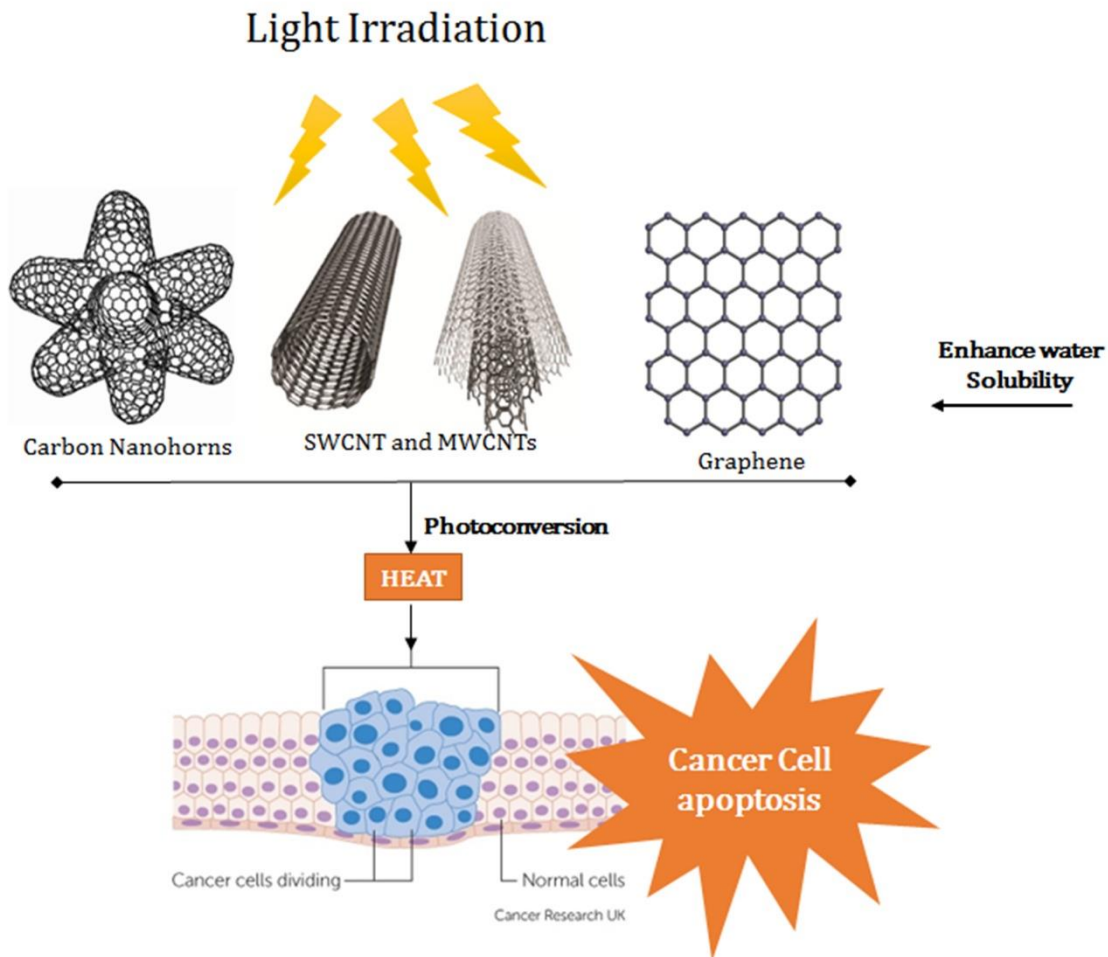
Fig 2.8. Schematic representation of PTT therapy using carbon nanomaterials as photothermal agents

Most of the investigation has been done using carbon nanotubes for potential PTT application for cancer therapeutics. In 2009, Hye Kyung Moon et al. used single carbon nanotube as a photothermal therapeutic agent to treat a localised tumour *in vivo*, represented as a scheme in Fig 2.9[96]. In their work, they induced human epidermoid mouth carcinoma KB tumour cells via xenograft on mice's backs. Approximately 120mg/L, 100µL of PEG-SWNTs were injected into the tumour region, and the near-infrared laser was irradiated for 3 min. Post-treatment they observed that when PEG-SWNTs were combined with laser irradiation, by the 14th day of treatment, there was a noticeable reduction in the tumour volume whereas, by the end of 20 days of treatment, the tumours were destroyed entirely. They also observed a residual black mark on the skin as a burn mark which was direct evidence of excessive local heating caused by the photothermal agents by the laser irradiation.
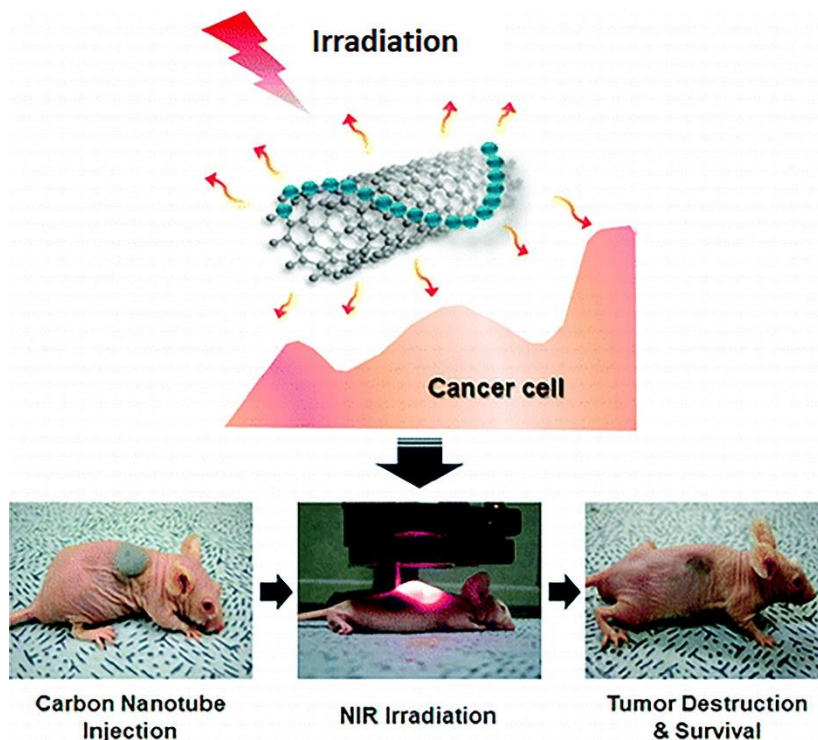
Fig 2.9. Schematic diagram representation of carbon nanotubes used in cancer cell ablation in PTT (image courtesy ref96)

Another exciting work on carbon nanomaterials came from Daiqin Chen and co-workers in 2014 who demonstrated photoacoustic imaging-guided NIR photothermal therapy using carbon nanohorns as theranostic agents[99]. In their work, they used single-walled carbon nanohorns (SWNHs) as photothermal/theranostic agent and functionalised it C_{18} PMH-PEG to optimise their EPR effect, enhance their accumulation in the tumour site and diminish toxicity in pristine form. Firstly they conducted cell growth inhibition assay where they tested the ability of nanomaterial to inhibit the growth of 4T1 cells either with or without laser irradiation. They observed after incubation of 4T1 cells, only after irradiation of laser at a specific power density of 0.6 Wcm^{-2} was there significant inhibition of the tumour cells. Furthermore, they took a 4T1 tumour bearing female Balb/c mice and intravenously injected with SWNHs/C_{18} PMH-PEG (2mg mL^{-1}, 200μL) and tested the photoacoustic image of a tumour and tumour ablation capabilities of the nanomaterials after laser irradiation. After calculating the mean signal intensity and maximum mean signal intensity of the region of interest, they found excellent photoacoustic effect which kept intensifying after ~24 hours post-injection. They also tested the photothermal ablation of tumour post 24 hours of i.v injection and exposure of the tumour region to a laser with a power density of 0.4 Wcm^{-2}. They observed that the temperature reached almost ~55°C after irradiation, the tumour size shrunk significantly, and the mice made a full recovery after 16 days of treatment. Similar to Hye Kyung Moon's (mentioned above), the tumour

31

site was left with black scar (crust) indicating the thermal ablation and regrowth of body hair on the site without recurrence of a tumour.

Among the carbon nanomaterials family, carbon nanotubes are the most popular choice when it comes to photothermal therapy. However, its sister "graphene", has not been far behind. In work done by Kai Yang and co-workers, they tested the photothermal ablation efficiency of PEG-functionalized graphene nanomaterials *in-vivo*. When they used a NIR laser with a power density of 2 Wcm^{-1} in an aqueous solution, they observed rapid rise in the temperature within a very short period. They also tested the PEG functionalized nanographene sheets on 4T1 tumour model on Balb/c mice. Then they injected 200μL of carbon nanomaterial in the tumour region and irradiated the site for 5 min after 24-hours post-injection. They found the surface temperature of ~50°C in contrast to uninjected mice which reached to just ~2°C. The survival curves of the mice showed all the mice treated with photothermal treatment survived over 40 days without any single death.

Studies on the potential advantages of using carbon nanomaterials as photothermal agents are pretty promising, with significant shrinkage of a tumour and high mice mortality rate, carbon nanomaterials have geared themselves for possible future medical cancer diagnosis. However, when it comes to photothermal agents from carbon family, mesoporous carbon nanospheres might have the upper hand owing to its porous structure in combination with the photothermal property of sp2 carbon nanomaterials. Mesoporous carbon nanospheres are hybrid nanocomposites that can be utilized for drug storage in the nanopores and can convert heat from light irradiation, making it a better performer for photothermal cancer therapy. This advantage of mesoporous carbon nanospheres was investigated by Guiju Xu and co-workers in 2014. Their group used functionalized mesoporous carbon nanospheres for a combination of cancer therapy that includes chemotherapy and photothermal therapy acting as synergists with a common goal of cancer cell destruction. In their work, they modified the mesoporous carbon nanospheres with folic acid for targeted chemotherapy, loaded doxorubicin hydrochloride (DOX) taking advantage of the high loading capacity and treated Hela cells following with photothermal therapy. When they subjected the nanoparticles to the Hela cells, they found that cytotoxicity of 25μg mL^{-1} carrying an equivalent of 13 μg mL^{-1} of DOX killed 64 % of the cells, whereas when the dose was combined with photothermal therapy, the cellular inhibition increased to 74%. Thus, mesoporous carbon nanospheres demonstrated the ability to significantly

enhance their cancer therapeutic efficiency with its photothermal efficiency being applied in combination with chemotherapy.

2.7. Conclusion:

Cancer therapeutic practices have gotten a whole new spin after the introduction of nanocarrier systems. Nanocarrier systems allow us to exploit relatively potent and safer therapeutic proteins or biomolecules to treat cancer / tumour cells without sacrificing its effectiveness or damaging its fragile structure. This has the potential to give rise to the next generation of chemotherapeutic treatment that will be safer and efficient method than conventional chemotherapy. Among the various nanocarrier systems that have been developed over the years, carbon nanocarrier systems such as CNTs, graphene, fullerenes, nanohorns, C-dots, mesoporous carbon nanospheres, etc., have made their own mark while proving their efficacy. Their uniquely hybridised carbon structures, inherent hydrophobicity, high surface area, high drug loading capacity, controlled release pattern, biocompatibility and high cellular uptake puts them into an enormous advantage over other groups of nanocarrier systems. Among the various carbon nanocarrier systems been investigated so far, mesoporous carbon nanospheres possess numerous benefits that make us consider them for numerous biomedical applications. Mesoporous carbon nanospheres have all the benefits of sp2 hybridized carbon materials along with an open porous framework with the large surface area . Thus, it achieves high loading capacity, high cellular delivery and controlled release of the load with high cellular interaction. They also enjoy high colloidal stability which can be achieved by conditional optimization. Mesoporous nanocarbon nanomaterials fabricated using nano casting method employing a hard porous silica template gives better control of the structure and porosity of the nanomaterials. First, they synthesize the porous silica template followed by infiltration of the template with carbon precursors. Then the polymer-silica matrix is carbonised, and at the final stage, the silica template is removed leaving us with the porous carbon framework. "Carbonization" is a vital step in the fabrication process as it dictates the carbon content, formation of C=C chains, morphology, crystallinity, etc., which determines the physicochemical properties of the mesoporous carbon nanospheres. In this PhD thesis, we have carried systematic study of the structural, chemical and behavioural changes occurring in mesoporous carbon spheres upon carbonization at various temperatures. In chapter 4 we synthesised mesoporous carbon hollow spheres (MCHS) using the one-pot synthesis method using porous silica particles. We primarily focused on the carbonization of polymer and silica matrix into carbonaceous

frameworks and their physicochemical changes at various temperatures. We also investigated the trend of the cellular interaction of the mesoporous carbon nanospheres carbonised at different temperatures in order to figure out the "optimised temperature" that can elicit the highest intracellular therapeutic delivery performance.

In chapter 5 we discussed the potential application of MCHS as free radical scavengers. As long conjugated carbon chains are attributed to the free radical scavenging that can also be beneficial for various ROS related ailments. In this PhD project, we dived into the potential of MCHS as efficient ROS scavenging nanoparticles. We also investigated whether the carbonization temperature influences the ROS scavenging ability of the nanoparticles or not. Furthermore, we tested MCHS after intracellular and its ability to diminish oxidative stress which is a ubiquitous sight in a tumour or cancer cellular environment. This included MCHS carbonised at an optimized temperature which shows the highest scavenging efficiency being compared with conventional and popular ROS scavengers as well as with other carbon nanocarrier systems.

The versatility of MCHS was extended in chapter 6 where we investigated the photothermal property of MCHS. Carbon nanocarrier systems are also great facilitators of photothermal conversion of pointed incident light into heat. This heat can be harvested to kill cancer cells and act as a synergist support nanocarriers that can carry therapeutic drug molecules and release them in the cytosol of the cancer cell while upconverting projected light into heat resulting in higher cancer cell cytotoxicity. We tested the photothermal of MCHS prepared at various carbonization temperatures under aqueous conditions. We also tested cancer cellular toxicity of optimised MCHS carrying HSP90 protein inhibitor (a drug molecule that inhibits the resistance of cancer cells to photothermal damage) and its photothermal ablation in MCF7 breast cancer cells.

Chapter 3
Methodology

This chapter summarizes the strategies utilized in the whole PhD project, including a synthetic method for the preparation of MCHS-*T.* It also discusses the methods and instruments used for the characterisations, detection methods and evaluations.

3.1. Material Synthesis

Mesoporous Carbon Hollow Spheres (MCHS) were synthesised using the hard templating method. MCHS was obtained after carbonising silica/polymer composite, where silica played the role of the hard template whereas the remainder carbon shell was a result of the pyrolysed polymer matrix. Tetrapropyl orthosilicate, TPOS; was the choice for silica precursor whereas Resorcinol Formaldehyde, RF; was used as the polymer source considering their suitable polymerisation kinetics for forming a sizeable mesoporous volume. At first, TPOS was added to the solvent system to hydrolyse, then self- assemble and homogenously nucleate to form monodisperse Stöber spheres, which acted as silica core. Later, the added RF precursors start to polymerise and initiate the heterogeneous nucleation process by growing on the surface of the silica core. At the reaction time, reaches the ~ 2-hour mark, the RF oligomers starts to co-condense along with primary silica particles and interact through weak hydrogen bonding forming a $SiO_2@SiO_2/RF$ core-shell structure. The SiO_2/RF shell continuously increases in thickness as the reaction continues and the size of the mesopores in the final structure is determined by the size of the silica aggregates co-condensing along with the polymer oligomers. Since TPOS has a high concentration of slow silica primary particles, it favoured the formation of large aggregated silica particles co-deposited with the RF oligomers causing large mesopores to form. After the final $SiO@SiO_2/RF$ matrix is formed, they were carbonised where the RF polymer was converted into carbon crystals. The carbonisation temperature plays a vital role in

determining the carbon crystalline symmetry, structure, chemical bonding, carbon content (percentage), etc., which in turn influenced its functionality and applications.
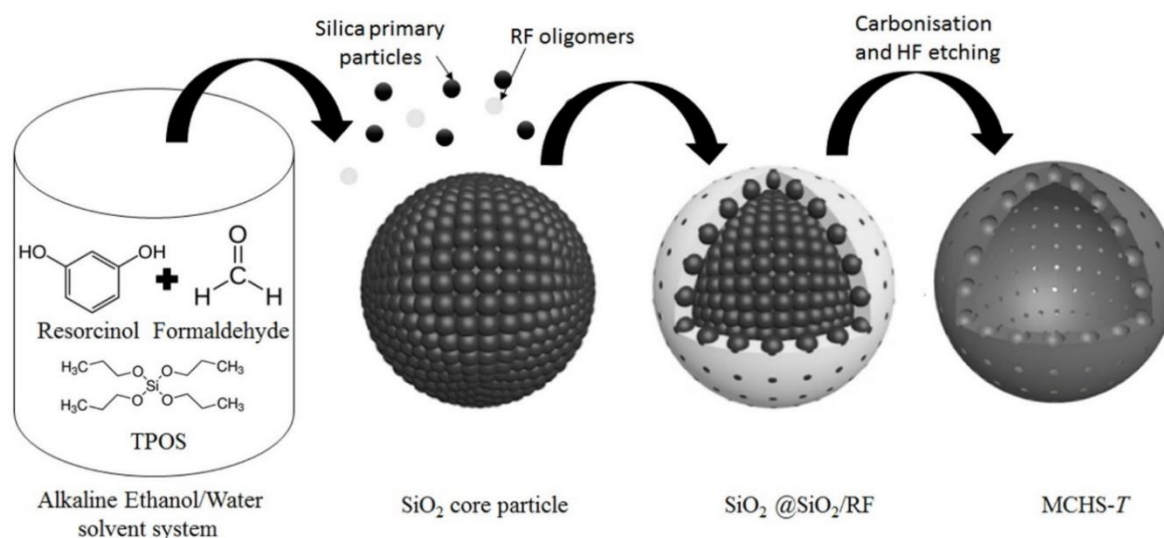
Scheme 3.1. A schematic representation of the one-pot synthesis of MCHS-*T*

3.2. Material characterisation

3.3.1 Transmission electron microscopy

Transmission Electron Microscope (TEM) is a high-resolution imaging tech nique which utilises energetic electrons to provide morphologic, compositional and crystallographic information even on small volumes of samples. TEM is a powerful microscope with a maximum potential magnification of 1nm producing precise 2D images of the desired samples. In our work, TEM was crucial to carry structural characterisation of the local structure of samples [1, 2]. In this PhD project, all the TEM images were taken using the JEOL 1010 microscope operated at 100 kV. Sample specimens were dispersed in ethanol and deposited on TEM copper grid and allowed to dry in air for a few seconds, before taking the images.

3.3.2 Scanning electron microscopy

Scanning electron microscopy (SEM) was used to analyse the morphology and surface properties of the synthesised particles. SEM uses a focussed beam of high-energy electrons to generate various signals at the surface of the solid specimen giving us information about the texture (external morphology), crystalline structure and orientation of the materials of the specimen composition[100]. We used a field emission

scanning electron microscope (FESEM, JEOL 7001) operated at 15kV in our studies. High-resolution scanning electron microscopy (HRSEM) images were obtained on JEOL JSM 7800 FE-SEM equipped with an in-column upper electron detector (UED) and gentle beam technology operated at a lower accelerating voltage of 0.8-1.5 kV. For SEM measurements, samples were prepared by dispersing the powder samples in ethanol after which they were deposited on to aluminium foil, attached to conductive carbon film on SEM stage. Then the prepared samples were kept for baking overnight in a vacuum oven at 70°C before imaging.

3.3.3 Nitrogen sorption measurements

Nitrogen adsorption measurements determined the investigations concerning the assessment of physical properties such as surface area, microporosity and mesoporosity, pore size distribution and pore volume of the particles. It measures the amount of nitrogen that adsorbs onto the subject of interest; regression analysis is then applied to the data resulting in the isotherm. Nitrogen sorption isotherms of the samples were obtained at -196 °C using a Micrometrics Tristar II system. Before the measurements; the samples were degassed at 180 °C for 12 h in vacuum. The total pore volume was calculated from the amount adsorbed at maximum relative pressure (P/P$_0$) of 0.99. The Barrett-Joyner-Halenda (BJH) method was used to calculate the pore size of samples from the adsorption branches of the isotherms. The Brunauer-Emmett Teller [101] method a.k.a., BET was utilised to calculate the specific surface areas.

3.3.4 Dynamic Light Scattering

Dynamic light scattering (DLS) usually referred to as a Quasi-Elastic Light Scattering (QELS) was used in this PhD work to measure the size, size distribution as well as the level of polydispersity of the particles in aqueous solutions and culture media. DLS is a well- established technique that uses Non-Invasive Back Scattering (NIBS) technology, which detects the Brownian motion of the particles in the suspension causing the laser light to scatter at different intensities[102]. The fluctuations in the light intensities vary according to the velocity of the Brownian motion of the particles within the suspension. The variations in the intensities are analysed, and the particle sizes are estimated using the Stokes-Einstein relationship[103]. The size of the particles was measured in nanometres whereas the polydispersity was measured in scales of PDI (Polydispersity Index). According to IUPAC recommendations, PDI is the "degree of

non-uniformity" of distribution of particles, where PDI=0.0 signifies perfectly uniform, PDI 0.0-0.1 signifies narrow monodispersion, PDI 0.1-0.4 signifies polydispersion. The hydrodynamic sizes of particle samples in this PhD project were measured using Malvern NanoZS Zetasizer at 25 ∘C in phosphate buffer solutions (PBS) and DMEM culture media.

3.3.5 Elemental Analysis

To analyse and quantify the elemental composition of the synthesised nanomaterials we used Elemental Analysis (EA). For this PhD project, we used CHNS-O Analyser (Flash EA 1112 series, Thermo Electron Cooperation) to determine the percentage of elements of carbon (C), nitrogen (N), hydrogen (H) and oxygen (O), according to the dynamic flash combustion (modified Dumas method).

3.3.6 Raman Spectroscopy

Raman spectroscopic techniques is a well-recognised practical method of chemical analysis and characterisation applications since the discovery of "Raman Effect" in 1928 by renowned Indian physicist Sir C. V. Raman. We characterised our synthesised particles using Raman spectroscopic analysis to get more insight into the structural and chemical differences in different samples. Renishaw Raman Microscope and Spectrometer were used for the analysis, which has an accuracy of one wavenumber equipped with three laser wavelengths (325nm, 514nm and 785nm) for Raman vibrational analysis.

3.3.7 X-Ray Photon Spectroscopy

X-Ray Photon Spectroscopy (XPS) is an excellent, non-destructive spectroscopic technique to analyse the surface chemistry of particles[104]. In this PhD work, we used Kratos Axis Ultra photoelectron spectrometer with a monochromatic Al Kα (1486.6 eV) X-ray source to analyse our samples for surface chemical composition. Each spectrum was recorded at a survey scan from 0 to 1200 eV with a dwell time of 100 m, and pass energy of 160 eV at steps of 1 eV with one sweep.

3.3.8 Electron Paramagnetic Resonance Spectroscopy

Electron paramagnetic resonance (EPR) (or synonymously electron spin resonance (ESR)) is a magnetic resonance technique used to investigate materials with unpaired

electrons such as free radicals, transition metal ions and clusters. EPR analysis provides essential information that can be applied to studies of nanomaterials, materials science, biology, chemistry, food science, radiation dosimetry and medicine. EPR analysis was essential to investigate the number of free radicals present before and after the addition of the synthesised particles to measure the free radical scavenging activity of particles. Bruker Elexsys E580 Pulsed Q-, X-band (with high power microwave amplifiers) for variable temperature (1.5-300K) EPR / ENDOR / ELDOR / ESEEM / DEER Spectrometer was used to carry out the analysis for this work.

3.3.9. Thermo Scientific™ Nicolet™ 6700 FT-IR spectroscopy

Fourier transform infrared (FTIR) spectroscopy was utilised to trace the carbon bonding of different MCHS-*T*. The powder of samples was added merely onto the crystal to obtain optimal contact. FTIR spectra were collected using the Thermo Scientific™ Nicolet™ 6700 FT-IR spectrometers. Each spectrum was obtained using dried powder against a background measured under the same condition. For each spectrum, 128 scans were collected at a resolution of 4 cm^{-1} over the range 400–4000 cm^{-1}.

3.3.10. UV-2450 Shimadzu Spectrophotometer

 UV-2450 is a universal research grade spectrophotometer that can be used in a wide range of fields and can easily be expanded to suit the measurement objective. It was used to measure the absorbance of spectra from 200 nm-900 nm with just one scan. It was used to measure the optical properties of nanoparticles.

3.3.11. NanoDrop^{TM} 1000 Spectrophotometer

NanoDrop-1000^{TM} Spectrophotometer is full spectrum robust UV-Vis spectrophotometer used for quantification and evaluation of purity of samples such as proteins and nucleic acids. It has a full spectrum (220-750 nm). Spectrophotometer utilizes a patented retention technology that employs surface tension alone to hold the sample in place. This allows for the analysis of sample sizes as small as 0.5 μl. The high absorbance capability of the instrument is reported to be 50 times that of

traditional spectrophotometers. In this thesis, the concentration of highly sensitive HSP protein inhibitors was measured using NanoDrop-1000^{TM} Spectrophotometer to quantify the amount absorbed in the nanocarriers and the amount released in the solutions at different time points.

3.4.12. TECAN Infinite® 200 PRO

The Infinite®200 PRO is an efficient multi-mode, easy-to-use plate reader that offers high-performance detection solutions by monochromator- or filter based technologies. The readers offer up to six detection modes for sample measurements in 6- to 384-well plates, PCR plates or cuvettes, based on the Quad4 Monochromators Infinite M and filter-based Infinite F configurations. Three sets of advanced optics and three high-performance detectors – optimised for the requirements of fluorescence, luminescence and absorbance reading – allow uncompromised performance in all detection modes. This detector is often used in various vital applications such as UV-Viz detection, DNA/RNA/protein quantification absorbance based ELISA, chemiluminescent ELISAs and many more.

3.4 Biological Characterisations
3.4.1 Confocal Laser Scanning Microscopy

Confocal Laser Scanning Microscopy (CLSM), an advanced imaging technique was used to obtain precise and clear images of biomaterials and the biological specimens. For this PhD project, ZEISS LSM 710 was used to capture the fluorescence of dye molecules loaded on the biomaterials and their cellular interactions. ZEIS LSM 710 is a laser scanning confocal microscope with advanced imaging capabilities that offers high sensitivity and superior signal to noise ratio, which has 34 channel detectors to monitor changes of multiple fluorophores. Bright field images were also obtained as the microscope can be flexibly selected with two flanking photomultipliers (PMT) channels and a 34 channel PMT array.

3.4.2 Flow Cytometry

Flow cytometry is a favourite analytical technique in cell- biology that utilises light to count and profile cells and its complexity in a heterogeneous fluid mixture. It is used extensively throughout life and biomedical sciences where researchers need to rapidly profile a large population of cells in media, forex, identifying, separating and

characterising immune cell subtypes by their size and morphology. In this PhD, project the intracellular uptake of fluorescent-tagged carbon particles, protein delivery, and intracellular ROS levels were quantified using BD LSR-II Analyzer (USA). The results were analysed by FlowJo Software.

3.4.3. MTT Assay

MTT assay involves using MTT 3-(4,5-dimethylthiazol-2-yl)-2,5-diphenyltetrazolium bromide, a yellow tetrazolium salt which gets reduced to purple formazan in living cells [105]. A solubilisation solution such as dimethyl sulfoxide (DMSO) is added to dissolve the insoluble purple formazan product into a coloured solution. The absorbance of this coloured solution is measured at a particular wavelength (usually between 490 nm and 600 nm) by UV-Vis spectrophotometer. MTT assay is a well-established colourimetric assay for assessing cell metabolic activity. In viable cells the NAD(P)H-dependent cellular oxidoreductase enzymes under defined conditions which reflects the number of viable cells present. These enzymes are capable of reducing the tetrazolium dye MTT to its insoluble formazan, which has a purple colour. In this PhD thesis, MTT assay was used to assess the cytotoxicity of nanocarriers delivering active bio/drug molecules into the cytosol of the cancer cells causing the ablation of cancer cells.

Chapter 4

Mesoporous Carbon Hollow Spheres: Carbonisation-Temperature-Dependent Delivery of Therapeutic Proteins

This chapter reports the influence of carbonization temperature of mesoporous carbon hollow spheres (MCHS) on their delivery performance of therapeutic protein. **This work has been published in Journal of Material Chemistry B, 2018; 5, 763-768.**

4.1. Introduction

Protein-based therapeutics are gaining increasing popularity for disease and cancer treatment because of their higher specific functions and fewer side effects over small molecule drugs.[106, 107] However, the fragile structures and poor cell membrane permeability of therapeutic protein molecules have impeded the broad applications of protein therapeutics. Exploiting nanocarrier systems has revolutionised the therapeutic practices of protein molecules by overcoming these issues with enhanced therapeutic efficacy.[8, 108] Various leading nanocarriers systems have been developed, including polymers, lipids, micelles, quantum dots, gold nanoparticles, mesoporous phosphosilicate nanoparticles and, carbon nanoparticles.[108, 109] Recently, the pristine mesoporous carbon nanospheres have stood out as a promising candidate with advantages of large pore sizes, excellent safety profile and hydrophobic nature for efficient therapeutic protein loading.[110]

Mesoporous carbon nanospheres are generally derived from the polymer sources under the heating process in a nitrogen environment,[28] in which the treated carbonisation temperature determines the physicochemical (e.g. hydrophobicity and crystallinity), electrical and mechanical properties behaviour of final products.[33, 23, 34, 35] Studies were done which demonstrated that carbonisation temperature on carbon nanomaterials profoundly influenced their performance in fuel cells,[83] catalyses,[84] and gas separation.[85] When using as nano-carriers for therapeutic protein delivery, it remains unknown what the effect of carbonisation temperature of mesoporous carbon spheres has on their delivery performance.

Herein, for the first time, we reported the impact of carbonisation temperature of mesoporous carbon hollow spheres (MCHS) on their delivery efficiency of therapeutic proteins and correlated with physicochemical properties determined by carbonisation temperature. MCHS-T samples were prepared at various carbonisation temperature (T=500, 700, 900 °C) and characterised. The carbonisation temperature difference, Δ°C, was kept at 200° C as it played a significant role in terms of "replication" (a classic statistical definition of an intervention or treatment) in experimental units[111]. Trial tests with several temperature differences ranging from, Δ°C, 50° C to 200° C, we observed that 200° C is the minimum temperature change the nanoparticles needed to acquire the morphological, structural and physicochemical variations to determine the contribution of carbonisation temperature in delivery efficiency in cell culture studies and acquire statistical significance. It was found that the pore size, pore volume and

hydrophobicity of MCHS increased as *T* increasing, mainly from 500 to 700. RNase A was chosen as a model of therapeutic proteins. MCHS-900 possess the highest loading capacity and most sustained release of RNase A, contributed by the high hydrophobicity and large pore size. RNase A delivered by MCHS-900 showed the best therapeutic efficacy with significant inhibition of human squamous carcinoma cells (SCC25), comparing to free RNase A or those delivered by MCHS-500 and MCHS-700. Also, MCHS-900 significantly promoted intracellular delivery of RNase A and subsequent endo/lysosome escape in SCC25 comparted to the other MCHS carriers, which are crucial for protein therapeutics.
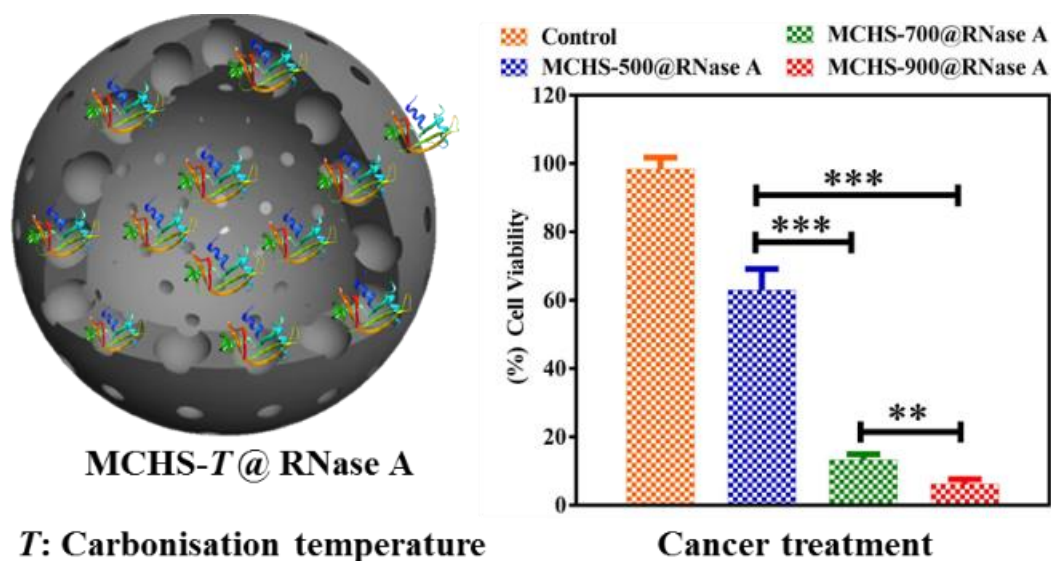
Scheme 4.1. Schematic representation of mesoporous carbon hollow spheres optimised by carbonization temperature for intracellular therapeutic protein delivery and the cancer cell cytotoxicity.

4.2. Experimental section

4.2.1. Characterizations

Transmission Electron Microscopy images were taken using a JEOL 1010 microscope operated at 100 kV. The TEM specimens were dispersed in ethanol and then transferred to a copper grid. For Scanning electron microscopy (SEM) measurements, the samples were prepared by dispersing the powder samples in ethanol, after which they were dropped to the aluminium foil pieces and attached to conductive carbon film on SEM mounts. The SEM mounts were heated in a vacuum oven at 70 °C for at 8 hours before observations. Nitrogen sorption isotherms of the samples were obtained at -196 °C using a Micromeritics Tristar II system. Before the measurements, the samples were degassed at 180 °C overnight in vacuum. The BET surface area was

calculated using experimental points at a relative pressure of P/P_0 = 0.05- 0.25. X-ray photoelectron spectroscopy (XPS) analysis was conducted using a Kratos Axis ULTRA X-ray photoelectron spectrometer. Peak fitting was carried out using the Casa XPS software. Elemental analysis (EA) was performed with a CHNS-O Analyzer (Flash EA1112 Series, Thermo Electron Corporation). The Raman analysis was done using the Renishaw Raman microscope. The particle size distribution profiles were collected at 25 °C using a Zetasizer Nano-ZS from Malvern Instruments.

4.2.2. Loading and Release Study

RNase A loading test was measured using "Bradford Protein Assay" (a spectroscopic analytical technique). Firstly, a stock solution of 2 mg mL^{-1} of RNase A was prepared in a PBS buffer solution. 1 mg of MCHS-*T* was dispersed in a 0.5 mL of PBS and ultrasonicated for 5 min to disperse MCHS-*T* in the solution thoroughly. Then 1.5 mL of RNase A stock solution was added to MCHS-*T* previously dispersed in PBS, in a 2mL Eppendorf tube. The tubes were kept in an incubator shaker for 24 h, shaken at a speed of 200 rpm, maintained at a temperature of 25°C in the dark. After the designated time, the tubes were centrifuged at 15000 rpm after which the supernatant was collected for spectrophotometric analysis. The collected supernatant was treated with Bradford reagents, and the concentration of RNase A was measured in a UV-Vis spectrophotometer at 277.5 nm. The decrease in concentration of protein was indicative of protein adsorption capacity. The release study was conducted by re-suspending the residual precipitate in fresh PBS solution and shaken in the incubator shaker at 200 rpm at 37 °C. The tubes were collected at specific intervals, centrifuged at 15000 rpm while 1 mL of the supernatant was replaced with fresh PBS solution. The protein concentration in the supernatant was determined by the same method to calculate the cumulative release profile.

4.2.3. Media preparation

The human squamous carcinoma (SCC 25) cells were grown in complete Dulbecco's modified Eagle's medium and Ham's F12 medium (DMEM/F12), supplemented with fetal calf serum (10%, FCS), L-glutamine (1%), penicillin-streptomycin (10,000 U mL^{-1}), 0.5 mM sodium pyruvate and 400 ng/mL hydrocortisone. For subculturing purposes, the cells were washed with sterile PBS solutions and trypsin (0.25 g L^{-1}). The cells were attached to T75 flasks and incubated at 37 °C under 5% CO_2 sterile environment.

4.2.4. Toxicity Assay

Cellular toxicity assay of MCHS-*T* was conducted after exposing the carcinoma cells with loaded RNase A, incubating for a required period and counting the viable and non-viable cells using haemocytometer. SCC-25 cells were seeded in a 24-well plate at a density of 0.05×10^6 cells/well. Then the cells were incubated overnight at 37 °C. After the overnight incubation, the cells were treated with a solution of MCHS-*T* loaded with RNase A, where the final concentrations of the loaded RNase A were 10, 25 and 50 µg mL^{-1}. To evaluate the cytotoxicity of carbon spheres, they were diluted in 2-fold series in the culture medium and incubated for 24 and 72 h. The safety of the pure MCHS-*T* was elucidated by treating SCC25 cells to 10, 25 and 50 µg mL^{-1} of bare MCHS-*T* as negative controls. After 24 and 72 h, the culture medium from each sample was collected, and cells were detached by incubating with 100 µL of 0.25% trypsin/EDTA mixture. Detached cells were then mixed with the medium previously collected from the sample. The cell suspension was diluted with Trypan Blue reagent in a 1:1 ratio. Live and dead cells were counted on a "haemocytometer". Cell viability was calculated using the following formula:

$$\text{Cell viability (\%)} = \frac{[\text{viable (live)cell count}]}{[\text{Total (live+dead)cell count}]} * 100$$

4.2.5. Confocal imaging

SCC25 cells were seeded on sterile glass coverslips kept a 6-well plate (Nalge NUNC International, Rochester, New York) at a seeding density of 1.5×10^5 cells per well and cultured overnight at 37 °C in DMEM/F12 media. Simultaneously FITC conjugated RNase A (FITC-RNase A) was loaded in MCHS-*T* particles (FITC-RNase A@MCHS-*T*) following the same process as described in the protein loading section, at a feeding ratio of 2:1. The loading was estimated by detecting the change fluorescence using TECAN Infinite 200 Pro. FITC-RNase A@MCHS-*T* samples along with the control group (RNase A in PBS) were added to the culture media at a final RNase A concentration of 25 µg mL^{-1}. One set of cells were incubated for 1 h whereas the second set for 6 h at 37 °C. Afterwards, the media was removed, and the cells were washed with sterile PBS. After adding fresh serum-free media, Lysotracker Red DND-99 was added at a concentration of 50-75 nM in the media. The cells were incubated for 30 min at 37 °C, then washed twice with PBS. The sterile glass coverslips were treated with 0.5 mL of 4% w/w paraformaldehyde solution to fix the cells followed by incubation overnight at room temperature. In the end, images were taken using the Zeiss LSM 710 META confocal microscope (Carl Zeiss, Thornwood, New York).

4.3. Results and discussions

MCHS-T samples were synthesised using silica templating method via a one-pot synthesis method. SEM images of MCHS-500, MCHS-700 and MCHS-900 are shown in Fig 4.1A-C, respectively. MCHS-500 displays an aggregated, non-uniform and partially concaved spherical morphology (Fig 4.1A). In contrast, MCHS-700 and MCHS-900 both show spherical morphologies with uniform particle sizes of ~ 170 nm in diameter (Fig 4.1B and C). The structural differences in MCHS-T samples were examined using TEM. MCHS-T samples all exhibit a hollow spherical structure, owing to their formation mechanism as reported previously.[28, 75] However, the TEM image of MCHS-500 indicates that the wall of hollow spheres is deformed or partially collapsed (Fig 4.1D), consistent with the SEM observation in Fig. 1A. Moreover, the mesopores within the wall are not evident. For MCHS-700 (Fig 4.1E) and MCHS-900 (Fig 4.1F), the intact hollow spherical morphology and the mesopores in the wall are clearly seen. Collectively, both SEM and TEM results have demonstrated that the carbonisation temperature has a significant impact on the final structure of MCHS-T samples.
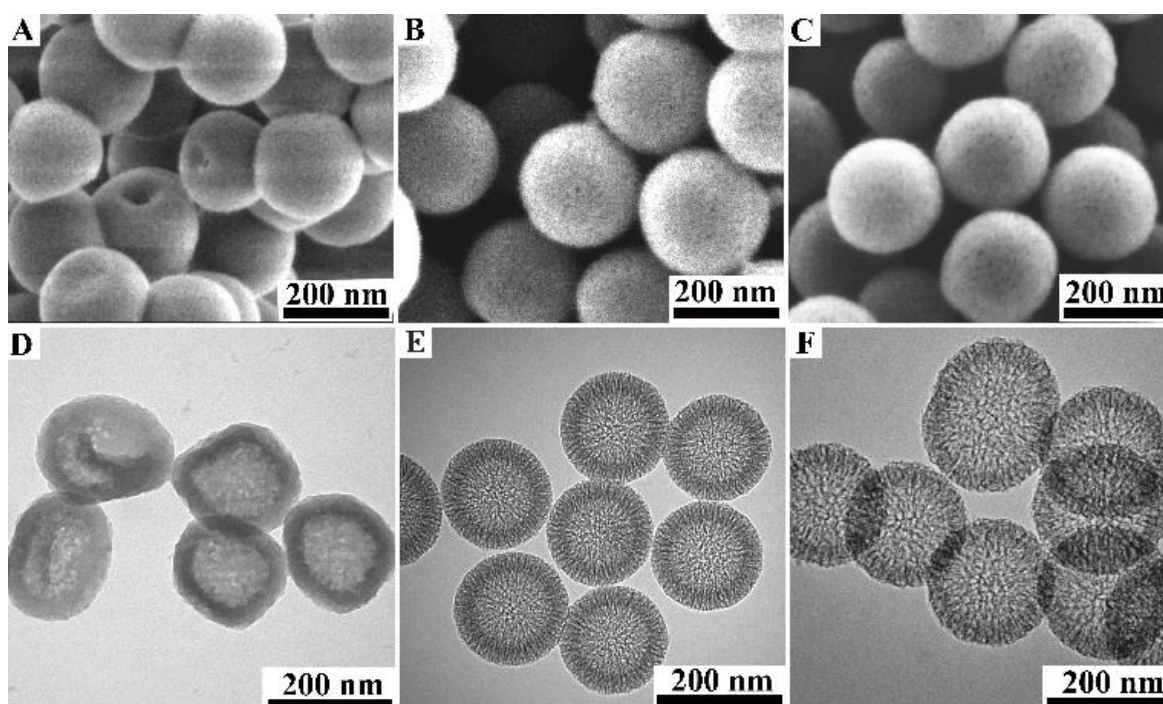
Fig 4.1 SEM (A, B, C) and TEM (D, E, F) images of MCHS-500, MCHS-700 and MCHS-900, respectively.

To understand the influence of carbonisation temperature on the composition and structure of MCHS-T samples, XPS and EA analyses were conducted, and the results are summarised in Table 4.1. MCHS-500 has the highest oxygen content of ~ 9.47% followed by MCHS-700 (5.09%) and MCHS-900 (4.48%). This trend is the same for

the H content in MCHS-T samples. For the carbon content, MCHS-500 shows the lowest value of 76.44% while MCHS-700 and MCHS-900 have a similar carbon content of 84 %. The above results indicate that the carbon content in MCHS-T samples increases with the carbonisation temperature, especially in the relatively low-temperature range (500-700 °C). The increase in carbon content is accompanied by a decrease in the O and H contents when the carbonisation temperature increases. It is noted that the oxygen content was measured by XPS, which generally reflects the surface composition difference. FTIR analysis also aligned with The XPS, and EA data obtained. FTIR analysis showed an absence of hydroxyl groups in MCHS-700 and MCHS-900 which can be attributed to the low O and H content (as provided in supporting information; Fig 4.S.2). Even MCHS-900 has a similar C content to MCHS-700 (measured from EA), the relatively lower O content leads to higher hydrophobicity as measured by the Rose Bengal adsorption test (Fig 4.S1).

Fig 4.2. Raman spectra (A) and DLS profiles of MCHS-T (B) in PBS and (C) in DMEM culture media.

Raman analysis was conducted to investigate the influence of carbonisation temperature on the atomic structures of MCHS-T samples. As shown in Fig 4.2A, the Raman spectra of three samples exhibit bo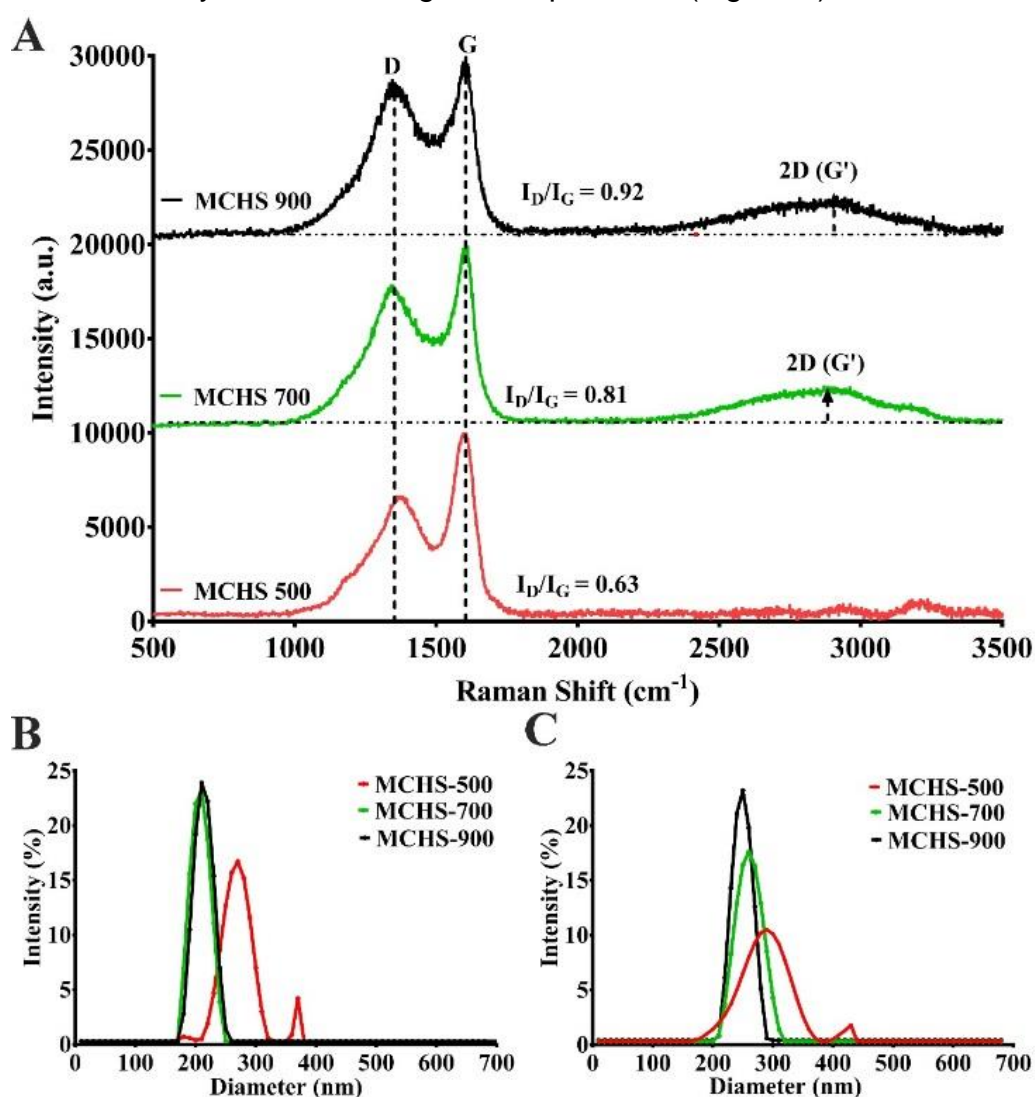th the "G band" (graphitic band) centred at 1580 cm^{-1} "D bands" (disordered band) centred at 1357 cm^{-1}.[112, 113] The ratio between the intensities of the D band and G band, i.e. I_D/I_G, is an important measurement of sp^3/sp^2 bonded carbon atoms.[114] With the increase in carbonisation temperature (500, 700, 900 °C), the I_D/I_G values increase (0.63, 0.81, 0.92). This observation is a common phenomenon in phenolic resins,[35, 115,86] indicating the ratio of disordered carbon atoms increases at elevated temperature. Moreover, MCHS-700 and MCHS-900 display 2D (G') peaks characteristic of multilayer graphene,[86] which is absent in MCHS-500, suggesting that graphitization starts at carbonisation temperature higher than 700 °C.

The dispersion of MCHS-T samples in phosphate buffer solution (PBS, pH 7.0) and DMEM media was analysed using DLS analytical technique. The DLS profiles of MCHS-700 and MCHS-900 show a narrow size distribution centred at 210 nm with a low polydispersity index (PDI) of 0.1 in PBS (Fig 4.2B). MCHS-500 shows a broad size distribution at 290 nm with a PDI of 0.4, indicating an aggregated structure. The dispersion of MCHS-T under aquatic conditions is influenced by its composition.[116-118] The aggregation of MCHS-500 is attributed to its higher oxygen content than MCHS-700 and MCHS-900. For MCHS-700 and MCHS-900 with a higher degree of carbonisation and increased hydrophobicity, their dispersity in PBS is significantly improved. However, at an even higher carbonisation temperature such as 1100 °C (MCHS-1100 in Fig 4.S3A), surface oxygen content decreases further to 3.32%. The sample MCHS-1100 forms visible aggregates due to high hydrophobicity (Fig 4.S4), suggesting low colloidal stability of MCHS-1100.

The colloidal stability of MCHS-T was also measured in DMEM (a cell culture medium) using DLS. As shown in Fig 4.2C, MCHS-900 is well dispersed in DMEM with a uniform size of 210 nm and a low PDI value of 0.13. For MCHS-700, the size increases from 210 nm in PBS to 260 nm and the PDI changes from 0.1 in PBS to 0.4. MCHS-500 has a broad size distribution centred at 290 nm and a high PDI of 0.93, indicating highly aggregated particles. This phenomenon has been observed in the previous studies,[28] in which the biomolecules in a cell culture medium may be absorbed on the carbon spheres. Our studies have shown that MCHS-900 has excellent colloidal stability in PBS and DMEM, which is crucial for cellular delivery applications.

Nitrogen adsorption isotherms of MCHS-T samples are shown in Fig 4.3A. MCHS-700 and MCHS-900 exhibit a type IV isotherm with two capillary condensation steps occurring at $P/P_0 = 0.6$-0.7 and $P/P_0 > 0.9$, characteristic of mesopores and large cavity, respectively. Compared to MCHS-700 and MCHS-900, MCHS-500 exhibits limited porosity and a large hysteresis loop indicating small pore entrance. The pore size distribution curves calculated from the adsorption branch using Barrett−Joyner−Halenda (BJH) model are shown in Fig 4.3B. The pore size of MCHS-500, MCHS-700 and MCHS-900 is 3.8, 6.0 and 6.9 nm, respectively. The Brunauer−Emmett−Teller (BET) surface area and pore volume of MCHS-T are summarised in Table 1. Compared to MCHS-900, MCHS-700 has a slightly higher surface area (1,705 vs 1,550 m^2 g^{-1}) and pore volume (2.8 vs 2.6 cm^3 g^{-1}) due to the slight framework shrinkage at a higher temperature.[115] MCHS-500 has the smallest surface area (494 m^2 g^{-1}) and pore volume (0.7 cm^3 g^{-1}). Our results have shown that the carbonisation temperature has a significant impact on the pore structures of MCHS-T samples. It is suggested that at a low carbonization temperature of 500 °C, the polymer network is not rigid and may deform during the silica etching process. Thus, the created mesopores are partially collapsed, leading to the low surface area and pore volume[119]. MCHS-1100 shows a similar porosity with MCHS-900 (Fig 4.S3B).
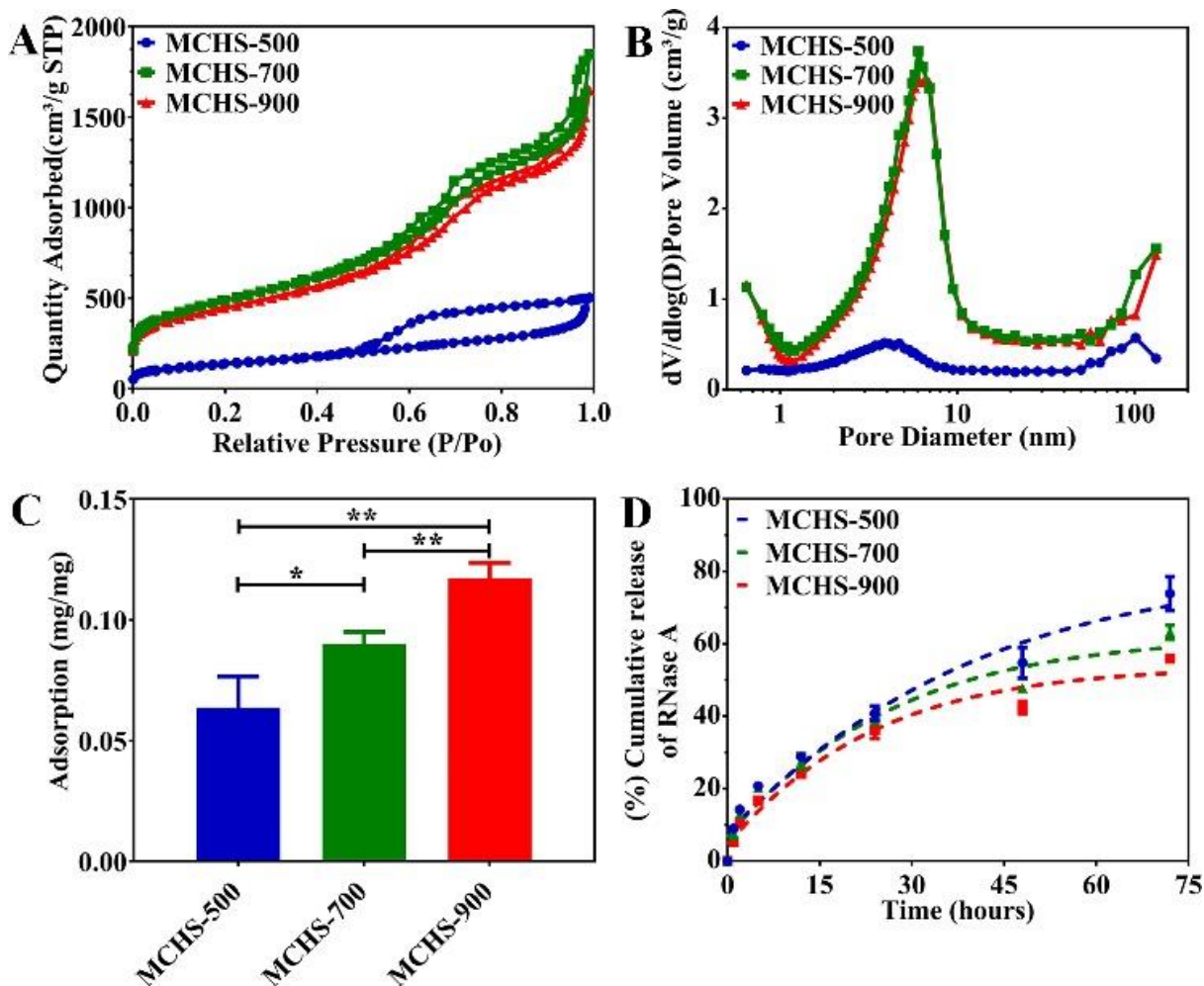
Fig. 4.3. (A) N$_2$ adsorption-desorption isotherms, (B) pore size distribution curves, (C) loading capacity of RNase A and (D) RNase A release profiles of MCHS-*T*.

Table 4.1. Summary of the physicochemical properties of MCHS-T

Sample	S (m^2 g^{-1})	P (nm)	V (cm^3 g^{-1})	C%	H%	O%
MCHS-500	494	3.8	0.7	76.44	3.62	9.47
MCHS-700	1705	6.0	2.8	84.17	1.92	5.09
MCHS-900	1550	6.9	2.6	84.02	1.42	4.48

Note: S is BET surface area, P is pore size, V is total pore volume, C% is carbon percentage, H% is hydrogen percentage, and O% is oxygen percentage.

Ribonuclease A (RNase A) with a size of 2.2 × 2.8 × 3.8 nm and a hydrophobic domain,[120] was reported as a potent therapeutic protein for cancer treatment by degrading cellular RNA and inhibiting protein production in the cytosol. RNase A was

51

chosen as a model protein to evaluate the delivery performance of MCHS-T. RNase A loading and release profiles were measured for MCHS-T before therapeutic evaluation. As shown in Fig 4.3C, MCHS-900 has the highest loading capacity among three MCHS-T samples. Moreover, MCHS-900 shows the slowest release, with ~ 40% of RNase A released in a period of 48 h (Fig 4.3D).

The high loading capacity and sustained release of MCHS-900 compared to two other samples are attributed to its high hydrophobicity as well as the large surface area and porosity. Based on our calculation (Table 4.S1 and Additional Discussion in supporting information), it is deduced that RNase A molecules loaded in MCHS-700 and MCHS-900 are mainly located on the mesoporous walls rather than the inner hollow cores. MCHS-1100 treated at even higher carbonization temperature demonstrates significantly decreased RNase A loading capacity (Fig 4.S5a) and slightly more sustained release (Fig 4.S5b) comparing to MHCS-900. High hydrophobicity induced aggregates of MCHS-1100 may hinder RNase A diffusion into the carbon samples in aqueous solutions. Furthermore, the large aggregates also significantly reduce cellular uptake of MCHS-1100 comparing to MCHS-900 (Fig 4. S5 c, d). It has been reported that efficient cellular uptake and high loading are crucial for therapeutic protein efficacy.[121] Thus, MCHS-1100 is not included in the following studies.

The cytotoxicity tests of MCHS-T and RNase A loaded MCHS-T were conducted in a cancer cell line (SCC25). For pure carriers as a negative control, there is little toxicity after the first 24 h of incubation at a high dose of 200μg mL^{-1} (Fig 4.S6). However, after further incubation for 48 h, MCHS-500 shows a higher level of toxicity with cell viability of ~ 70% due to its high organic content, which causes cellular irritation. MCHS-700 and MCHS-900 mostly comprised of inert carbon are biocompatible, but after 48 h MCHS-700 shows slight toxicity (~ 85% cell viability), whereas MCHS-900 retains its inertness. These results suggest that MCHS-900 is the most biocompatible carriers among the three tested samples.
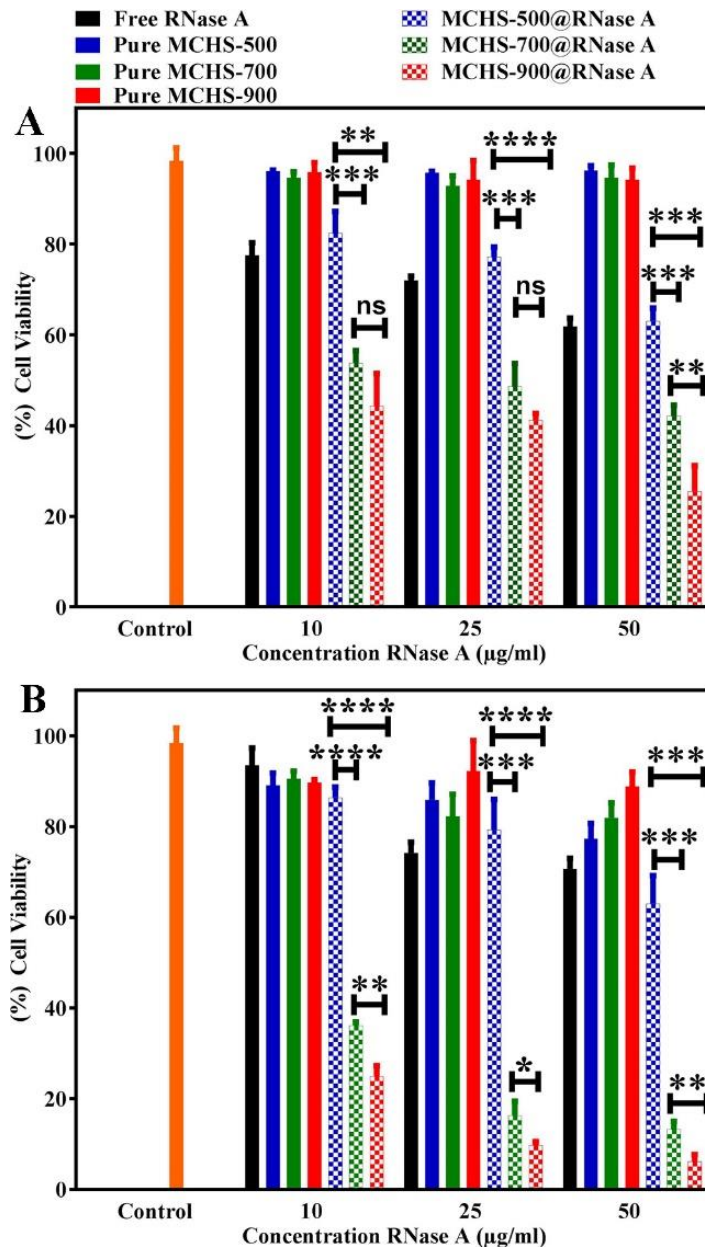
Fig. 4.4 Dosage-dependent cell viability of SCC25 cells treated with bare and RNase A after (A) 24 and (B) 48 h incubation. ns p> 0.05, *p<0.05, **p<0.01, ***p<0.001.

SCC25 cells were exposed to various concentrations of RNase A@MCHS-T where the final concentration of RNase A was 10, 25 and 50 µg mL^{-1}. Untreated cells were used as a blank control while both bare particles and naked RNase A were included a control with the same concentrations. Figs. 4A and B represent the dose-dependent cytotoxicity at 24 and 48 h incubation, respectively. In the first 24 h, ~74.4% of cells are inhibited by MCHS-900@RNase A at the highest dosage of 50 µg mL^{-1}, significantly better than MCHS-700@RNase A (57.8% inhibition), MCHS-500@RNase A (37% inhibition) and naked RNase A (38.2% inhibition) at the same dosage. After incubation for 48 h, the inhibition ratio is up to 93.9%, 86.7%, 36.9% and 29.4 % for MCHS-900@RNase A, MCHS-700@RNase A, MCHS-500@RNase A and free

RNase A groups at 50 µg mL^{-1}, respectively. In this prolonged incubation period, the anticancer efficiency of RNase A delivered by MCHS-900 and MCHS-700 significantly improved; however; in the case of MCHS-500, the therapeutic effect remains similar. The cytotoxicity tests demonstrate that the carbonisation temperature has a significant influence on the cellular delivery efficacy of RNase A for cancer cell treatment.
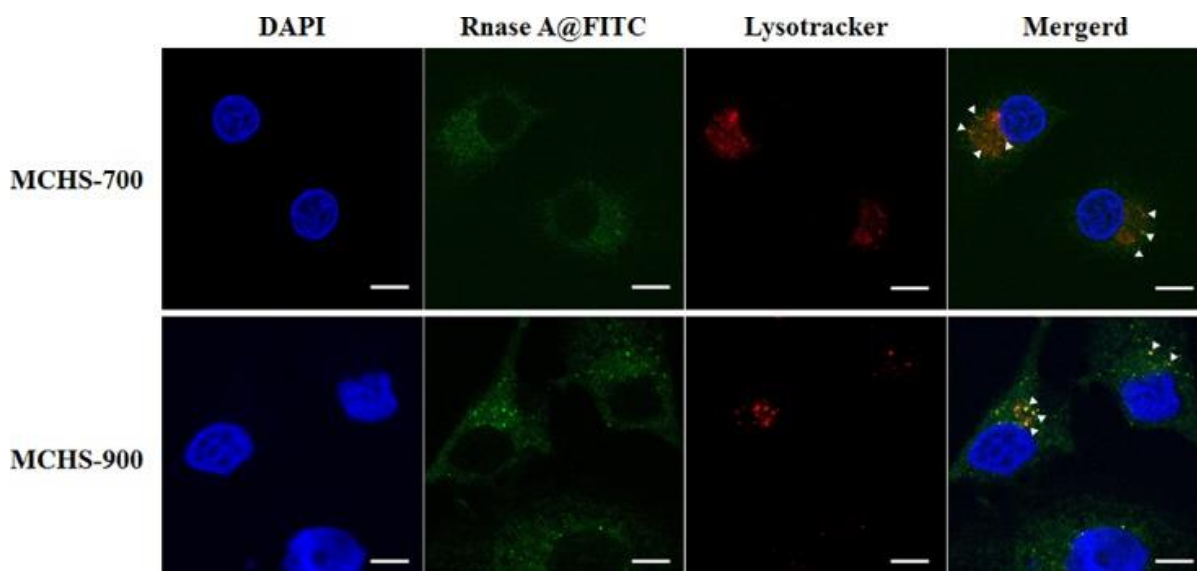
Fig. 4.5 Confocal microscopy images of SCC25 treated with RNase A delivered with MCHS-700 and MCHS-900. Blue fluorescent signal indicates the nuclei stained with DAPI; green represents FITC tagged with RNase A and red represents the endo/lysosome stained by lysotracker. Scale bar is 10 µm.

Efficient cellular uptake and endo/lysosome escape ability are essential for successful intracellular delivery of therapeutic proteins to achieve their functions inside cells.[108] To further understand why MCHS-900 has the best cellular delivery efficacy, the cells incubated with the MCHS-T samples loaded with RNase A tagged with FITC (RNase A@FITC) were monitored using the confocal microscope. The subcellular compartments of endo/lysosomes were traced using Lysotracker Red. As shown in Fig. 5, the green fluorescence intensity in SCC25 cells is much stronger in the MCHS-900 group compared to MCHS-700, indicating promoted intracellular delivery of RNase A. However, MCHS-500 has undetectable green fluorescence (Fig. S6). For MCHS-700, a significantly higher number of RNase A co-localized with endosomes (indicated by yellow fluorescence with triangle symbols) was observed compared to MCHS-900, suggesting that MCHS-900 is more efficient in endo/lysosome escape, contributed by improved hydrophobility.[122] Hydrophobic nanoparticles have been

reported to improve cellular uptake and facilitate cytosol delivery of therapeutic proteins with significantly enhanced cancer treatment efficacy.[122] These results indicate that MCHS-900 having the highest hydrophobicity demonstrate the best cellular uptake and most successful cytosol delivery of RNase A.

4.3. Conclusions

In summary, MCHS-*T* samples were synthesised under carbonisation temperature at 500°C (MCHS-500), 700°C (MCHS-700) and 900°C (MCHS-900) to evaluate their intracellular delivery performance of therapeutic proteins. MCHS-900 showed the highest hydrophobicity among all samples, exhibiting superior RNase A (a model of therapeutic proteins) adsorption and sustained release, beneficial for therapeutic protein delivery. RNase A delivered by MCHS-900 demonstrated significantly improved anti-cancer efficacy than free RNase A or delivered by MHCS-500 and MHCS 700. Furthermore, MCHS-900 also enhanced the cellular uptake of RNase A and successful endosomal escape, critical steps for therapeutic protein delivery. These findings in this work provide the rational design of efficient carriers with enhanced therapeutic protein delivery performance.

4.4. Supporting Information

4. S.1. Synthesis of MCHS-*T*

Mesoporous carbon hollow spheres (MCHS) were synthesised according to our previously reported method.[75] Specifically, 12 mM of tetrapropyl orthosilicate (TPOS) was added into an alcoholic solvent system consisting of 70 mL of absolute ethanol and 10 mL of deionized water with 3 mL of ammonium hydroxide (28 wt %) as a catalyst. Then, the above mixture was stirred for 15 minutes at room temperature, followed by simultaneous addition of 0.4 g of resorcinol and 0.56 mL of formalin (37 wt. %). The reaction solution was continuously stirred for 24 hours. The resultant slurry was collected and subjected to high-speed centrifugation at 20,000 rpm for 15 minutes. The solid samples were collected after washing with ethanol for three times and then dried overnight at 50 °C overnight. The hybrid RF polymer/silica samples were carbonised at different temperatures (500, 700, 900 or 1100 °C) for 5 hours under a nitrogen environment. The samples were then treated with 10 % hydrogen fluoride (HF, 50 %) solution for at least 24 hours to remove silica templates and washed thoroughly with deionized water three times. Finally, the carbon samples were obtained after drying at 50 °C overnight and denoted MCHS-*T* (*T*= 500, 700, 900, 1100), where *T* represents the carbonisation temperature in a nitrogen environment.

4. S.2. Fourier transform infrared spectroscopy (Fig 4.S) Spectral analysis of MCHS
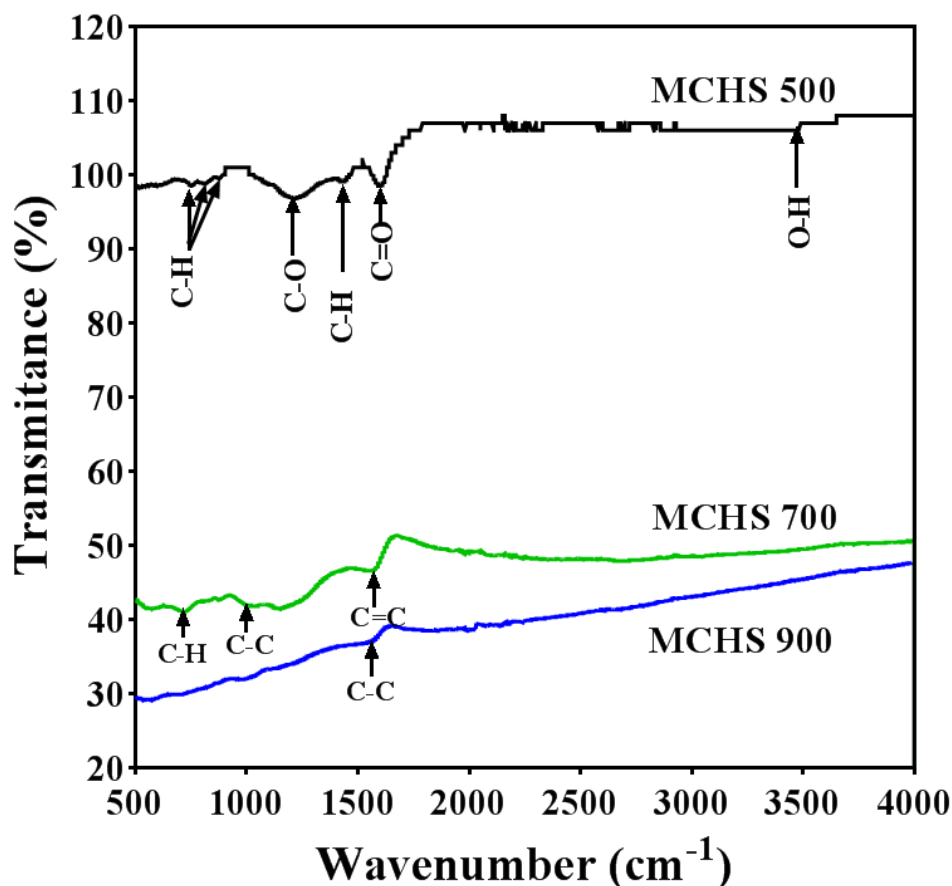
Fig 4.S1. FTIR spectral analysis of MCHS-*T* carbonised at different temperatures indicated as MCHS-500, MCHS-700, and MCHS-900.

 FTIR spectra of mesoporous carbon nanocarriers (MCHS) were conducted to identify the conformational differences in the samples carbonised at three different temperatures, presented in Fig. 4.S1. In the recorded spectra, a band around 3500-3400 cm^{-1} range were observed indicative of O-H stretching vibrations in MCHS-500, which were absent in MCHS-700 and MCHS-900. This showed that MCHS carbonised at lower temperature had hydroxyl groups present in the nanoparticles structures that got removed when carbonised at a higher temperature>700°C and above. Moreover, MCHS-500 showed sharp band around 1597 cm^{-1}. One of the possibilities could be indicative of the presence of N-H amine bonds, conceivably due to the addition of ammonium hydroxide in the system to maintain a basic condition for the TPOS hydrolysis, which is not observed in MCHS-700 as well as MCHS- 900. However, no N-H stretching band for ammonium at 3100 cm^{-1} can be observed. Therefore, we

believe this band can be assigned to C=O bonds from residual and not fully carbonised resorcinol, which diminished at a higher temperature. A medium, broad peak around 1200 cm^{-1} suggested the presence of C-O bond in MCHS-500, while in case of MCHS-700, the peak intensity was significantly diminished while being completely absent in MCHS-900. It is interesting to notice subtle peaks around 1100 cm^{-1} and 1047 cm^{-1} in MCHS-700 suggesting a shift of band to lower wavenumber which indicates the conversion of C-O bonds into C-C bonds [123]. A band peak around 1550 cm^{-1} in MCHS-700 indicated C=C bond stretching usually connected to the vibration of aromatic structures [124]. As the carbonization temperature increased to 900 °C in MCHS-900, the intensity of the peak for C=C decreased, indicating less polar functional groups. Apart from this intriguing trend, additional trend was observed from the spectra; three consecutive signalling peaks around 877 cm^{-1}, 809 cm^{-1} and 752 cm^{-1} representatives of a sequence of C-H bonds in MCHS-500 were almost reduced to minimal in MCHS-700 whereas almost non-existent in MCHS-900, thus, suggesting absence of any significant hydrogen bonds in the samples carbonized at higher temperatures. These observations support the theory of polarised hydrophobicity for samples carbonised at higher temperatures and as the temperature of carbonisation decreases, so does the hydrophobicity, as bonds with oxygen (O) persists at lower temperature modules. Clearly, from the FTIR peaks, it could be suggested, with increasing carbonisation temperatures, there was a significant decrease in functional groups indicating increased hydrophobicity, also supported by further Elemental Analysis (EA).

4.S.3. Flow cytometry analysis to evaluate cellular uptake of MCHS-900 and MCHS-1100

The cellular uptake of MCHS-900 and MCHS-1100 was estimated using flow cytometry analysis. Before the cellular study, 5μg of Rhodamine B Isothiocyanate (RBITC) was completely absorbed in 1 mg of MCHS-900 and MCHS-1100 in 1.5 ml of PBS, washed and resuspended in sterile PBS solution. SCC25 cells were seeded in a 24-well plate with a density of 5×10^4/well and incubated for 24 hours. Afterwards, 25 μg of RBITC@MCHS-900 or RBITC@MCHS-1100 were added in serum-free DMEM-F12 media. The cells were incubated for 4 hours, and the media was then removed, and the cells were washed with PBS twice. Then the cells were harvested by treating the cells with trypsin, followed by washing with PBS. The cells were suspended in 4 % paraformaldehyde solution for 30 minutes at room temperature, washed again and then resuspended FACS buffer (0.5 % BSA with 5 mM of EDTA in PBS).

4. S.4. Hydrophobicity Test (Rose Bengal Partitioning test)

The hydrophobicity of MCHS-T samples was evaluated using a xanthene dye "Rose Bengal" which preferentially gets adsorbed based on the hydrophobicity of the nanoparticles. It is a very reliable method, mainly applied in pharmaceutical studies to determine the surface hydrophobicity of nanoparticle drug delivery systems[125]. At first, in 0.1 M phosphate buffer solution (PBS) with a pH of 7.4, Rose Bengal (RB) reagent was dispersed making an aqueous RB stock solution. The stock solution was diluted to obtain a final concentration of 20 µg/mL. Then the dye solutions were added to various concentrations of nanoparticles (MCHS-T), followed by incubation at 25°C for 3 hours. Afterwards, the suspensions were centrifuged at 13,300 rpm for 10 minutes. The supernatants were collected, and absorbance was measured using UV-Vis spectroscopy at 549 nm. Evaluation of hydrophobicity by adsorption of RB was done by determining the PQ (partition quotient). PQ was plotted against the various concentrations of MCHS-T to indicate the ratio of an amount of RB [bound] to the MCHS-T Vs the RB [free] in the solution, where,

$$RB\ [bound]\ =\ [RB]\ total\ concentration\ -\ RB\ [free]$$

Moreover, PQ is calculated as:

$$PQ\ =\ RB\ [bound]/\ RB\ [free]$$

The degree of RB entrapment is expressed through the loading capacity and loading efficiency values. Loading capacity (LC) takes the amount of RB entrapped in the particles as a function of the weight of particles. Loading efficiency (LE) is calculated by comparing the amount of RB included in the particles with the total sum of RB. The following equations determined loading capacity (LC) and loading efficiency (LE):

$$LC\ (\%) = Bound\ [RB]/weight\ of\ particles \times 100$$

$$LE\ (\%) = bound\ [RB]/total[RB] \times 100$$

Three batches of particles were prepared in each system, and the results are given as average and standard deviations[126].
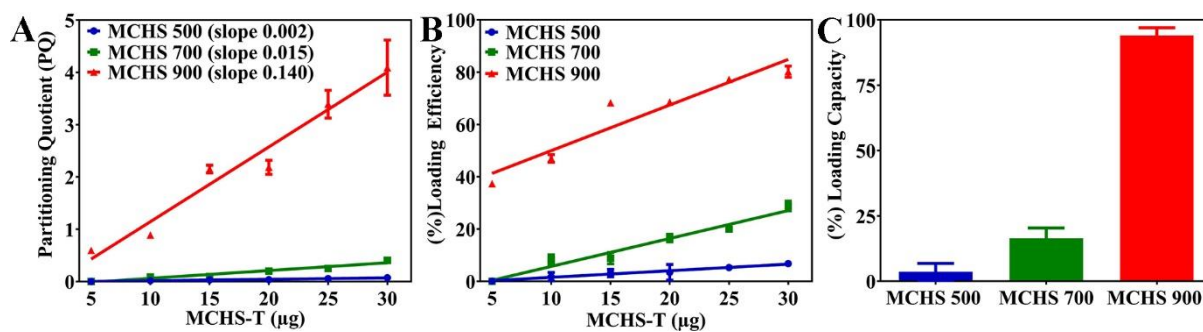
Fig 4.S2. Relative hydrophobicity as measured by adsorption of Rose Bengal on MCHS-*T*. (A) PQ and (B) LE values as a function of the weight of MCHS-*T* and (C) LC of 10 µg of MCHS-*T* towards RB.

PQ values are shown in Fig 4.S2A showed a higher inclined slope in MCHS-900 (0.140) than MCHS-700 (0.015) and MCHS-500 (0.002), suggestion more adsorption of RB per unit weight. LE values varied from 37 % to 80 % for MCHS-900 when the weight of MCHS-900 increased from 5 to 30 μg (Fig 4.S2 B). In contrast, the LE value for MCHS-700 ranged from 0% to 30 % while that value for MCHS-500 could only reach maximum 6.9 % of LE given the highest amount of nanoparticles. The evaluation of LC was calculated based on 10µg of MCHS-*T* in aqueous RB solution. MCHS-500 had the lowest capacity, 3.6 % followed by MCHS-700 with a value of 16.5%. MCHS-900 was proved to have a much higher LC value (94 %) than the other two samples as shown in Fig 4.S2 C. These results consistently indicate that MCHS-900 have the highest hydrophobicity. Higher carbonisation temperature leads to higher hydrophobicity.

Fig 4.S3. (A) TEM image and (B) nitrogen absorption-desorption isotherm and pore size distribution curve (inset) of MCHS-1100.

TEM image of MCHS-1100 (Fig 4.S3A) reveals a similar intact hollow spherical morphology with the mesoporous wall as observed in MCHS-900. The adsorption-desorption plot (Fig 4.S3B) is typical type IV isotherm with one capillary condensation

step at P/P_0=0.6-0.7, indicating mesoporous structure. The corresponding pore size distribution curve (inset of Fig 4.S3B) shows a pore size centred at 6.84 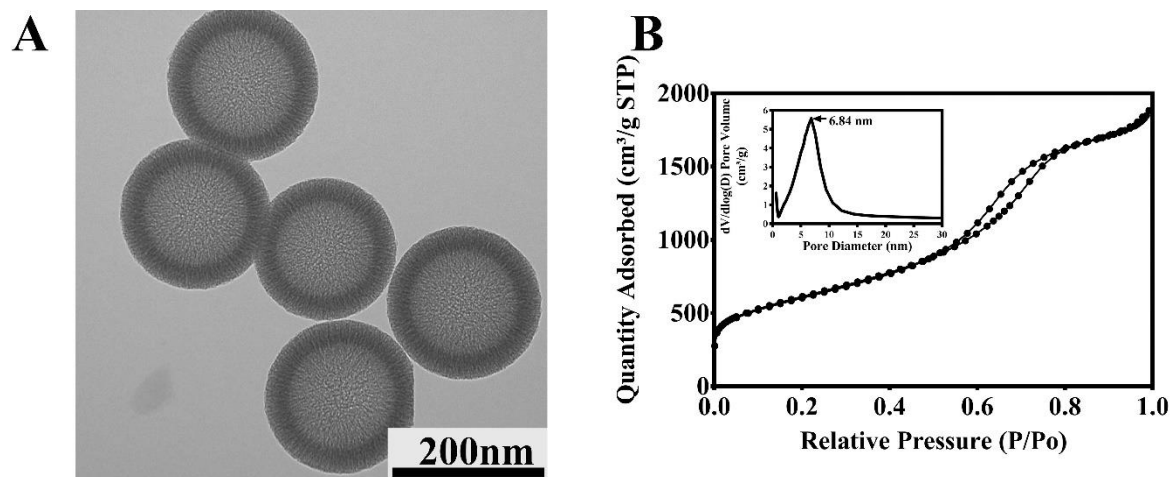nm, which is similar to MCHS-900. BET surface area and pore volume of MCHS-1100 is 2145.5 m^2/g and 2.9 $cm^3 g^{-1}$, respectively.
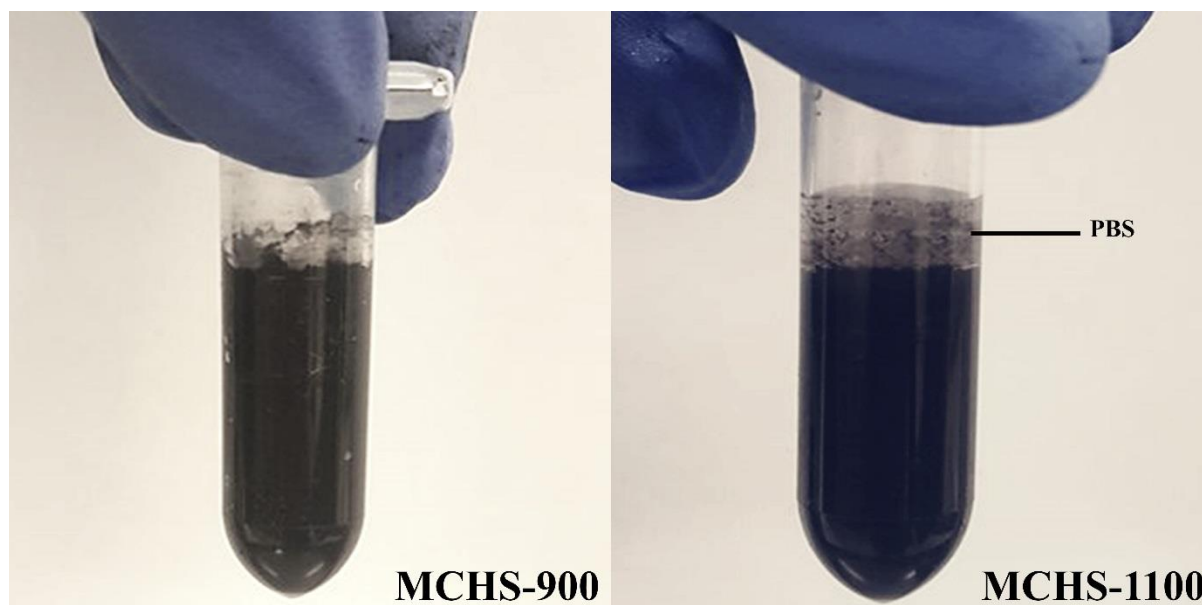
Fig 4.S4. Images are showing the dispersion of MCHS-900 and MCHS-1100 after ultra-sonication. We observed that MCHS-900 had excellent dispersity in PBS buffer solution whereas MCHS-1100 started to separate from the buffer solution and settle as aggregates in PBS after 5 minutes of ultra-sonication.

4. S.5. Additional Discussion: Possible locations of RNase A molecules in MCHS samples

To predict the possible locations of RNase A adsorbed on MCHS samples, RNase A adsorption capacity per unit surface area (mg/m^2) is calculated (as shown in Table 4.S1), dividing loading capacity by BET surface area excluding the unusable micropore area for RNase A adsorption. MCHS-500 has limited porosity. Thus RNase A molecules are mainly adsorbed on the external surface, showing a loading capacity of 0.14 mg/m^2. For MCHS-700 and MCHS-900, the pore size is 6-6.9 nm, which is smaller than double size of 3.8 nm (the largest dimension of single RNase A molecule). Therefore, it is unlikely that the single mesoporous channel on the shell could accommodate two RNase A molecules. In this case, the mesoporous area of MCHS-700 and MCHS-900 is partially used for RNase A adsorption (around 50% or less), thus showing relatively low loading capacity of 0.06 and 0.09 mg/m^2 for MCHS-700 and MCHS-900. If RNase A molecules are loaded inside the large hollow cavity of MCHS-700 and MCHS-900, these molecules should in a multi-layer adsorption model

and the calculated RNase A adsorption capacity per unit surface area would be significantly higher than 0.06 or 0.09 mg/m^2. Based on these results, we assume that RNase A molecules loaded in MCHS-700 and MCHS-900 are on the surface of carbon materials (mesoporous, external and internal wall) with a mono-layer adsorption model, rather than inside of hollow cores.
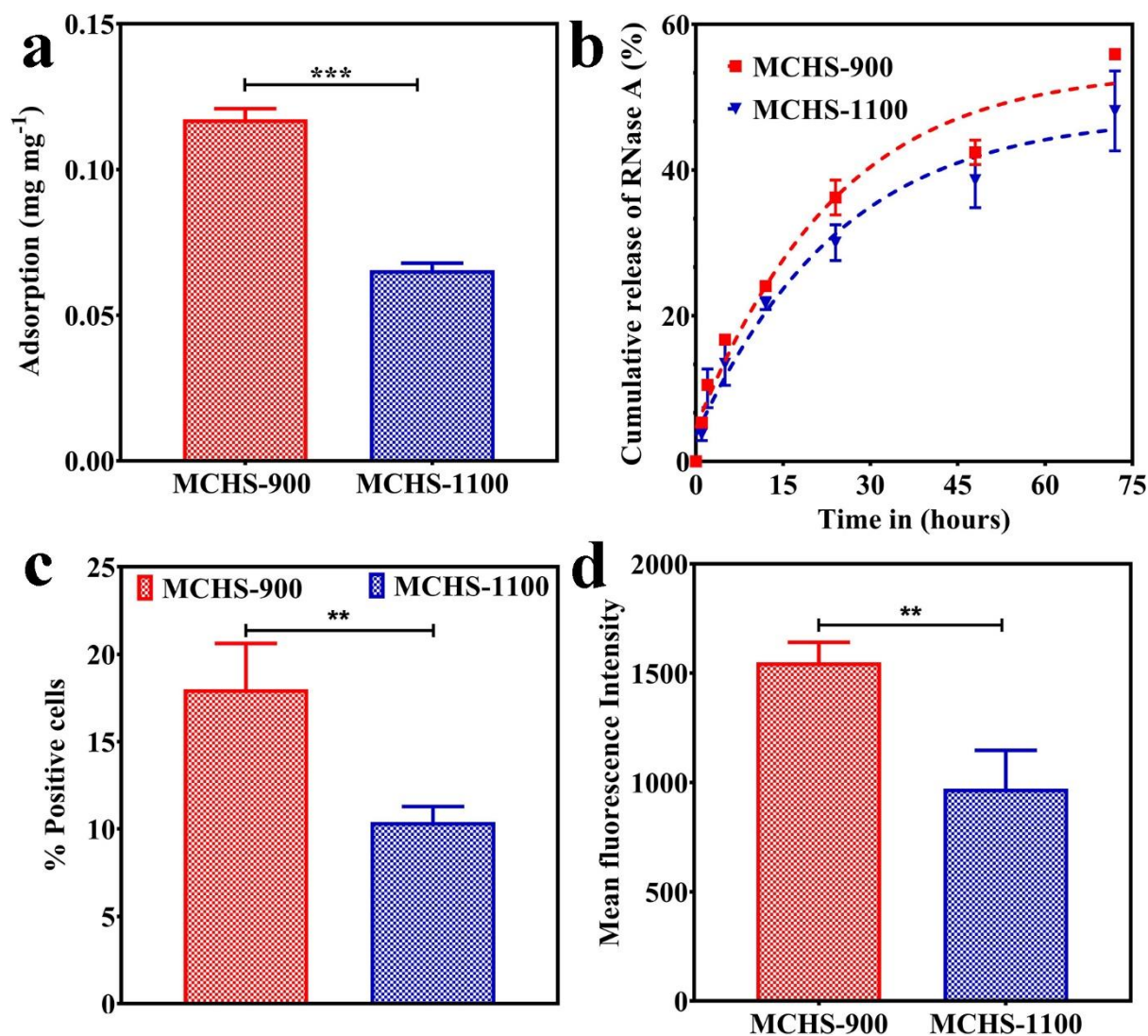
Fig 4.S5. (a) Loading capacity of RNase A, (b) RNase A release profile of MCHS-900 and MCHS-1100, (c) RBITC positive cell percentages and (d) mean fluorescence intensity of SCC25 cells treated with RBITC labelled MCHS-900 and MCHS-1100.

MCHS-1100 shows a much lower RNase A loading capacity than MCHS-900 (0.065 vs 0.117 mg/mg, Fig 4.S5a) and slightly more sustained release of RNase A (Fig 4.S5b). To quantify the cellular uptake performance of MCHS-900 and MCHS-1100, flow cytometry was performed in SCC25 cells treated with RIBTC loaded carbon samples. The cells treated with RBITC loaded MCHS-900 show significantly larger proportion of RBITC positive cells (18.0±2.6% vs 14.4±0.9%, Fig 4.S5c) and stronger

mean fluorescence intensity (1550±91 vs 971±176, Fig 4.S5d) than those treated with RBITC loaded MCHS-1100. These results suggest that the low colloidal stability caused by high hydrophobicity significantly impedes the cellular uptake of MCHS-1100, thereby not suitable for cellular delivery of RNase A.
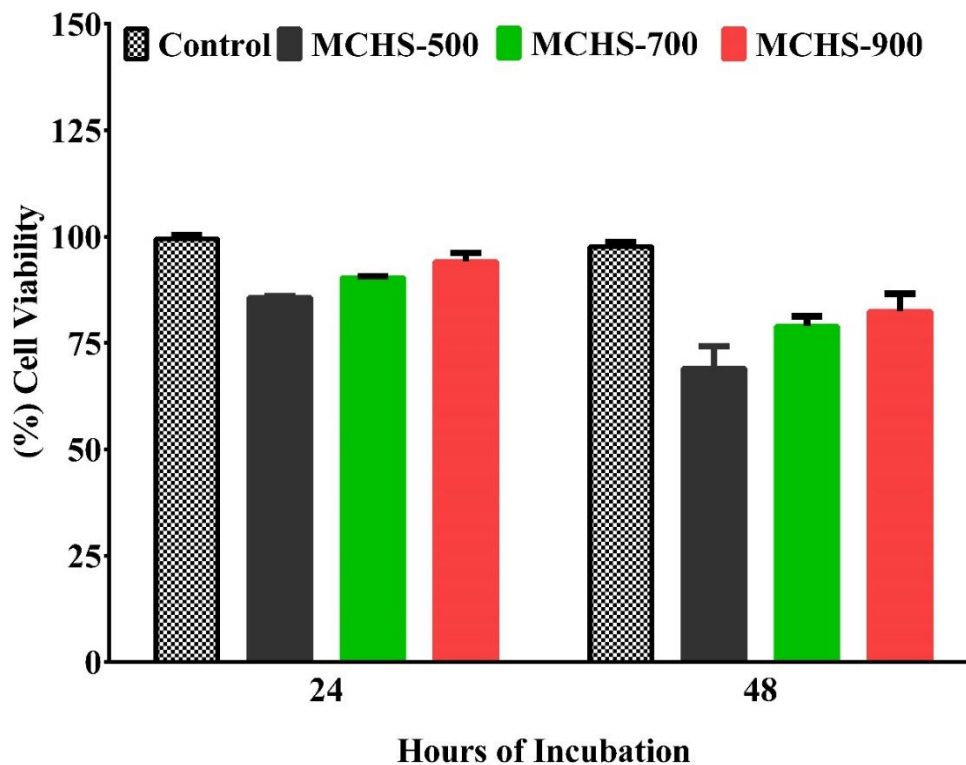
Fig 4.S6. Cell viability of SCC25 cells treated with bare MCHS-*T* at a high concentration of 200µg/mL to investigate the biocompatibility of the nanocarriers.
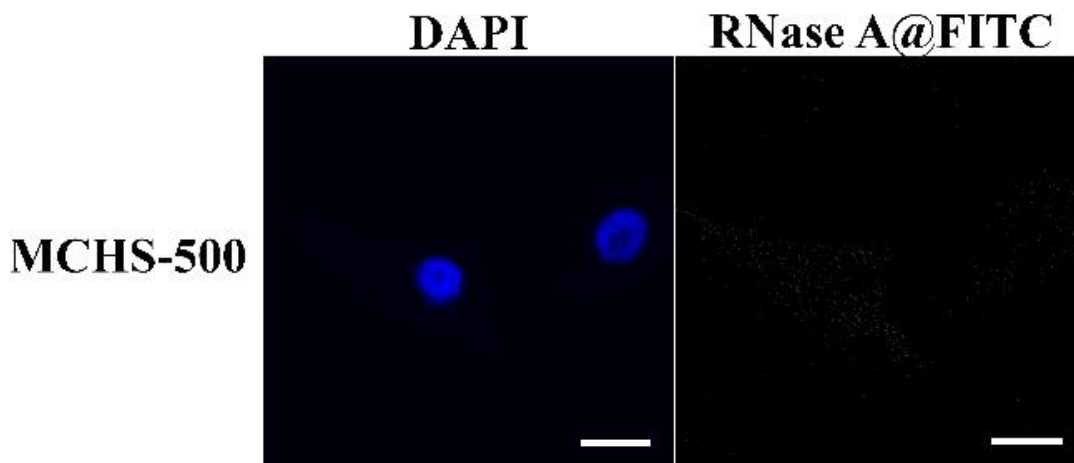
Fig 4.S7. Confocal Microscopic images of SCC25 showing the fluorescent signals of blue representing DAPI and green representing RNase A tagged with FITC carried inside the cells by MCHS-500, the scale bar is 10µm.

Table 4.S1. Calculated RNase A adsorption capacity of MCHS samples.

	MCHS-500	MCHS-700	MCHS-900
S_{BET} (m^2 g^{-1})	494	1705	1550
S_{Micro} (m^2 g^{-1})	40	231	217
$S_{BET-Micro}$ (m^2 g^{-1})	454	1474	1333
$C_{RNase\ A}$ (mg g^{-1})	63.6	89.9	117
$C'_{RNase\ A}$ (mg m^{-2})	0.14	0.06	0.09

S_{BET} (m^2 g^{-1}): BET surface area; S_{Micro} (m^2 g^{-1}): t-Plot micropore area; $S_{BET-Micro}$ (m^2 g^{-1}):BET surface area – t-Plot micropore area; $C_{RNase\ A}$ (mg g^{-1}) : RNase A adsorption capacity; $C'_{RNase\ A}$: RNase A adsorption capacity per m^2 ($C_{RNase\ A}$/$S_{BET-Micro}$).

Chapter 5

Antioxidant property of pristine mesoporous carbon hollow spheres (MCHS) for ROS-mediated cancer therapeutic strategy

This chapter reports the ability of MCHS to relieve intracellular oxidative stress, mainly prevalent in cancer cells, by its efficient free radical scavenging property.   Here we measured the antioxidant property of MCHS carbonised at varied temperatures to select the optimized MCHS for maximum scavenging activity. We also tested the free radical scavenging activity of MCHS compared to other popular carbon scavengers to compare its effectiveness.

5.1. Introduction

The key to developing novel and effective cancer therapeutics is to understand the behaviour of cancer cells and their specific alterations. Mounting evidence has suggested that compared to healthy cells, most of its cancer counterparts have particular biochemical modifications that allow them to have high levels of intracellular ROS aka. "Reactive Oxygen Species"[127, 128]. ROS, are defined as highly reactive free radicals that arise from cellular respiration as essential by-products originating from the mitochondrial electron transport chain (ETC), found in almost all cells and tissues. They help in various critical biological functions such as signal transduction for the regulation of protein and transcription factors, cellular growth, survival and differentiation, vascular regulation, oxygen sensing for initiating adaptive responses and immunological defence system[129]. However, due to the presence of several unpaired electrons, most of them are highly charged species, and a severe increase in their cellular level leads to "oxidative stress"; often result in irreversible oxidative damage causing cellular alterations, mutations and death[130, 131]. Our bodies natural defence response to high cellular ROS levels is to deploy special enzymes called "antioxidants" [such as, superoxide dismutase (SOD), catalase, glutathione peroxidase (GPx), glutathione (GSH),trace amounts of coenzyme Q, etc.], that represses the reactivity of ROS to lower levels and establish cellular redox homeostasis[132, 133]. Mounting amount of studies have found that most of the cancer cells exhibit increased aerobic glycolysis known as the Warburg effect, the discovery of which has given rise to new research interest towards the development of novel ROS- mediated therapeutic strategies[134, 135]. Cancer cells found in advanced tumours frequently show high oxidative state environments giving rise to a "vicious cycle". Generally, in the homeostatic state, ROS species activates wild-type p-53 protein in healthy cells that trigger stress responses and repairs the DNA from ROS-mediated damage. However, in cancer cells with defective p53, ROS mediated damaged DNA starts to accumulate which results in loss of function of p53. With ROS mediated DNA mutations and lack of deletions, the accumulation of damaged DNA propagates genomic instability, activation of oncogenes, metabolic dysfunction causing more DNA damage and contributing to cancer spread[127, 136]. Constant exposure to intrinsic oxidative stress may exert adaptive mechanisms to counteract the potential toxic effects of elevated ROS levels and to promote cancer cell survival. Thus,

Chemotherapeutics, especially, ROS generating agents alone are not sufficient to kill cancer cells. To maximise the ROS mediated therapeutic strategy; it is possible to apply antioxidant agents to have an additive or synergistic effect in cancer therapeutics.

Endogenous and dietary antioxidants such as Vitamin C and E have been extensively investigated for its anticancer and antitumor properties and has shown modest clinical significance1-3. However, these antioxidants are limited by its poor selectivity for radical eradication, limited stoichiometric capacity, and dependence on detoxifying molecules[14]. Recent preclinical studies have demonstrated carbon nanomaterials such as single-walled and multi-walled carbon nanotubes, graphene, fullerenes, carbon clusters, carbon dots, etc. exhibit superior antioxidant properties than those of dietary antioxidants and it's an affinity towards cellular uptake [14][12, 13]. Their antioxidant properties have shown impressive results in not only ROS generated diseases such as inflammation, arthritis; neuro-generative diseases, cancer etc.[133, 137-139]; but also showed promising performance in recovery and restoration in patients who suffered traumatic brain injury[12]. However, among the various carbon particles utilized for biomedical applications, mesoporous carbon nanomaterials hold a more significant promise as it has a carbonaceous composition with high porosity, biocompatibility, chemical inertness, cellular affinity, which are highly desirable traits for therapeutics strategies[2, 36]. Moreover, owing to its physicochemical properties, biocompatibility and its cellular affinity, it readily interacts with ROS species (hydroxyl radicals) in the cells and displays ROS scavenging activity, which has never been reported in any other carbon nanoparticles. Thus, the most intriguing property of MCHS lies in its antioxidant property in its pristine form, which can be enhanced by changing its carbonization temperature. This property has never been observed in any other contemporary carbon nanoparticles. Herein, for the first time, we report the antioxidant property of mesoporous carbon hollow spheres (MCHS) optimized by the carbonizing temperature that assists it to have a hydroxyl scavenging property along with high cellular affinity and high biocompatibility without the need to functionalize. We further tested its antioxidant property compared to other contemporary pristine carbon nanoparticles such as carbon nanotubes and reduced graphene oxide in cancer cell line HCT-116. Hence, using optimized MCHS alone may function as effective antioxidants and have sufficient capacity for radical eradication to be used therapeutically during periods of excessive ROS generation.
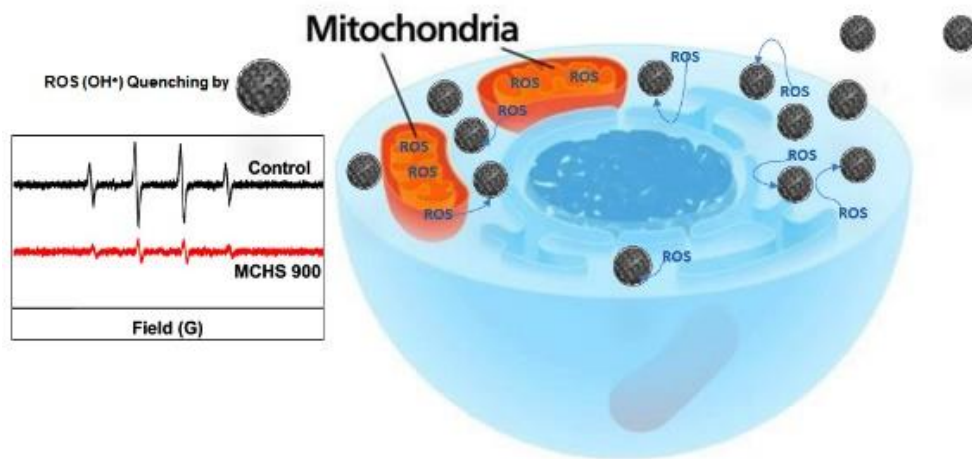
Fig 5.1 Schematic representation of antioxidant MCHS-900 having ROS scavenging property.

5.2. Materials Specifications:

MCHS-*T* were synthesised and carbonised according to the procedure described in Chapter 4. Carbon nanotubes (CNT), >98% were purchased from Sigma-Aldrich, product#719803-25G. Reduced Graphene oxide (RGO) was borrowed from the Centre for Personalised Nanomedicine laboratory, AIBN, UQ synthesised by Dr Xiaodan Huang using established protocol[140] which he fully characterised[141]. HCT-116 adherent cells were grown in DMEM media supplemented with 10 % Fetal Bovine Serum (FBS) and 1% Penicillin-streptomycin (PS). For subculturing purposes, the cells were washed with sterile PBS solutions and trypsin (0.25 g L^{-1}). The cells were attached to T75 flasks and incubated at 37 °C under 5% CO_2 sterile environment.

5.3. Experimental section

5.3.1. Hydroxyl free radical scavenging assay by EPR spectroscopy

The reactive oxygen species was monitored by electron plasma resonance (EPR, Elexsys E500 CW, Bruker) spectroscopy using the spin trapping technique. In this method the intensity was measured, resulting from the conversion of a trapping agent DMPO to DMPO-OH● adduct brought about the hydroxyl free radicals generated by Fenton reaction:

$$Fe^{2+} + H_2O_2 \longrightarrow OH● + OH + Fe^{3+}$$

Hydroxyl free radicals were generated by adding 10 mM of H_2O_2 into a PBS buffer solution, pH 7.4, containing 250 mM of 5, 5-dimethyl-1-pyrroline-N-Oxide (DMPO, trapping agent) and 1 mM of $FeSO_4$. 50 μL of the sample were measured and were

marked as positive control. Later, to test the scavenging property of the carbon nanoparticles. 100 µg of the particles were added to the mixed solution similar to positive control and incubated at room temperature for 20 min. 50 µL of the solution was then transferred into the capillary tube for EPR analysis of the remaining hydroxyl free radicals.

5.3.2. Intracellular ROS measurement using a fluorescent microplate technique

HCT 116 cells were seeded in 96 welled plates (Corning 96 Well, clear bottom, fluorescence-based Microplate) at a concentration of 3×10^4 cells and incubated for 24 hours at 37°C in 5 % CO_2 sterile environment. Then the media is removed and washed with 100µL of 1XPBS per well. Then a 10µM solution of tert-Butyl hydroperoxide (TBHP) was added to each well to emulate the oxidative stress environment in cells leaving control groups were incubated for an hour at 37°C in 5 % CO_2 sterile environment. Then the MCHS samples carbonised at different temperatures (700˚C -1300 ˚C) were added to each well at a concentration of 25µg/mL and incubated. Then the PBS is removed, and 25 µM of DCFH2-DA is added to each well. The cells were incubated for 45 minutes at 37°C in 5 % CO_2 under dark conditions. Then dye solutions were removed, and the cells were again washed with 1x PBS. Then 100 µL of the buffer solution is added to each well, and the plates were read in Tecan Plate Reader PRO 200, at an excitation wavelength at 485 nm and emission wavelength at 535 nm.

5.3.3. Detection of ROS scavenging activity using fluorescence imaging

HCT 116 cells were seeded in a 6-welled plate at a seeding concentration of 1.5×10^5 on the surface of sterilised coverslips in DMEM media supplemented with 10 % Fetal Bovine Serum (FBS) and 1% Penicillin-streptomycin (PS). The cells were incubated for 24 hours at 37°C in 5 % CO_2 sterile environment. 10 µM of TBHP (Tert-Butyl hydroperoxide, {TBHP), 70 % in H_2O, was added to each well, and the cells were incubated for an hour at 37°C generating an intracellular environment of extreme oxidative stress. One of the wells were left untreated with TBHP and were marked as the negative control. Then the carbon-scavenging agents were added to each well at a concentration of 25µg/mL leaving one of them as the positive control. The cells were incubated for 4 hours at 37°C in 5 % CO_2 sterile environment. After the incubation

period, the media was removed, and the cells were washed with sterile 1xPBS twice. After that 25µM solution of DCFH2-DA (2′, 7′-dichlorodihydrofluorescein diacetate) were added to cells to stain them. The cells were incubated for 45 minutes at 37°C in 5 % CO_2 under dark conditions. Then dye solution was removed, and the cells were again washed with 1x PBS twice. Then 500µL of 4% PFA (Paraformaldehyde) to each well and were incubated overnight at room temperature. Again, the cells were washed with 1xPBS, and then the cells were observed under a bright field microscope with an excitation wavelength at 485nm and emission wavelength at 535nm. The cellular uptake was also quantified by flow cytometry analysis (FACS) using BD Accuri™ C6 Plus.

5.3.4. Flow cytometry analysis to evaluate ROS scavenging activity

HCT-116 cells were grown on 12-welled plates at a seeding concentration of 0.5×10^6. After overnight incubation at 37°C in 5 % CO_2, the media was removed, and the cells were washed with sterile PBS. Then a 10µM solution of TBHP was prepared in a serum-free media and was added to each well to induce oxidative stress. The cells were incubated for an hour at 37°C in 5 % CO2, and the nanoparticles were added, and the cells were incubated for 12 hours. After that 25µM solution of DCFH2-DA (2′, 7′-dichlorodihydrofluorescein diacetate) were added to cells to stain them. The cells were incubated for 45 minutes at 37°C in 5 % CO_2 under dark conditions. Then DCFH2-DA solutions were removed, and the cells were again washed with 1x PBS twice. The cells were washed thrice and trypsinised using (0.25 %) Trypsin-EDTA and incubated for 3 minutes at 37°C in 5 % CO_2. The trypsinized samples were collected, centrifuged and washed with sterile PBS and resuspended in FACS Buffer (1 % BSA and EDTA solution made in Ca^{2+} and Mg^{2+} free Phosphate buffer). The samples were then analysed using "BD Accuri C6" flow cytometer. All the samples analysed were triplicated.

5.3.5. Cellular uptake study of carbon-scavenging agents

HCT116 cells were seeded in sterile glass coverslips placed in 6-welled plates at a density of 1.5×10^5 cells per well and cultured for 24 hours in DMEM media at 37 °C in 5 % CO_2 sterile environment. Simultaneously, Rhodamine B (RhB) was loaded in the 1 mg of carbon nanoparticles with an RhB feeding amount of 5µg/mL in PBS solution. The loading amount was measured by measuring the difference in UV-Vis absorbance of RhB in the solution before and after adding carbon-scavenging agents. Then the

RhB loaded carbon-scavenging agents were added to the wells at a concentration of 0.35 µg/mL of RhB, finalised from the loading amounts. Then the cells were incubated for 4 hours at 37 °C after which the media was removed, and the coverslips with attached cells were washed twice with PBS. After washing the cells, 500 µL of 4 % w/w paraformaldehyde solution was added to each well to fix the cells followed by incubation overnight at room temperature. Later, the coverslips were rewashed with PBS twice, and the coverslips were attached to the slides by adding DAPI stains and let it dry at room temperature. In the end, the cellular images were taken using a Zeiss LSM 710 META confocal microscope (Carl Zeiss, Thornwood, New York).

5.3.6. Flow cytometry analysis to evaluate cellular uptake

The cellular uptake of MCHS-900, CNT and RGO were estimated using flow cytometry analysis. Before the cellular study, 5µg of RhB was wholly absorbed in 1 mg of samples in 1.5 ml of PBS, washed and suspended in sterile PBS solution. HCT-116 cells were grown on 12-welled plates at a seeding concentration of 0.5×10^6. After overnight incubation at 37°C in 5 % CO_2, the media was removed, and the cells were washed with sterile PBS. Then 0.35 µg/mL of RhB loaded particles were added to each well. The cells were incubated for 4 hours at 37°C in 5 % CO_2. The cells were washed thrice and trypsinized using (0.25 %) Trypsin-EDTA and incubated for 3 minutes at 37°C in 5 % CO_2. The trypsinized samples were collected, centrifuged and washed with sterile PBS and resuspended in 500µL of FACS Buffer (1 % BSA and EDTA solution made in Ca^{2+} and Mg^{2+} free Phosphate buffer). The samples were then analysed using "BD Accuri C6" flow cytometer. All the samples analysed were triplicated.

5.4. Results and discussion:

Hydroxyl radical (OH•) is the most abundantly found ROS in the human body, and we did a preliminary EPR analysis to investigate the OH• radical eliminating property of pristine MCHS modified with carbonization temperature, Fig.5.2 (A). We found that at 900°C, MCHS's scavenging activity of hydroxyl ions was enhanced, however further elevation of carbonization temperature diminished its scavenging influences. The EPR profiles of MCHS carbonised at different temperatures (700°C -1300 °C) showed an interesting trend. At 700 °C, the percentage of hydroxyl radicals scavenged was close to ~65.00 %. As we carbonised MCHS at a higher temperature, the scavenging activity of MCHS was heightened, and the radical annihilation was close to ~74.00%. However, the trend didn't linger for long, further increase in carbonization temperature the scavenging activity of MCHS kept

reducing where MCHS carbonised at 1100 °C, and 1300 °C reduced approximately ~69.60 % and ~67.40 %, respectively. From EPR analysis, we could found that 900 °C is the optimized temperature of carbonization for MCHS that has the ability to bring out the best hydroxyl scavenging property in pristine form. Additionally, we conducted an EPR analysis of MCHS-900 compared to other carbon-scavenging agents in its pristine form as well, as shown in Fig. 5.3 (A). The EPR results revealed that in aqueous solutions RGO had a higher scavenging activity than CNT, where RGO reduced the OH$^\bullet$ levels to ~30.4 % and CNT brought the levels down to ~17.4 %. Summarizing all the EPR analysis data, we could conclude that pristine MCHS-900 carbonised at 900°C not only has an excellent scavenging ability than any other MCHS carbonised at other temperatures (700 °C -1300 °C) but also its still the best carbon scavenging agent in its pristine state than other popular carbon-based scavenging agents.
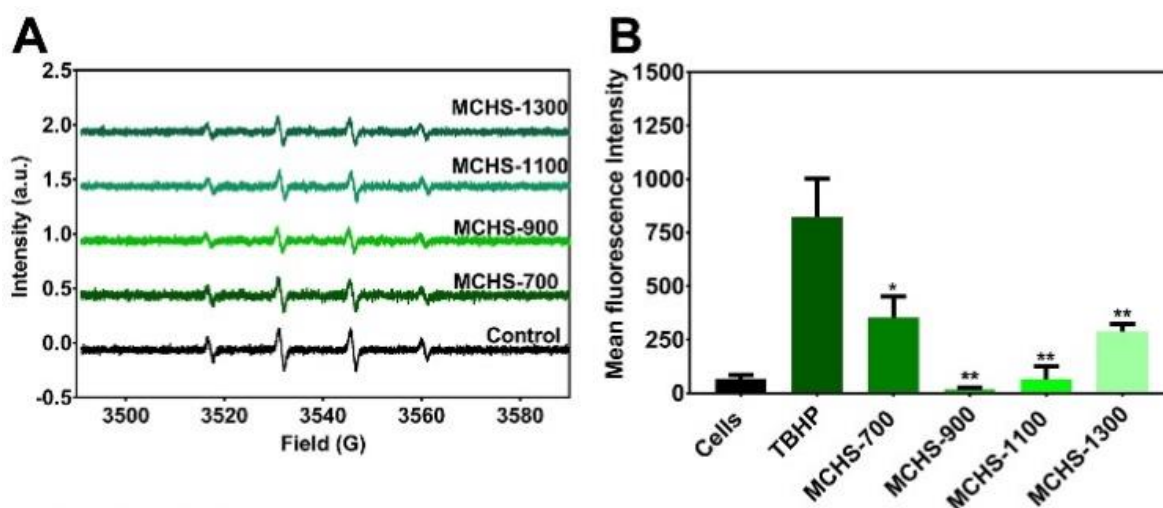
Fig 5.2 (A) Effect of MCHS carbonised at different temperatures on hydroxyl radicals generated by Fenton reaction. The number of radicals produced is proportional to the intensity of EPR signals(B) Intracellular ROS scavenged by MCHS carbonised at different temperatures in HCT-116 cells, ns, *$p<0.05$, **$p<0.01$, ***$p<0.001$.

We proceeded further to investigate the intracellular hydroxyl radical annihilation ability of pristine MCHS and weather the carbonization temperature influences its ability to scavenge ROS intracellularly as it does extracellularly. As shown in Fig. 5.2(B), the intracellular ROS scavenging activity changed as MCHS were modified at different carbonization temperature. We observed after cellular interaction of HCT-116 cells with MCHS-700, ~50.00 % of TBHP induced ROS were scavenged. As the temperature of carbonization was elevated, the amount of ROS scavenged was massively amplified by an average of 97.93 %. However, as the temperature of carbonization was increased further, the scavenging activity was affectedly

reversibly. MCHS-1100 showed a slight drop in the scavenging activity to an average of ~92.00 % whereas MCHS-1300 dropped even further to ~65.14%. Thus, we observed that MCHS carbonization temperature had the highest ROS scavenging prowess over any other carbonization temperature indicating the MCHS-900 being the ideal candidate.
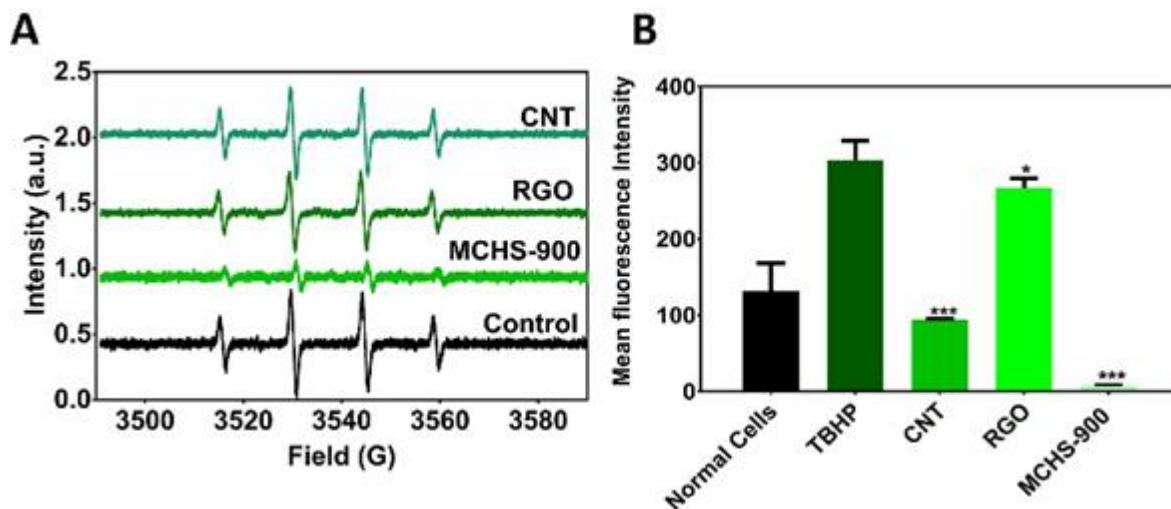
Fig 5.3 (A) Effect of different carbon nanoparticles on hydroxyl radicals generated by Fenton reaction measured by the intensity of EPR signal (B) Intracellular ROS scavenged by different carbon nanoparticles in HCT-116 cells, ns, *p<0.05, **p<0.01, ***p<0.001.

Fig.5.4 Bright field images of HCT-116 cells stained with DCFH2-DA (green fluorescence) after being incubated with tert-Butyl hydro peroxide and then treated with 25μg of carbon nanoparticles to detect their scavenging property (A) Positive control (B) CNT (C) RGO (D) MCHS-900

Fig 5.5 Confocal images of HCT-116 cells showing cellular uptake of carbon samples loaded with RhB with the same feeding amount of RhB determined from the loading capacity of the samples where (A)DAPI@Control PBS (B) PBS (C) DAPI combined with CNT@RhB (D)CNT@RhB (E)DAPI combined with MCHS-900@RhB (F)MCHS-900@rhB (G)DAPI combined with RGO@RhB (H) RGO@RhB. The scale bar is 2μm.

However, we wanted to investigate further how MCHS-900 in its pristine form compares to other carbon antioxidant agents are currently used as antioxidants, CNT and reduced graphene oxide. One of the most popular and engineered carbon allotrope C60 for potential biomedical application wasn't added to study group as it's a tendency to form strong aggregates in unmodified forms which weren't suitable for the fair comparison of other carbon forms in their unmodified versions.

To make a relative investigation of the antioxidant property of MCHS-900 with other carbon antioxidant agents, we conducted a visual fluorescent imaging test to verify the difference in fluorescence of ROS reactive dy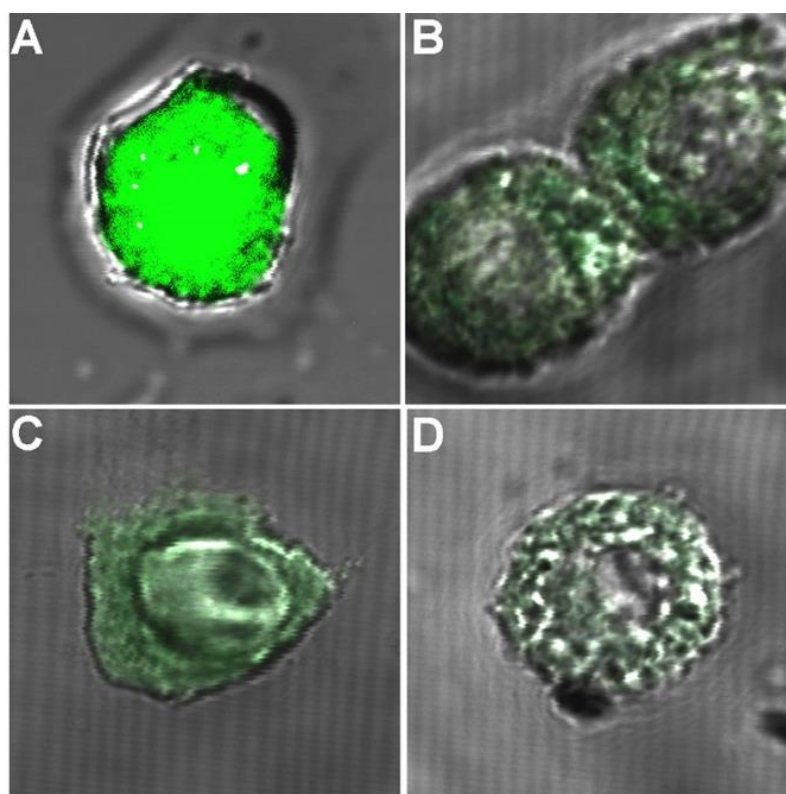e DCFH2-DA, where the intensity of the dye is proportional to the amount of ROS inside the cells. As shown in Fig. 5.4 (A), a strong green fluorescence indicates a state of extreme oxidative stress induced by TBHP. However, as shown in Fig. 5.4 (B), after incubating the cells stressed with high ROS levels with CNT, the fluorescence of the dye diminished indicating that some amount of ROS was successfully scavenged by CNT after its cellular interaction. However, the fluorescence coming from a cell that was subjected to RGO as antioxidant agents showed very little difference in the fluorescence, indicating the cellular interaction of pristine RGO is enormously less, Fig. 5.4 (C); thus; RGO is ineffective when it comes to scavenging ROS in pristine form.
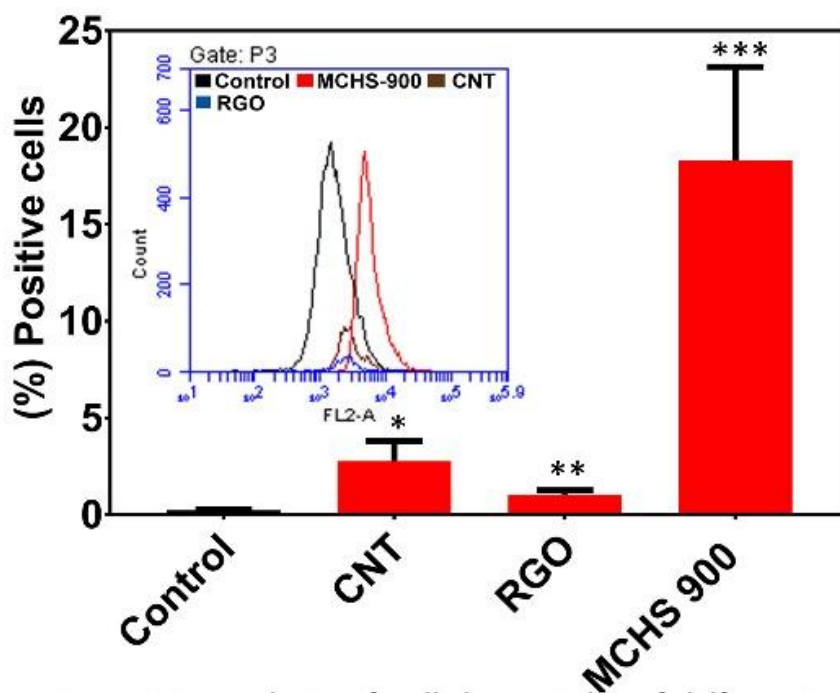
Fig 5.6 Flow cytometry analysis of cellular uptake of different carbon uptake of different carbon samples loaded with RhB in HCT-116 after 4 hours of incubation, inset cellular uptake histogram; where, ns, *p<0.05, **p<0.01, ***p<0.001.

When it comes to MCHS-900 however, the intensity of the green fluoresce was significantly diminished as can be seen in Fig.5.5 (D), indicating the high antioxidant property of pristine MCHS-900. To quantify the amount of ROS species scavenged by the carbon agents, flow cytometry analysis was performed, as shown in Fig.5.3 (B). The FACS results revealed MCHS-900 scavenged an average of ~93.67% of ROS while CNT reduced the ROS levels by ~33.5% and merely ~10 % of ROS was reduced by RGO. These results indicated that pristine MCHS-900 has superior antioxidant property and its very efficient ROS scavenging agent than other carbon-scavenging agents.

To understand the reason for the efficiency of MCHS-900 over other carbon agents, we conducted cellular uptake studies to observe the cellular interaction of MCHS-900 compared to other carbon-scavenging agents by loading fluorescent dye in the samples, then feeding the cells and then observing them under confocal microscopy. Pristine MCHS particles possess a relatively stronger capability to scavenge hydroxyl radicals compared with carbon nanotubes and reduced graphene oxide. It exhibited a far excellent antioxidant property than other nanoparticles in their primary forms. In the cellular uptake study, RhB dyes were loaded in each carbon-scavenging agents, and HCT-116 cells were exposed to equal amounts of RhB, and the number of carbon

nanoparticles was determined based on the loading capacity. It was evident, as shown in Fig. 5.5 (A-H) that there was substantial red fluorescence of RhB coming from the cytosol of the cells exposed to MCHS-900 as compared to CNT and RGO indicated superior cellular uptake of MCHS-900 than other samples. Further, flow cytometric analysis confirmed the observation with a quantitative measure of the cellular interaction with the nanoparticles. The cellular uptake FACS histogram indicated the highest mean fluorescence is coming from cells having an interaction with MCHS-900 compared to other samples. MCHS-900 showed an average of ~21.0 % positive cells; whereas, CNT had an average of merely ~2.77% positive cells and RGO had only ~1.03% of positive cells, as shown in Fig .5.6. These results suggest that MCHS-900 are incredibly beneficial for cellular interaction and are internalized in large amounts that in turn exposes a large number of nanoparticles to the ROS species inside the cells causing higher scavenging efficiency than other carbon nanoparticles.

5.4. Conclusions

In summary, EPR analysis of pristine MCHS carbonised at different temperatures revealed MCHS-900 carbonised at 900°C has remarkable ROS scavenging profile with an efficiency of 74 % reduction in OH$^\bullet$ in the aqueous environment. Further comparative EPR analysis revealed that MCHS-900 is 3.2 times and 2.7 times more effective than CNT and RGO, respectively. The intracellular study revealed MCHS-900 has the highest antioxidant activity in its pristine form among all the other MCHS samples carbonised at different temperatures; with ROS inhibition of 93.7 % as well as among other carbon-based antioxidant agents. The intracellular ROS scavenging efficacy was also confirmed via confocal imaging and flow cytometry. Moreover, intracellularly, CNT showed higher antioxidant activity than RGO, where CNT reduced TBHP induced oxidative stress in HCT-116 cells by ~30.41 % whereas RGO reduced the levels by ~17.4 %; which was a reverse trend in EPR analysis; indicating RGO having less cellular interaction than CNT (which was proven via cellular uptake study. The cellular uptake study revealed that MCHS-900 has the highest cellular uptake followed by CNT and then RGO. The high antioxidant efficacy of MCHS-900 could be attributed to ultrahigh cellular uptake and good ROS scavenging capability that is vital insight for chemotherapeutic and biomedical studies. Also, It sheds light on the prominence of carbonization temperature in mesoporous carbon spheres that dictates it's antioxidant capabilities.

Chapter 6

Carbonisation temperature optimised Mesoporous Carbon Hollow Spheres nanocarriers for chemo-photothermal therapy of cancer cells

This chapter reports the photothermal conversion efficiency of MCHS-T nanocarriers influenced by carbonisation temperature. This property can be utilised for an effective combined therapy as the nanocarriers deliver the anti-cancer drug molecule intracellularly while the nanocarrier themselves generate heat from irradiated light creating a state of intracellular hyperthermia.

6.1. Introduction:

Over the past few decades, there has been a steady growth in the development of chemotherapeutic practices. Chemotherapeutic agents that are being used in clinical practices presently inhibit cancer/tumour growth by different mechanisms of action such as attacking the DNA, inhibiting nucleotide metabolism, suppression of microtubule function[142]. Yet, a single hitting chemotherapy approach can cause remissions due to the unrestricted cell cycle of cancer which may not inhibit the cancer growth completely. That's why the concept of multi-hit modality and combination therapy is emerging. Usually, the stage and type of cancer often determine whether single therapy or combination therapy is needed. The rationale for combination chemotherapy is to use drugs that work by different mechanisms or in combination with radiation/photothermal therapy, thereby decreasing the likelihood that resistant cancer cells will develop. When drugs with different targeting methods are employed, we can achieve the highest efficiency of cancer eradication using drugs at its optimal dose, without intolerable side effects.

In light of the multi-hit concept, heat shock protein- 90 (Hsp90) has been considered as the "wonder drugs"[142, 143]. Hsp90 is a chaperone protein that assists other proteins in folding correctly, stabilising them against heat stress, and aiding in protein degradation. They are a class of chaperone proteins that are among the most highly expressed cellular proteins across all species[144]. As their name implies, heat shock proteins protect cells when stressed by elevated temperatures. They are found in heavy concentrations in cancer/tumour sites. That's why Hsp90 is a promising target in cancer therapy. Preclinical and clinical evaluations target the Hsp90 using a variety of Hsp90 inhibitors that have shown the antitumor effect as a single agent and in combination with chemotherapy. Geldanamycin (GA), a naturally occurring antibiotic isolated from *Streptomyces hygroscopicus* was the first Hsp90 inhibitor tested for anticancer/antitumor properties. Although GA exhibited potent anti-cancer activities in preclinical in vivo studies, it was determined to have little clinical potential mostly due to its high hepatotoxicity[145, 146]. As a result, a search for GA derivatives that maintain similar anti-cancer activities but with better toxicological properties was encouraged to be pursued. Thus, 17-AAG (17-allylamino-17-desmethoxygeldanamycin; Tanespimycin)[146, 147] was synthesized as a safer option than GA. It showed promising antitumor effects in Phase I [148, 149]and Phase II [150, 151]clinical trials.

However, several drawbacks of 17-AAG, such as low water-solubility, instability in solution, and low oral bioavailability may become an obstacle to further clinical

application [152, 153]. Thus, nanocarrier systems can provide the right assistance to overcome the limitations and enhance their effect and bioavailability. Among the numerous nanocarrier systems available, mesoporous carbon nanocarriers are the best choice for this purpose owing to the following reasons (i) low density, porous shells, accessible interior space, high surface area, large pore volume offers more significant advantage to load higher amounts of active drug/biomolecule[28, 75] (ii) they are highly non-toxic and biocompatible [23, 154] (iii) they have very intriguing optical and photothermal properties [155, 156]which makes them ideal nanocarrier systems for combination therapy using chemotherapy and photothermal therapy for cancer/tumour ablation. In our work, we aim to enhance the performance of 17 AAG in chemotherapy using mesoporous carbon nanocarriers as delivery vehicles. We integrated mesoporous carbon hollow spheres (MCHS) as nanocarrier systems to deliver high amounts of 17 AAG in cancer cells (chemotherapy) while irradiating them to inflict photothermal therapy simultaneously in combination.

As we know carbonization temperature plays a crucial role in the synthesis of MCHS-*T* in determining the physiochemical performance of the nanocarriers; thus, we also tested the up-conversion efficiency of irradiated light into heat. Our theory is that more intracellularly available 17AAG will be, more the cancer cells will get susceptible to thermal damage by its mechanism of action. Simultaneously the up-conversion of temperature optimized MCHS will elevate the heat intracellularly causing a combined therapeutic effect having maximum cancer cell death by creating an intracellular environment of hyperthermia. Hence, using optimized MCHS may function as a chemo-photothermal agent at the same time.
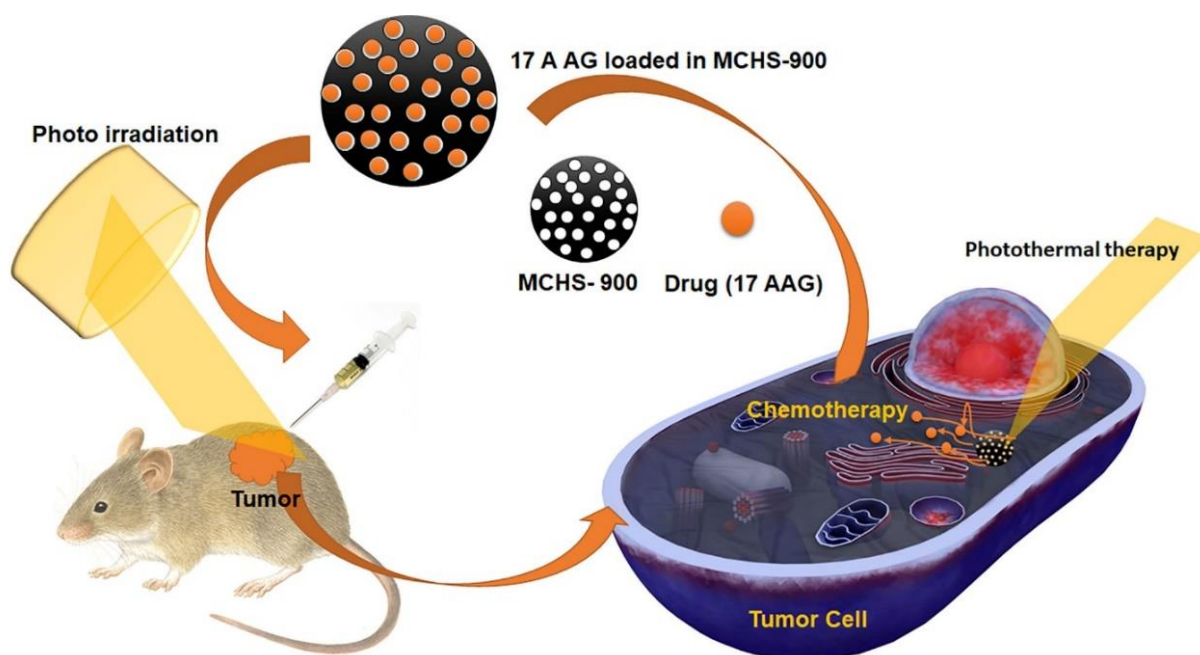
Fig 6.1 Schematic representation of the multi-hit modality of photothermal therapy and chemotherapy for a tumour and cancer cell ablation.

6.2. Materials Specifications:

MCHS-T were synthesized and carbonized according to the procedure described in Chapter 4. Cells were cultured in DMEM (Dulbecco's Modified Eagle Medium) with high glucose, L-glutamine and phenol Red as additives. DMEM were supplemented with 10 % Fetal Bovine Serum (FBS) and (1%), penicillin-streptomycin (10,000 U mL^{-1}). For subculturing purposes, the cells were washed with sterile PBS solutions and trypsin (0.25 g L^{-1}). The cells were attached to T75 flasks and incubated at 37 °C under 5% CO_2 sterile environment. For MTT assay, thiazolyl blue tetrazolium bromide (98%) was purchased from Sigma-Aldrich. UV irradiation was conducted using ML-3500 Series, MAXIMA™ Ultra-High Intensity UV-A Lamp that utilises micro discharge light (MDL) technology with a spot reflector has a nominal steady-state UV-A intensity of *50,000 µW/cm^2* at 240 V, 15 inches (38 cm).

6.3. Characterization:

UV-Vis characterizations were done using TECAN Infinite® 200 PRO microplate reader. The optical properties of the nanoparticles were analysed using UV-2450 Shimadzu Spectrophotometer.

6.4. Experimental section:

6.4.1. UV-Vis Spectral analysis and photothermal test

To test the spectral absorbance behaviour of MCHS-*T*, UV-Vis spectrophotometric analysis was conducted. The samples were prepared by making 1mg/mL solutions in PBS and thoroughly dispersing them by exposing them to ultra-sonication for 5 min. Then 50 µg/mL solution of MCHS-*T* were prepared and analysed under spectrometer baselining PBS. The photothermal tests were conducted to measure the ability of nanoparticle to convert incident light into heat. Two different concentrations of the particles (75 µg/mL and 200 µg/mL) were prepared and suspended in PBS solutions and were ultrasonicated for 10 min to achieve even distribution of nanoparticles in PBS. After that, the MCHS-*T* solutions were irradiated for 3 minutes by a UV light source enclosed in a dark box. The temperature changes were detected using a digital thermometer to detect the temperature changes.

6.4.1. Loading and release study:

For the loading test, first the active molecule "Tanespimycin (17-*N*-allylamino-17-demethoxygeldanamycin, 17-AAG) "was dissolved in DMSO (Dimethyl sulfoxide) making a concentrated suspension of 5 µg/mL concentration designated as the stock solution. A measured amount of the stock solution was dissolved in sterile phosphate buffer to make 125 ng/mL of solution (Solution A). Then 100 µL of solution A was added to 1mg of MCHS-*T* samples in Eppendorf tubes, and the final suspensions were ultrasonicated for 10 min in an ultrasonicator bath while maintaining the water temperature at 4°C. Then the sample tubes were rotated in tube rotor for 24 hours in a cold room (in 4°C temperature) in complete darkness. The samples were retrieved and then centrifuged at 15000 rpm for 10 min. In the end, the supernatant was separated and observed under NanoDrop UV- Vis spectrometer at 335 nm.

To study the release of 17 AAG from MCHS-*T*, the drug-loaded particles were dispersed in 1 mL of buffer at pH 7.4 in Eppendorf tube. The tubes were placed in a dark room with 150 rpm at 37°C. At the predetermined time intervals, the nanomaterials solution was centrifuged at 13000 rpm for 10 min, and the supernatant was withdrawn. Then 50µL of the suspension was withdrawn for analysis and replaced by an equal amount of fresh PBS, and then the concentrations of the released drug were analysed at those predetermined time intervals as cumulative release amounts.

6.4.2. Chemo-photothermal therapy cell viability test using MTT assay

The cell viability test was carried out by MTT (3-(4, 5-Dimethylthiazol-2-yl)-2, 5-Diphenyltetrazolium Bromide) assay. Cellular toxicity of MCHS-T was tested by exposing MCF 7 cells with 17AAG loaded MCHS-T, incubating for a required period, irradiating it with UV irradiation for 3 min and measuring the absorbance of added MTT solution under UV-Vis spectrophotometer. MCF 7 cells were seeded in 24-well plate at a density of 0.05 x 106 cells/well. Then the cells were incubated for 24 hours at 37 °C in 5 % CO2 sterile environment for the cells to attach to the plate surface. After the 24 hours incubation, the cells were treated with an aqueous suspension of MCHS-T loaded with 17AAG, where the final concentrations of the loaded 17AAG were 12.5 ng mL-1. Then the cells were incubated overnight for the cells to uptake the MCHS-T loaded with 17 AAG. After that, the cells were irradiated with high-intensity UV light for 3 min. Then the media was removed and washed with sterile PBS solution. Then 1mL of 10 % MTT solution was added to each well, and the cells were incubated at 37 °C for 4 hours.   After the incubation, the solution was removed, and 500 µL of DMSO was added to each well and shaken in Microtiter/PCR Plate Shaker for 15 minutes. The absorbance of the resultant formazan was measured in UV-Vis spectrophotometer at 570 nm. The following formula was applied to calculate the cell survival rate:

$$Cell\ Viability\ (\%) = \frac{(mean\ abs.\ of\ treated\ group)}{(mean\ abs.\ of\ control\ group)}\ X\ 100$$

6.4.3. Biocompatibility using MTT assay

Biocompatibility of the nanoparticles was also tested using MTT assay. Varied concentrations of MCHS-T were suspended in sterile PBS solutions and ultrasonicated for 10 minutes for even distribution in PBS. MCF 7 cells were seeded in 24-well plate at a density of 0.05 x 10^6 cells/well. Then the cells were incubated for 24 hours at 37 °C in 5 % CO_2 sterile environment for the cells to attach to the plate surface. Concentrations of 10 µg/mL, 20 µg/mL, 40 µg/mL, 60 µg/mL, 80 µg/mL, 100 µg/mL, 200 µg/mL of MCHS-T were added to cells and further incubated for 24 hours. Then the media was removed and 1mL of 10 % MTT solution was added to each well, and the cells were incubated with at 37 °C for 4 hours which the solution was removed, and 500 µL of DMSO was added to each well and shaken in Microtiter/PCR Plate Shaker for 15 minutes. The absorbance of the resultant formazan was measured in

UV-Vis spectrophotometer at 570 nm. The cell survival was calculated using the cell viability formula mentioned above.

6.5. Result and Discussion:

To test the feasibility of 17 AAG@MCHS-*T* as photothermal agents, we chose a UV light source to irradiate the particles, and we irradiated them for 3 minutes interval.
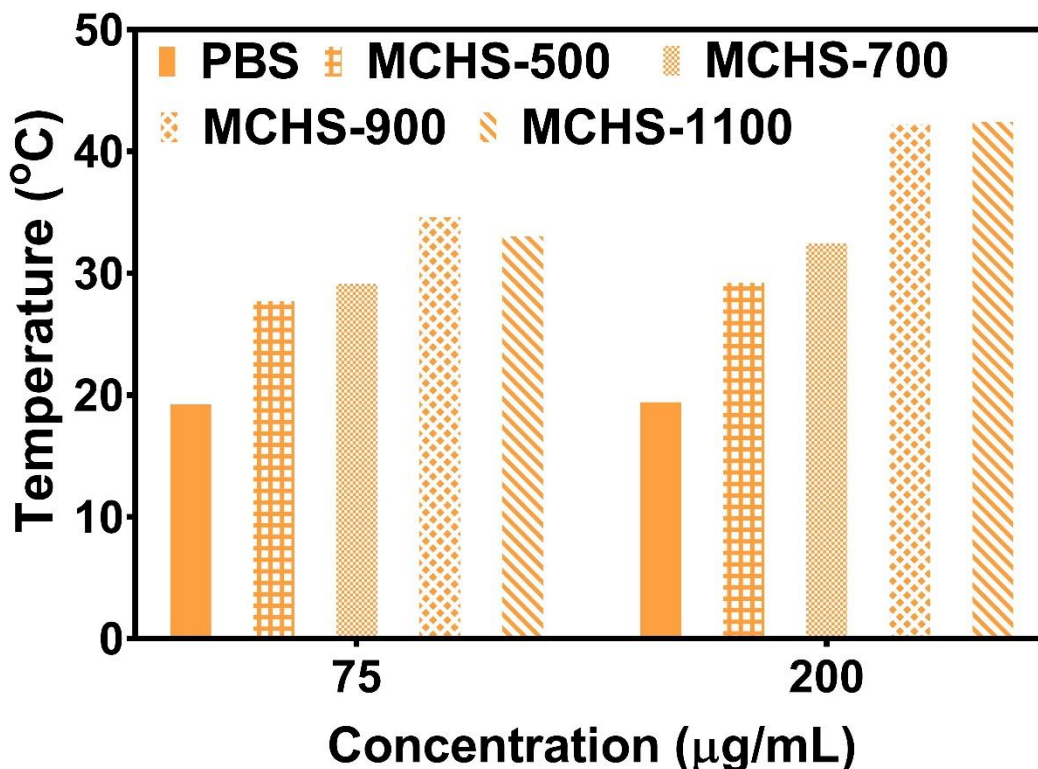
Fig 6.2 Photothermal heating graph of MCHS-T at different concentrations of 75 µg/ml and 200 µg/mL after UV-A irradiation for 3 min.

For this test, two different concentrations of MCHS-*T* were prepared as shown in Fig 6.2. Before irradiation, the temperature of all the nanoparticles suspension groups including the control group was measured, and all were detected to be an average of 19.8°C. When the control group PBS buffer was irradiated, no changes were observed in the temperature before and after irradiation. After adding 75 µg/mL of MCHS-500, the temperature of the suspension increased by the mark of ~ Δ 8.3°C. We observed, the higher the MCHS-*T* were carbonised during the synthesis process, the ability of photothermal conversion was also higher. MCHS-(700, 900, and 1100) were able to increase the temperature to 29.7°C, 35.2 °C and 33.6°C respectively. When the concentration of MCHS-*T* was increased to 200 µg/mL, the photothermal conversion improved as well. It was noted that MCHS-900 and MCHS-1100 reached over 40°C

which is considered to be the temperature of clinical significance. The aim of photothermal therapy is usually to reach the temperature of clinical significance to create an environment of hyperthermia inside tumour microenvironment[157]. The primary reason for the thermal conversion property might be attributed to the carbon content and carbon crystallinity in nanomaterials[158]. Carbonising nanoparticles to higher temperatures enhance the carbon crystallinity and carbon-carbon linkage that helps with the thermal generation and conduction. In this challenge, MCHS-900 emerged as a clear winner as it has high aqueous stability along with desired carbon features for photothermal conversion. When the temperature reaches higher than 900°C, the aqueous stability of the nanoparticles is compromised which limits its clinical use.
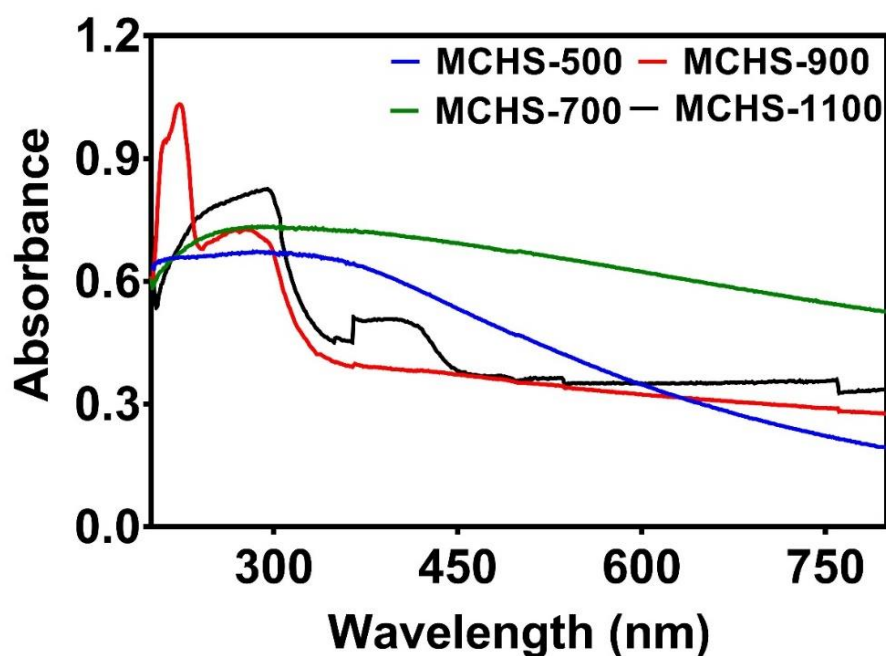
Fig 6.3 UV-Vis spectral analysis of MCHS-*T* in PBS buffer solution at pH 7.4.

The efficiency of photothermal conversion can be clarified by the ability of MCHS-*T* to absorb light. To test the photo-absorption of nanoparticles UV-Vis spectrum was recorded. We detected the UV-Vis spectra of MCHS-500 to 1100 in PBS in the same concentration using PBS as a baseline. As shown in Fig 6.3, MCHS-900 demonstrated a characteristic sharp absorption peak at 223 nm. Meanwhile, MCHS-500 and MCHS-700 didn't display similar peaks in that spectral range. MCHS-1100 showed peaks around 285nm -300 nm which indicates that M CHS-900 has better UV- A light absorption capacity than MCHS-1100. The high photoabsorption of MCHS-900 can

explain the high photoconversion of UV-A irradiated light into thermal energy ability demonstrated the best photothermal conversion efficiency among all MCHS-T.
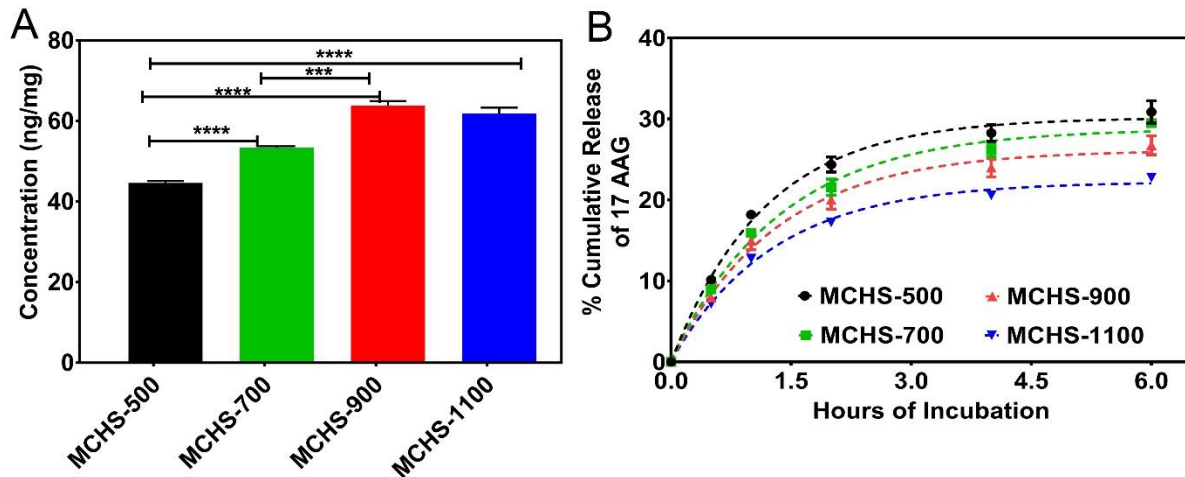
Fig 6.4. (A) The loading efficiency of 17 AAG in MCHS-T (B) the release profile of MCHS-T, ns p> 0.05, *p<0.05, **p<0.01, ***p<0.001.

The structural features of MCHS-T are highly desirable for drug delivery owing to large surface area and mesopores. However, these advantageous features are dictated by the temperature at which the nanoparticle templates are carbonised. To evaluate the loading performance of MCHS-T, 125 ng mL^{-1} of 17 AAG (Tanespimycin) were mixed with nanoparticles in PBS buffer solution at neutral pH. Fig 6.4 shows MCHS-500 had the lowest loading capacity while MCHS-900 had the highest loading with a mean of ~65 ng of 17 AAG. The existence of hydrophobic behaviour and high dispersibility made 17 AAG loading very reasonable. With the lower carbonisation temperature like 500°C and 700°C, the hydrophobic nature of the nanoparticles are compromised which lowers the loading capacity of the particles. However, MCHS-1100 had a lower loading amount than MCHS-900, probably due to the poor aqueous distribution and aggregation in PBS. The release profile of MCHS-T showed a clear trend as shown in Fig 6.4(B). The in-situ release of 17AAG was evaluated in a PBS buffer solution at 37°C for more than 6 hours. These first 6 hours are essential for the cells to uptake the nanocarriers to release the HSP90 inhibitor intracellularly for the inactivation of heat shock protein categorised under chemotherapy. We observed that the temperature at which MCHS was carbonised is directly proportional to the percentage % release of 17 AAG. The sustained release of 17 AAG was more in MCHS carbonised at a higher temperature than lower temperature. As previously demonstrated, the hydrophobicity of the nanocarriers enhances along with carbonisation temperature. Thus the hydrophobic interaction between the drug molecules and the nanocarriers are higher attributing to more sustained release. We

observed that while MCHS carbonised at lower temperature release an average of 31% of the drug by the 6th hour, MCHS-900 released 29.5% while MCHS-1100 released only 22%. While usually cancer therapeutic drug delivery, sustained release of the drug molecule is a desired trait, however, in combination therapy, the release should be enough to elicit a desired chemotherapeutic response so that the photothermal effect can kick in a synergistic effect. This enhanced effect was tested further in cell viability tests.
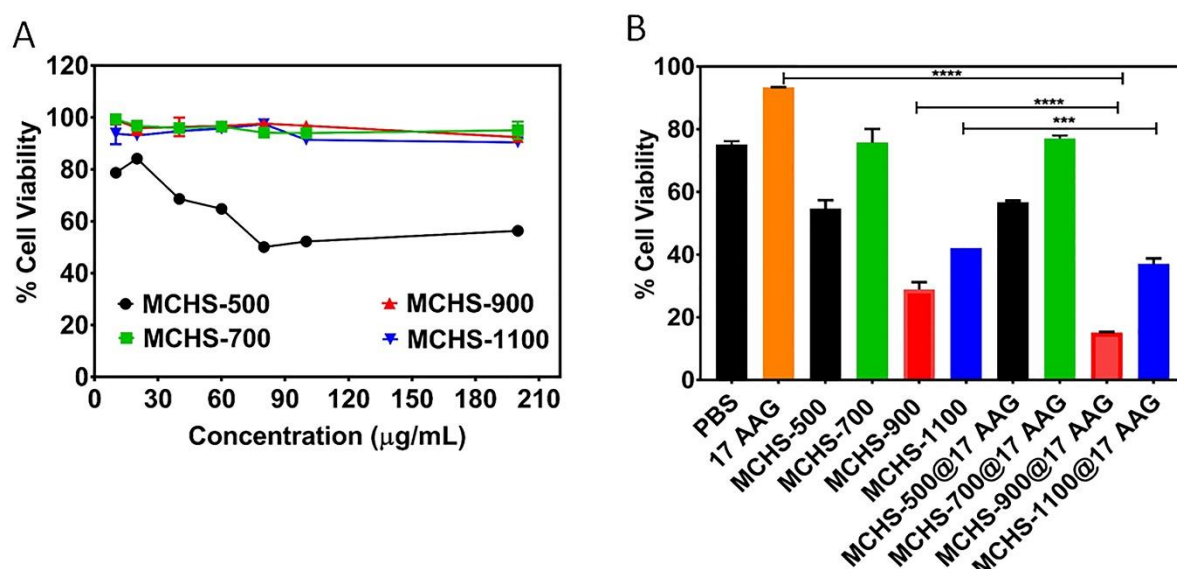
Fig 6.5 (A) Dosage-dependent cell viability of MCF 7 cells treated with bare testing the biocompatibility of MCHS-T after 24 hours incubation (B) Cell viability of MCF 7 after combination therapy by exposing them to pure 17 AAG, only MCHS-T and 17 AAG loaded in MCHS-T and after irradiation with UV light irradiation for 3 minutes; ns p> 0.05, *p<0.05, **p<0.01, ***p<0.001.

The in-vitro cytotoxicity of MCHS-*T* of MCF 7 cells was investigated by MTT assay. Fig 6.5 (A) showed no obvious cytotoxicity to MCF 7cells from a concentration of 10-200 µg of MCHS- *T*. We could observe MCHS-700, 900 and 1100 had very low influence in the concentration of the cells. However, MCHS-500 showed fairly high toxicity where the toxicity was proportional to the concentration of the nanoparticles. The display of higher toxicity with low carbonisation temperature may be attributed to cytotoxicity brought about by the residual polymer in the carbon framework in MCHS-500 which are absent in MCHS carbonised at a higher temperature.

MTT analysis was also used to test the cell viability of MCF 7 cells after combination therapy. After adding 12.5 ng of drug molecule combined with irradiation, there wasn't any significant decrease in cancer cell concentration. This may be due to the inability of the ultra-sensitive drug molecule to penetrate the cell membrane. However, when bare particles were irradiated with UV irradiation, MCHS-900 showed inhibition of cells

of about 75% mean, owing to its high photoconversion efficiency, previously observed in the photothermal test. MCHS-900 in itself was able to create a state of hyperthermia in the cancer cells owing to its high cellular uptake and high photoconversion efficiency. MCHS-1100 wasn't able to create similar effects due to limited cellular uptake. MCHS-500 and MCHS-700, on the other hand, displayed low to moderate cell inhibition. However, when MCHS-*T* was combined with chemotherapy, the cellular inhibition of MCF 7 cells was enhanced due to its dual targeting. After the cells were exposed to 17 AAG loaded MCHS-*T*, 17AAG were escorted and released intracellularly making the cells sensitive to thermal damage. Thus, after irradiation the state of hyperthermia caused the cells to die off. This combination therapy was most significant in MCHS-900 loaded with 17AAG as shown in Fig 6.5 (B). Because of the high cellular uptake efficiency of MCHS-900, 17 AAG was escorted inside the cell very effectively which allowed it to act on the chaperone protein aka. HSP 90 proteins of the cancer cells forcing them to become inactive. This caused the cancer cells unable to defend or repair itself from the heat produced intracellularly causing significant damage to cancer cells.

6.6. Conclusion:

In summary, all the above test demonstrated that the photoconversion efficiency of mesoporous carbon nanoparticles could be tuned by tuning its carbonisation temperature. MCHS-900 showed the most efficient photoconversion ability where 200 µg of the nanoparticles were able to raise the temperature to clinical significance. The photothermal test revealed that MCHS-900 and MCHS-1100 had high photoconversion of irradiated UV light that MCHS-500 or MCHS-700. Not only that MCHS-900, owing to its hydrophobicity, mesoporosity and high surface area was able to load the highest amount of drug 17 AAG along with a sustained release. Moreover, MCHS-900 also showed high biocompatibility and high cellular toxicity when combined with a drug molecule and used in combination with photothermal therapy.

6.7. List of References:

1. J. Wang, Z. Hu, J. Xu and Y. Zhao, *Npg Asia Mater*, 2014, **6**, e84.

2. G. S. Hong, S. O. Diao, A. L. Antaris and H. J. Dai, *Chemical Reviews*, 2015, **115**, 10816-10906.

3. K. Kostarelos, A. Bianco and M. Prato, *Nat Nanotechnol*, 2009, **4**, 627-633.

4. Y. P. Sun, K. F. Fu, Y. Lin and W. J. Huang, *Accounts Chem Res*, 2002, **35**, 1096-1104.

5. I. Khan, K. Saeed and I. Khan, *Arabian Journal of Chemistry*, 2017, DOI: https://doi.org/10.1016/j.arabjc.2017.05.011.

6. A. C. Tripathi, S. A. Saraf and S. K. Saraf, *Materials*, 2015, **8**, 3068-3100.

7. R. Singh and J. W. Lillard, *Experimental and molecular pathology*, 2009, **86**, 215-223.

8. D. Peer, J. M. Karp, S. Hong, O. C. Farokhzad, R. Margalit and R. Langer, *Nat Nano*, 2007, **2**, 751-760.

9. K. J. Cho, X. Wang, S. M. Nie, Z. Chen and D. M. Shin, *Clin Cancer Res*, 2008, **14**, 1310-1316.

10. O. Harush-Frenkel, Y. Altschuler and S. Benita, *Crit Rev Ther Drug*, 2008, **25**, 485-544.

11. H. Hillaireau and P. Couvreur, *Cell Mol Life Sci*, 2009, **66**, 2873-2896.

12. B. R. Bitner, D. C. Marcano, J. M. Berlin, R. H. Fabian, L. Cherian, J. C. Culver, M. E. Dickinson, C. S. Robertson, R. G. Pautler, T. A. Kent and J. M. Tour, *ACS Nano*, 2012, **6**, 8007-8014.

13. Y. Qiu, Z. Wang, A. C. E. Owens, I. Kulaots, Y. Chen, A. B. Kane and R. H. Hurt, *Nanoscale*, 2014, **6**, 11744-11755.

14. R. Huq, E. L. G. Samuel, W. K. A. Sikkema, L. G. Nilewski, T. Lee, M. R. Tanner, F. S. Khan, P. C. Porter, R. B. Tajhya, R. S. Patel, T. Inoue, R. G. Pautler, D. B. Corry, J. M. Tour and C. Beeton, *Sci Rep-Uk*, 2016, **6**, 33808.

15. G. Ku, M. Zhou, S. Song, Q. Huang, J. Hazle and C. Li, *ACS Nano*, 2012, **6**, 7489-7496.

16. M.-F. Tsai, S.-H. G. Chang, F.-Y. Cheng, V. Shanmugam, Y.-S. Cheng, C.-H. Su and C.-S. Yeh, *ACS Nano*, 2013, **7**, 5330-5342.

17. K. Li and B. Liu, *Chemical Society Reviews*, 2014, **43**, 6570-6597.

18. C. Xie, P. K. Upputuri, X. Zhen, M. Pramanik and K. Pu, *Biomaterials*, 2017, **119**, 1-8.

19. P. Chakravarty, R. Marches, N. S. Zimmerman, A. D.-E. Swafford, P. Bajaj, I. H. Musselman, P. Pantano, R. K. Draper and E. S. Vitetta, *Proceedings of the National Academy of Sciences*, 2008, **105**, 8697-8702.

20. J. T. Robinson, K. Welsher, S. M. Tabakman, S. P. Sherlock, H. Wang, R. Luong and H. Dai, *Nano Research*, 2010, **3**, 779-793.

21. R. Sharma and C. J. Chen, *Journal of Nanoparticle Research*, 2009, **11**, 671-689.

22. W. Qiao, B. Wang, Y. Wang, L. Yang, Y. Zhang and P. Shao, *Journal of Nanomaterials*, 2010, **2010**.

23. Y. Fang, D. Gu, Y. Zou, Z. Wu, F. Li, R. Che, Y. Deng, B. Tu and D. Zhao, *Angewandte Chemie*, 2010, **49**, 7987-7991.

24. J. Lu, M. Liong, J. I. Zink and F. Tamanoi, *Small*, 2007, **3**, 1341-1346.

25. B. R. Selvi, D. Jagadeesan, B. S. Suma, G. Nagashankar, M. Arif, K. Balasubramanyam, M. Eswaramoorthy and T. K. Kundu, *Nano Lett*, 2008, **8**, 3182-3188.

26. J. Liu, N. P. Wickramaratne, S. Z. Qiao and M. Jaroniec, *Nature materials*, 2015, **14**, 763-774.

27. J. Gu, S. Su, Y. Li, Q. He and J. Shi, *Chem. Commun.*, 2011, **47**, 2101-2103.

28. H. Zhang, M. Yu, H. Song, O. Noonan, J. Zhang, Y. Yang, L. Zhou and C. Yu, *Chemistry of Materials*, 2015, **27**, 6297-6304.

29. T. W. Kim, P. W. Chung, I. I. Slowing, M. Tsunoda, E. S. Yeung and V. S. Y. Lin, *Nano Lett*, 2008, **8**, 3724-3727.

30. A. Bianco, K. Kostarelos and M. Prato, *Current Opinion in Chemical Biology*, 2005, **9**, 674-679.

31. M. Manning, K. Patel and R. Borchardt, *Pharm Res*, 1989, **6**, 903-918.

32. Z. Gu, A. Biswas, M. Zhao and Y. Tang, *Chem Soc Rev*, 2011, **40**, 3638-3655.

33. C. J. Lee, J. Park, Y. Huh and J. Yong Lee, *Chem Phys Lett*, 2001, **343**, 33-38.

34. Z. Abbasi, E. Shamsaei, S. K. Leong, B. Ladewig, X. Zhang and H. Wang, *Microporous and Mesoporous Materials*, 2016, **236**, 28-37.

35. T.-H. Ko, W.-S. Kuo and Y.-H. Chang, *Polymer Composites*, 2000, **21**, 745-750.

36. Q. Zhao, Y. Lin, N. Han, X. Li, H. Geng, X. Wang, Y. Cui and S. Wang, *Drug Delivery*, 2017, **24**, 94-107.

37. L. Zhou, K. Dong, Z. Chen, J. Ren and X. Qu, *Carbon*, 2015, **82**, 479-488.

38. Y. Fang, D. Gu, Y. Zou, Z. Wu, F. Li, R. Che, Y. Deng, B. Tu and D. Zhao, *Angewandte Chemie International Edition*, 2010, **49**, 7987-7991.

39. L. B. Zhou, Y. Jing, Y. B. Liu, Z. H. Liu, D. Y. Gao, H. B. Chen, W. Y. Song, T. Wang, X. F. Fang, W. P. Qin, Z. Yuan, S. Dai, Z. A. Qiao and C. F. Wu, *Theranostics*, 2018, **8**, 663-675.

40. G. J. Xu, S. J. Liu, H. Niu, W. P. Lv and R. A. Wu, *Rsc Adv*, 2014, **4**, 33986-33997.

41. C. Liang, Z. Li and S. Dai, *Angewandte Chemie International Edition*, 2008, **47**, 3696-3717.

42. A. G. Whitman, P. J. Lambert, O. F. Dyson and S. M. Akula, in *Emerging Conceptual, Ethical and Policy Issues in Bionanotechnology*, ed. F. Jotterand, Springer Netherlands, Dordrecht, 2008, DOI: 10.1007/978-1-4020-8649-6_8, pp. 117-130.

43. V. Bhardwaj and A. Kaushik, *Micromachines-Basel*, 2017, **8**.

44. P. Mulvaney, *Acs Nano*, 2015, **9**, 2215-2217.

45. B. Panchapakesan and E. Wickstrom, *Surgical Oncology Clinics of North America*, 2007, **16**, 293-305.

46. E. Bradley, E. Bieberich, F. Mivechi Nahid, D. Tangpisuthipongsa and G. Wang, *STEM CELLS*, 2012, **30**, 1624-1633.

47. C. Wei, L. Junbai and D. Gero, *Advanced Materials*, 2016, **28**, 1302-1311.

48. S. M. Dizaj, S. Jafari and A. Y. Khosroushahi, *Nanoscale Research Letters*, 2014, **9**, 252-252.

49. Q.-L. Zhou, Z.-Y. Chen, Y.-X. Wang, F. Yang, Y. Lin and Y.-Y. Liao, *Biomed Res Int*, 2014, **2014**, 13.

50. M. Mazaheri, N. Eslahi, F. Ordikhani, E. Tamjid and A. Simchi, *International Journal of Nanomedicine*, 2015, **10**, 6039-6054.

51. A. Chowdhury, S. Kunjiappan, T. Panneerselvam, B. Somasundaram and C. Bhattacharjee, *International Nano Letters*, 2017, **7**, 91-122.

52. T. C. Pagonis, J. Chen, C. R. Fontana, H. Devalapally, K. Ruggiero, X. Song, F. Foschi, J. Dunham, Z. Skobe, H. Yamazaki, R. Kent, A. C. R. Tanner, M. M. Amiji and N. S. Soukos, *Journal of endodontics*, 2010, **36**, 322.

53. *Journal*, 2007.

54. W. Fu, B. An, X. Wang and J. Qu, *Bioanalysis*, 2017, **9**, 1349-1352.

55. M. M. Abhyankar, M. T. Orr, S. Lin, M. O. Suraju, A. Simpson, M. Blust, T. Pham, J. A. Guderian, M. A. Tomai, J. Elvecrog, K. Pedersen, W. A. Petri and C. B. Fox, *npj Vaccines*, 2018, **3**, 22.

56. S. Changrob, A. M. McHenry, M. H. Nyunt, J. Sattabongkot, E.-T. Han, J. H. Adams and P. Chootong, *Scientific Reports*, 2018, **8**, 8347.

57. A. S. Lubiniecki, *Cytotechnology*, 1998, **28**, 139-145.

58. C. J. Sherr, *Science*, 1996, **274**, 1672-1677.

59. H. E. Davis and J. K. Leach, *Ann Biomed Eng*, 2011, **39**, 1-13.

60. S. Nozaki, J. G. W. Sledge and H. Nakshatri, *Oncogene*, 2001, **20**, 2178.

61. H. Shen, M. Liu, H. He, L. Zhang, J. Huang, Y. Chong, J. Dai and Z. Zhang, *ACS Applied Materials & Interfaces*, 2012, **4**, 6317-6323.

62. N. Serna, L. Sánchez-García, U. Unzueta, R. Díaz, E. Vázquez, R. Mangues and A. Villaverde, *Trends in Biotechnology*, 2018, **36**, 318-335.

63. S. F. Oliveira, G. Bisker, N. A. Bakh, S. L. Gibbs, M. P. Landry and M. S. Strano, *Carbon*, 2015, **95**, 767-779.

64. B. Yu, H. C. Tai, W. Xue, L. J. Lee and R. J. Lee, *Mol Membr Biol*, 2010, **27**, 286-298.

65. P.-C. Hsu, P.-C. Chen, C.-M. Ou, H.-Y. Chang and H.-T. Chang, *Journal of Materials Chemistry B*, 2013, **1**, 1774-1781.

66. N. W. Shi Kam, T. C. Jessop, P. A. Wender and H. Dai, *Journal of the American Chemical Society*, 2004, **126**, 6850.

67. N. W. S. Kam, Z. Liu and H. Dai, *Angewandte Chemie International Edition*, 2006, **45**, 577-581.

68. N. G. Sahoo, H. Bao, Y. Pan, M. Pal, M. Kakran, H. K. F. Cheng, L. Li and L. P. Tan, *Chemical Communications*, 2011, **47**, 5235-5237.

69. F. Yang, G. E. LeCroy, P. Wang, W. Liang, J. Chen, K. A. S. Fernando, C. E. Bunker, H. Qian and Y.-P. Sun, *The Journal of Physical Chemistry C*, 2016, **120**, 25604-25611.

70. F. Yin, Z. Gengfeng, Y. Jianping, T. Haosha, Z. Yafeng, K. Biao, L. Yingying, X. Congjian, A. A. M., Z. Jian, Z. Fan and Z. Dongyuan, *Angewandte Chemie*, 2014, **126**, 5470-5474.

71. M. Jambhrunkar, M. Yu, H. Zhang, P. Abbaraju, A. K. Meka, A. Cavallaro, Y. Lu, N. Mitter and C. Yu, *Nano Res*, 2018, **11**, 370-382.

72. L. Chengdu, L. Zuojiang and D. Sheng, *Angewandte Chemie International Edition*, 2008, **47**, 3696-3717.

73. J. H. Knox, K. K. Unger and H. Mueller, *Journal of Liquid Chromatography*, 1983, **6**, 1-36.

74. H. Zhang, X. Huang, O. Noonan, L. Zhou and C. Yu, *Adv Funct Mater*, 2017, **27**, 1606023-n/a.

75. H. Zhang, O. Noonan, X. Huang, Y. Yang, C. Xu, L. Zhou and C. Yu, *Acs Nano*, 2016, **10**, 4579-4586.

76. C. Swaroop, D. G. S. and M. S. K., *Journal of Biomedical Materials Research Part A*, 2017, **105**, 2906-2928.

77. A. Albanese, P. S. Tang and W. C. Chan, *Annual review of biomedical engineering*, 2012, **14**, 1-16.

78. S. E. Gratton, *Proc. Natl Acad. Sci. USA*, 2008, **105**, 11613-11618.

79. S. E. A. Gratton, *J. Control. Rel.*, 2007, **121**, 10-18.

80. C. D. Walkey, J. B. Olsen, H. Guo, A. Emili and W. C. W. Chan, *Journal of the American Chemical Society*, 2012, **134**, 2139-2147.

81. Z. Peng, D. Zhang, L. Shi and T. Yan, *J Mater Chem*, 2012, **22**, 6603-6612.

82. M. M. Aljumaily, M. A. Alsaadi, R. Das, S. B. A. Hamid, N. A. Hashim, M. K. AlOmar, H. M. Alayan, M. Novikov, Q. F. Alsalhy and M. A. Hashim, *Sci Rep-Uk*, 2018, **8**, 2778.

83. Z. Z. Jiang, Z. B. Wang, H. Rivera, W. L. Qu and D. M. Gu, *Fuel Cells*, 2014, **14**, 660-666.

84. J. K. Shon, X. Jin, Y. S. Choi, J. G. Won, Y. K. Hwang, D. J. You, C. Li and J. M. Kim, *Carbon Lett*, 2016, **20**, 66-71.

85. T. A. Centeno and A. B. Fuertes, *Journal of Membrane Science*, 1999, **160**, 201-211.

86. T. H. Ko, W. S. Kuo and Y. H. Chang, *J Appl Polym Sci*, 2001, **81**, 1084-1089.

87. A. Galano, *The Journal of Physical Chemistry C*, 2008, **112**, 8922-8927.

88. E. L. G. Samuel, M. T. Duong, B. R. Bitner, D. C. Marcano, J. M. Tour and T. A. Kent, *Trends in Biotechnology*, 2014, **32**, 501-505.

89. J. Li, M. Guan, T. Wang, M. Zhen, F. Zhao, C. Shu and C. Wang, *ACS Applied Materials & Interfaces*, 2016, **8**, 25770-25776.

90. W. Sheng, S. He, W. J. Seare and A. Almutairi, *Review of the progress toward achieving heat confinement—the holy grail of photothermal therapy*, SPIE, 2017.

91. in *Carbon Nanomaterials for Bioimaging, Bioanalysis, and Therapy*, DOI: 10.1002/9781119373476.ch12.

92. F. Dietzel, in *Vascular Perfusion in Cancer Therapy*, eds. K. Schwemmle and K. Aigner, Springer Berlin Heidelberg, Berlin, Heidelberg, 1983, DOI: 10.1007/978-3-642-82025-0_31, pp. 177-190.

93. D. Zhang, M. Wu, Y. Zeng, L. Wu, Q. Wang, X. Han, X. Liu and J. Liu, *ACS Applied Materials & Interfaces*, 2015, **7**, 8176-8187.

94.   H. S. Jung, P. Verwilst, A. Sharma, J. Shin, J. L. Sessler and J. S. Kim, *Chem Soc Rev*, 2018, **47**, 2280-2297.

95.   in *Semiconductor Quantum Dots and Rods for In Vivo Imaging and Cancer Phototherapy*, DOI: 10.1142/9789813142893_0006, pp. 111-139.

96.   H. K. Moon, S. H. Lee and H. C. Choi, *Acs Nano*, 2009, **3**, 3707-3713.

97.   W. Wang, Z. Wang, Y. Liu, N. Li, W. Wang and J. Gao, *Materials Research Bulletin*, 2012, **47**, 2245-2251.

98.   X. Wang, C. Wang, L. Cheng, S.-T. Lee and Z. Liu, *Journal of the American Chemical Society*, 2012, **134**, 7414-7422.

99.   D. Q. Chen, C. Wang, X. Nie, S. M. Li, R. M. Li, M. R. Guan, Z. Liu, C. Y. Chen, C. R. Wang, C. Y. Shu and L. J. Wan, *Adv Funct Mater*, 2014, **24**, 6621-6628.

100.   M. M. Kantor, *Ind Lab+*, 1981, **47**, 1148-1159.

101.   M. J. Thun, J. O. DeLancey, M. M. Center, A. Jemal and E. M. Ward, *Carcinogenesis*, 2010, **31**, 100-110.

102.   T. Hiroi and M. Shibayama, *Journal of Visualized Experiments : JoVE*, 2017, DOI: 10.3791/54885, 54885.

103.   D. K. Carpenter, *Journal of Chemical Education*, 1977, **54**, A430.

104.   A. Proctor and P. M. A. Sherwood, *Analytical Chemistry*, 1982, **54**, 13-19.

105.   J. S. Cavenaugh, G. von Laszewski, T. R. Mosmann, J. Rebhahn, S. Datta, I. Naim, G. Sharma, A. Pangborn, D. Roberts, J. Espenshade and H. L. Wu, *Cytom Part B-Clin Cy*, 2009, **76B**, 397-398.

106.   B. Leader, Q. J. Baca and D. E. Golan, *Nat Rev Drug Discov*, 2008, **7**, 21-39.

107.   G. R. Devi, *Cancer Gene Ther*, 2006, **13**, 819-829.

108.   M. H. Yu, Z. Y. Gu, T. Ottewell and C. Z. Yu, *J Mater Chem B*, 2017, **5**, 3241-3252.

109.   S. K. Das, M. K. Bhunia, D. Chakraborty, A. R. Khuda-Bukhsh and A. Bhaumik, *Chem Commun*, 2012, **48**, 2891-2893.

110.   M. Jambhrunkar, M. Yu, H. Zhang, P. Abbaraju, A. K. Meka, A. Cavallaro, Y. Lu, N. Mitter and C. Yu, *Nano Research*, 2017, DOI: 10.1007/s12274-017-1640-1.

111.   S. E. Lazic, C. J. Clarke-Williams and M. R. Munafò, *Plos Biol*, 2018, **16**, e2005282.

112.   O. A. Maslova, M. R. Ammar, G. Guimbretière, J. N. Rouzaud and P. Simon, *Physical Review B*, 2012, **86**, 134205.

113. L. G. Cançado, A. Jorio, E. H. M. Ferreira, F. Stavale, C. A. Achete, R. B. Capaz, M. V. O. Moutinho, A. Lombardo, T. S. Kulmala and A. C. Ferrari, *Nano Lett*, 2011, **11**, 3190-3196.

114. A. C. Ferrari and J. Robertson, *Physical Review B*, 2000, **61**, 14095-14107.

115. B. Bayatsarmadi, Y. Zheng, M. Jaroniec and S. Z. Qiao, *Chemistry – An Asian Journal*, 2015, **10**, 1546-1553.

116. B. Smith, K. Wepasnick, K. E. Schrote, H.-H. Cho, W. P. Ball and D. H. Fairbrother, *Langmuir*, 2009, **25**, 9767-9776.

117. B. Smith, K. Wepasnick, K. E. Schrote, A. R. Bertele, W. P. Ball, C. O'Melia and D. H. Fairbrother, *Environ Sci Technol*, 2009, **43**, 819-825.

118. N. B. Saleh, L. D. Pfefferle and M. Elimelech, *Environ Sci Technol*, 2008, **42**, 7963-7969.

119. F. Zhang, Y. Meng, D. Gu, Yan, C. Yu, B. Tu and D. Zhao, *Journal of the American Chemical Society*, 2005, **127**, 13508-13509.

120. W. Shang, J. H. Nuffer, J. S. Dordick and R. W. Siegel, *Nano Lett*, 2007, **7**, 1991-1995.

121. J. Zhang, S. Karmakar, M. H. Yu, N. Mitter, J. Zou and C. Z. Yu, *Small*, 2014, **10**, 5068-5076.

122. Y. Niu, M. Yu, A. Meka, Y. Liu, J. Zhang, Y. Yang and C. Yu, *J Mater Chem B*, 2016, **4**, 212-219.

123. H. Yang and J. Irudayaraj, *J Amer Oil Chem Soc*, 2001, **78**, 889-895.

124. A. C. Lua and T. Yang, *Journal of Colloid and Interface Science*, 2005, **290**, 505-513.

125. Y. Xiao and M. R. Wiesner, *J Hazard Mater*, 2012, **215**, 146-151.

126. M. C. Moran, A. F. Jorge and M. P. Vinardell, *Biomacromolecules*, 2014, **15**, 3953-3964.

127. D. Trachootham, J. Alexandre and P. Huang, *Nat Rev Drug Discov*, 2009, **8**, 579-591.

128. A. A. Alfadda and R. M. Sallam, *Journal of Biomedicine and Biotechnology*, 2012, **2012**, 14.

129. E. Panieri and M. M. Santoro, *Cell Death Dis*, 2016, **7**.

130. T. Shinya, O. Keisei, Y. Junji and H. Hiroshi, *FEBS Letters*, 1995, **358**, 1-3.

131. T. P. Szatrowski and C. F. Nathan, *Cancer Research*, 1991, **51**, 794-798.

132. B. Marengo, M. Nitti, A. L. Furfaro, R. Colla, C. D. Ciucis, U. M. Marinari, M. A. Pronzato, N. Traverso and C. Domenicotti, *Oxidative Medicine and Cellular Longevity*, 2016, **2016**, 6235641.

133. L. He, T. He, S. Farrar, L. Ji, T. Liu and X. Ma, *Cellular Physiology and Biochemistry*, 2017, **44**, 532-553.

134. M. V. Liberti and J. W. Locasale, *Trends in biochemical sciences*, 2016, **41**, 211-218.

135. R. Diaz-Ruiz, M. Rigoulet and A. Devin, *Biochimica et Biophysica Acta (BBA) - Bioenergetics*, 2011, **1807**, 568-576.

136. T. M. Johnson, Z. X. Yu, V. J. Ferrans, R. A. Lowenstein and T. Finkel, *Proceedings of the National Academy of Sciences*, 1996, **93**, 11848-11852.

137. J. M. MatÉs, C. Pérez-Gómez and I. N. De Castro, *Clinical Biochemistry*, 1999, **32**, 595-603.

138. P. A. Riley, *Int J Radiat Biol*, 1994, **65**, 27-33.

139. W. Domej, K. Oettl and W. Renner, *Int J Chronic Obstr*, 2014, **9**, 1207-1224.

140. D. Li, M. B. Müller, S. Gilje, R. B. Kaner and G. G. Wallace, *Nature nanotechnology*, 2008, **3**, 101.

141. X. Huang, B. Sun, D. Su, D. Zhao and G. Wang, *J Mater Chem A*, 2014, **2**, 7973-7979.

142. M. V. Blagosklonny, *Leukemia*, 2002, **16**, 455.

143. D. C. DeZwaan and B. C. Freeman, *Cell Cycle*, 2008, **7**, 1006-1012.

144. P. Csermely, T. Schnaider, C. So"ti, Z. Prohászka and G. Nardai, *Pharmacology & Therapeutics*, 1998, **79**, 129-168.

145. L. Neckers, T. W. Schulte and E. Mimnaugh, *Investigational New Drugs*, 1999, **17**, 361-373.

146. L. Neckers and P. Workman, *Clinical cancer research : an official journal of the American Association for Cancer Research*, 2012, **18**, 64-76.

147. A. N. Tse, D. S. Klimstra, M. Gonen, M. Shah, T. Sheikh, R. Sikorski, R. Carvajal, J. Mui, C. Tipian, E. O'Reilly, K. Chung, R. Maki, R. Lefkowitz, K. Brown, K. Manova-Todorova, N. Wu, M. J. Egorin, D. Kelsen and G. K. Schwartz, *Clinical cancer research : an official journal of the American Association for Cancer Research*, 2008, **14**, 6704-6711.

148. Y. Li, T. Zhang, S. J. Schwartz and D. Sun, *Drug Resistance Updates*, 2009, **12**, 17-27.

149. U. Banerji, A. O'Donnell, M. Scurr, S. Pacey, S. Stapleton, Y. Asad, L. Simmons, A. Maloney, F. Raynaud, M. Campbell, M. Walton, S. Lakhani, S. Kaye, P. Workman and I. Judson, *Journal of Clinical Oncology*, 2005, **23**, 4152-4161.

150. E. I. Heath, D. W. Hillman, U. Vaishampayan, S. Sheng, F. Sarkar, F. Harper, M. Gaskins, H. C. Pitot, W. Tan, S. P. Ivy, R. Pili, M. A. Carducci, C. Erlichman and G. Liu, *Clin Cancer Res*, 2008, **14**, 7940-7946.

151. E. A. Ronnen, G. V. Kondagunta, N. Ishill, S. M. Sweeney, J. K. DeLuca, L. Schwartz, J. Bacik and R. J. Motzer, *Investigational New Drugs*, 2006, **24**, 543-546.

152. M. Edward, J. Keith, A. B. Paul, J. D. Martin and W. Paul, *Curr Top Med Chem*, 2006, **6**, 1193-1203.

153. F. Fay, C. J. Scott and P. A. McCarron, *Curr Nanosci*, 2010, **6**, 560-570.

154. Y. Fang, Y. Lv, F. Gong, Z. Wu, X. Li, H. Zhu, L. Zhou, C. Yao, F. Zhang, G. Zheng and D. Zhao, *J Am Chem Soc*, 2015, **137**, 2808-2811.

155. G. Xu, S. Liu, H. Niu, W. Lv and R. a. Wu, *Rsc Adv*, 2014, **4**, 33986-33997.

156. Q. Kong, L. Zhang, J. Liu, M. Wu, Y. Chen, J. Feng and J. Shi, *Chem. Commun.*, 2014, **50**, 15772-15775.

157. D. Jaque, L. Martinez Maestro, B. del Rosal, P. Haro-Gonzalez, A. Benayas, J. L. Plaza, E. Martin Rodriguez and J. Garcia Sole, *Nanoscale*, 2014, **6**, 9494-9530.

158. A. A. Balandin, *Nature Materials*, 2011, **10**, 569.

Chapter 7

Conclusion and Outlook

The research that I have accomplished during my PhD is presented in this dissertation provides a guide to optimise multi-functional mesoporous carbon nanocarriers by controlling the carbonisation temperature during the fabrication process using a hard templating method. This dissertation discussed in details how the carbonisation temperature would influence the behaviour and characteristics of the nanocarriers to display its highest biomedical performance. Currently, mesoporous carbon nanocarriers are being extensively investigated for bio applications especially in cancer therapeutics as it possesses several advantageous qualities than other carbon-based nanocarrier systems such as the open porous framework for higher drug/biomolecule loading, sustained release pattern, high biocompatibility, high cellular uptake, faster endosomal escape. Carbonisation temperature plays a key role in the development of the advantageous features of mesoporous carbon nanocarriers. Setting up the carbonisation temperature is crucial during the fabrication process as it determines the morphology, carbon content, crystallinity, carbon-carbon bonding, hydrophobicity etc., as the 3D carbon framework is being formed in a controlled environment. These physicochemical properties determine its multifunctional ability such as therapeutic drug delivery efficiency, free radical scavenging property or photothermal conversion efficiency.

7.1. Conclusions:

7.1.1. In the first project, Chapter 4, we dived into the first functionality of the nanocarrier system, i.e. therapeutic drug delivery. For this project, mesoporous carbon nanocarriers MCHS-*T* were fabricated using silica hard templating method, where the

resorcinol-formaldehyde polymer was used as a carbon precursor source. The polymer-silica matrix were carbonised at various temperatures from 500°C (MCHS-500), 700°C (MCHS-700), 900°C (MCHS-900) and 1100°C (MCHS-1100) to investigate the physicochemical changes in the nanocarriers synthesized followed by the evaluation of its therapeutic delivery of therapeutic protein performance in cancer cells. MCHS-500 showed an aggregated, non-uniform and partially concaved spherical morphology. Other nanocarriers showed spherical morphologies with uniform particle sizes of $\sim$ 170 nm in diameter. Out of all the nanocarrier systems, MCHS-900 emerged as the nanocarrier with the with high aqueous distribution with 0.1 PDI, high carbon content (84.2 %), high surface area, high loading capacity of RNase A protein, better hydrophobicity and sustained release of the protein. Moreover, the nanocarriers displayed efficient cellular activity such as uptake and quicker endosomal escape to carry and release the protein intracellularly the most efficient way possible compared to other nanocarrier systems. This resulted $\sim$74.4% of cell inhibited by MCHS-900@RNase A at the dosage of 50 µg mL^{-1} in first 24-hour incubation while after 48-hour incubation, 93.9% of the cells died indicating potent anticancer activity. It was concluded that temperature lower than 900°C carbonisation temperature suffers from poor physicochemical properties that hinder its biological effectiveness. While carbonisation temperature higher than 900 °C suffers from lower colloidal stability and poor cellular uptake that impedes their full potential as a nanocarrier.

7.1.2. The major contribution of this work is the discovery of the antioxidant properties of this nanocarrier system which is the second functionality of MCHS dictated by the carbonisation temperature. In this project, we found that MCHS-900 has high free radical scavenging activity with an efficiency of 74 % reduction in OH$^{\bullet}$ in the aqueous environment, higher than any other MCHS-T. When compared with other popular nanocarrier systems such as CNT and RGO, it showed 3.2 and 2.7 times higher antioxidant activity respectively. Moreover, MCHS-900 can reduce the intracellular ROS levels by 93.7 % of the oxidatively stressed cells. Utilising MCHS-900 might be an effective way to reduce the cellular oxidative stress in cells that can create and propagate cancer or tumour formation (details can be referred to in Chapter 5).

7.1.3. Utilizing the knowledge gathered in the previous project on the physicochemical changes brought about by the carbonisation temperature, we proceeded to test the photoconversion ability of MCHS-T for its application in combination cancer therapy. MCHS-900 showed high photoconversion ability by reaching 43°C (clinical threshold

>40°C) after UV irradiation. 17 AAG, a heat shock chaperone protein inhibitor, was loaded in MCHS-900 which suffers from low bioavailability on its own. We then applied a combination of 17AAG@MCHS-900 incubated with MCF-7 breast cancer cells and irradiated with UV light showed ~86% reduction in cells detected by MTT assay. MCHS carbonised at lower temperature didn't have much photoconversion efficiency while MCHS carbonised at higher temperature although showed good photoconversion efficiency, had lower cytotoxicity owing to lower cellular interaction.We concluded that carbonisation temperature also influences the photothermal capabilities of nanocarriers of converting light into heat that might be a useful tool when applied in photothermal or combination therapy

 Thus,   this PhD dissertation concludes that 900°C is the optimised temperature at which the mesoporous carbon nanocarriers should be carbonised during the fabrication process to achieve the best biomedical functionality.

7.2. Recommendations for future work

This work introduced the dynamics that come into play when it comes to the influence of carbonisation temperature during fabrication of mesoporous carbon nanocarriers and the changes it brings in its multifunctional bioapplications. However, there is still room to do a more elaborate investigation of ways to improve the efficiency of mesoporous carbon nanocarriers. The versatility of MCHS allows them to be applied in different ways such as drug delivery systems, ROS scavengers and photothermal agents which may help combat cancer /tumour growth, propagation and malignancies.

 In chapter 4, we focussed our attention on the delivery performance of the mesoporous carbon nanocarriers. Carbonising MCHS at the optimised temperature helped us deliver fragile therapeutic protein in large amounts intracellularly to achieve cancer cell inhibition. As a result, we achieved high anti-cancer effect from more safer and potent therapeutic protein than conventional chemotherapy that results in numerous side effects.

 In chapter 5, we have shown the outstanding ability of MCHS-900 to scavenge free radicals that are highly detrimental and can cause major illnesses. High levels of intracellular ROS are the primary reason for many grave illnesses including cancer. Overextended exposure of ROS has shown to create new cancer cells and help in its growth. Using potent antioxidant agents such as MCHS might be a solution to this challenge as it effectively scavenges intracellular free radicals more effectively than any other carbon nanocarrier agent or conventional antioxidants. More investigation

might lead to more breakthroughs related to the possibilities of utilising its antioxidant properties to only cancer but also other grave illnesses.

In the final project, chapter 6, we were able to use MCHS as a photothermal agent as well as a chemotherapy nanocarrier. The versatility of the nanocarrier allowed us to successfully use it as a combination therapy in breast cancer cells. MCHS-900 showed useful photothermal of irradiated light into heat which reached to clinal significance while delivering low bioavailable and sensitive 17 AAG HSP90 inhibitor causing significant cellular inhibition. Unfortunately, due to time constraints, we couldn't investigate the project further. There is still room for more investigation such as in- vivo studies that can show the nanocarrier systems inhibit the growth or shrink the localised tumour with this combination therapy and mark the effectiveness of this therapy.

Through this PhD dissertation, I hope we were able to shed some light into the optimisation process of mesoporous carbon nanocarrier systems and its multifunctionality aspect and wish to see it transition from a proof of concept to clinical relevance and practice.